


March 2016

## Model Systems for Characterizing the Intrinsic Properties of Polymer Semiconductors: Oligomers and Single Crystals

Nicholas S. Colella  
*University of Massachusetts Amherst*

Follow this and additional works at: [https://scholarworks.umass.edu/dissertations\\_2](https://scholarworks.umass.edu/dissertations_2)

 Part of the [Polymer and Organic Materials Commons](#), [Polymer Science Commons](#), and the [Semiconductor and Optical Materials Commons](#)

---

### Recommended Citation

Colella, Nicholas S., "Model Systems for Characterizing the Intrinsic Properties of Polymer Semiconductors: Oligomers and Single Crystals" (2016). *Doctoral Dissertations*. 558.  
[https://scholarworks.umass.edu/dissertations\\_2/558](https://scholarworks.umass.edu/dissertations_2/558)

This Open Access Dissertation is brought to you for free and open access by the Dissertations and Theses at ScholarWorks@UMass Amherst. It has been accepted for inclusion in Doctoral Dissertations by an authorized administrator of ScholarWorks@UMass Amherst. For more information, please contact [scholarworks@library.umass.edu](mailto:scholarworks@library.umass.edu).

**MODEL SYSTEMS FOR CHARACTERIZING THE INTRINSIC PROPERTIES  
OF POLYMER SEMICONDUCTORS: OLIGOMERS AND SINGLE CRYSTALS**

A Dissertation Presented

by

NICHOLAS S. COLELLA

Submitted to the Graduate School of the  
University of Massachusetts Amherst in partial fulfillment  
of the requirements for the degree of

DOCTOR OF PHILOSOPHY

February 2016

Polymer Science and Engineering

© Copyright by Nicholas S. Colella 2016

All Rights Reserved

**MODEL SYSTEMS FOR CHARACTERIZING THE INTRINSIC PROPERTIES  
OF POLYMER SEMICONDUCTORS: OLIGOMERS AND SINGLE CRYSTALS**

A Dissertation Presented

by

NICHOLAS S. COLELLA

Approved as to style and content by:

---

Alejandro L. Briseno, Co-Chair

---

James J. Watkins, Co-Chair

---

Sankaran Thayumanavan, Member

---

David A. Hoagland, Department Head

Polymer Science and Engineering

## **DEDICATION**

*To my friends and family, without whom none of this would have been possible.*

*Mom, Dad, Chris, Grammy & Papa, Nonna, Gus,  
Thao, Jon, Dan, Marcos, Itza, Brittany, Joelle, Sami, Kyle, Emma, Aria,  
Zach, John, Hallie, Alex, Eric, Drew, Drew, Christian, and Jeremy – thank you.*

## ACKNOWLEDGMENTS

I would first like to thank my advisors, Professor Alex Briseno and Professor Jim Watkins. Their guidance and support throughout my graduate studies has been phenomenal. Alex has been a treasure trove of information with his encyclopedic knowledge of the literature. Moreover, his creativity in the lab and passion for research have driven me to achieve my goals during my time in PSE. Jim's focus and directed advice were essential for the completion of my research. Seldom have I met such an insightful scientist who has such a great understanding of both the broad goals of the field as well as the experimental details necessary for impactful research in the lab.

I would also like to thank my thesis committee member, Professor Thayumanavan. His support, friendly demeanor, and constructive critique of the research presented here helped greatly in making this work complete and thorough.

I must thank the CHM for the support they have given me, both intellectually and financially, during my time at PSE.

My fellow group members from both the Briseno and Watkins group were instrumental in keeping me both happy and productive during my time in graduate school. In particular, Lei Zhang was an amazing mentor as well as friend, and I am a better scientist and person having known him. Marcos Reyes was a fellow scientist I could always depend on, whether I needed advice on an experiment or just a laugh and camaraderie. Dongpo Song is one of the most thoughtful scientists that I have had the pleasure of working with and our collaborations were both numerous and impactful. Joelle Labastide helped me keep my sanity during tough times and I will be forever grateful for her support and knowledge. Professor Henning Winter is an amazing

scientist with a wonderful sense of humor – every conversation that I had with him was truly a pleasure.

Jayanta, Qingshuo, Cheng, Ying, Irene, Ben, and Feng were amazing collaborators; I am both proud and honored to have worked with them. All of the other members of the Briseno and Watkins groups, too numerous to list here, were brilliant colleagues and I am elated to be a part of such a talented group of phenomenal people.

I want to thank the PSE Class of 2010 for being so remarkable. They have made the past 5 years enjoyable and I certainly would not have been able to make it through without them.

Finally, I would like to thank my family. Their unending support throughout my graduate studies has given me strength that I cannot even begin to describe.

## **ABSTRACT**

### **MODEL SYSTEMS FOR CHARACTERIZING THE INTRINSIC PROPERTIES OF POLYMER SEMICONDUCTORS: OLIGOMERS AND SINGLE CRYSTALS**

**FEBRUARY 2016**

**NICHOLAS S. COLELLA, B.A., WILLIAMS COLLEGE**

**M.S., UNIVERSITY OF MASSACHUSETTS AMHERST**

**PH.D., UNIVERSITY OF MASSACHUSETTS AMHERST**

**Directed by: Professor Alejandro L. Briseno and Professor James J. Watkins**

Polymer semiconductors hold great promise for the realization of inexpensive, flexible electronic devices. One of the greatest strengths of these materials, their low-cost processability from solution, results in a wide range of solid-state structures. The crystallinity and morphology of these materials strongly impacts their performance as charge carriers. Furthermore, the nature of polymerization inherently leads to the production of materials which are disperse in their molecular character, with regard to both coupling and molecular weight. Thus, it is difficult to deconvolute the intrinsic properties of polymer semiconductors from their synthetic and processing conditions.

Polythiophenes are particularly susceptible to performance variations due to their dependence on crystallinity for effective charge transport. Moreover, it is difficult to characterize charge transport within their crystallites, which are often tens of nanometers in size. The approaches reported here are intended to provide well-defined model systems, oligomers and single crystals, for characterizing the crystallization and semiconductor physics of conjugated polymers.



In Chapter 2, the characterization of monodisperse oligothiophenes is reported. In evaluating the evolution of crystalline, morphological, and optoelectronic properties with increasing chain length, the transition from monomer to polymer is described. The pentamer of poly[bis(3-dodecyl-2-thienyl)-2,2'-dithiophene -5,5'-diyl] (PQT-12) is identified as a potential model system for probing the intrinsic properties of the polymer.

In Chapter 3, the interactions between a model oligomer, the trimer of poly[2,5-bis(3-dodecylthiophen-2-yl)thieno[3,2-*b*]thiophene] (PBTTT), and high molecular weight polymer are characterized. The effects of enhanced crystallinity and connectivity, from the oligomer and polymer, respectively, are reported. In particular, the morphology, crystallinity, and charge transport properties of films of blended oligomer-polymer systems were studied. Although oligomers are often considered impurities in the synthesis of semiconducting polymers for device applications, it was demonstrated that films consisting of up to 83% oligomer exhibited high charge transport mobilities equal to that of pure high molecular weight polymer.

In Chapter 4, a novel technique for the fractionation and recrystallization of oligothiophenes in supercritical fluid is reported. Furthermore, the crystal habit, structure, and molecular coupling of the resulting crystals are described. This crystallization method leverages the solubilizing and transport properties of supercritical fluids to create a system that combines the advantages of crystallizations from vapor and solution and could be broadly applied to the crystallization of other polymeric systems.

## TABLE OF CONTENTS

	Page
ACKNOWLEDGMENTS .....	v
ABSTRACT .....	vii
LIST OF TABLES .....	xiii
LIST OF FIGURES .....	xiv
CHAPTER	
1. INTRODUCTION .....	1
1.1 Organic Semiconductor Overview .....	1
1.1.1 Traditional Semiconductors .....	1
1.1.2 $\pi$ -Conjugated Systems .....	1
1.1.3 Charge Transport in Crystalline Materials .....	2
1.1.4 Motivation .....	6
1.2 Structure-Property Relationships .....	7
1.2.1 Overview .....	7
1.2.2 Molecular Structure .....	7
1.2.3 Morphology .....	8
1.2.4 Single Crystal Measurements .....	9
1.2.5 The Role of Oligomers .....	10
1.4 Dissertation Overview .....	11
2. CHARACTERIZING THE TRANSITION FROM MONOMER TO POLYMER .....	12
2.1 Introduction .....	12
2.2 Experimental .....	19

2.2.1 Materials .....	19
2.2.2 Methods.....	20
2.3 Results and Discussion .....	22
2.3.1 Evaluating oligomer molecular weight and purity.....	22
2.3.2 Characterization of crystallinity and thermal properties.....	23
2.3.3 The evolution in crystal structure for short oligothiophenes .....	26
2.3.4 Characterization of DDQT-3 single crystal by transmission electron microscopy .....	28
2.3.5 Characterization of DDQT oligomer packing in thin films .....	29
2.3.6 Characterization of morphology by atomic force microscopy .....	32
2.3.7 Determination of ionization potentials of DDQT thin films.....	35
2.3.8 Evolution of optoelectronic properties and determination of effective conjugation length.....	36
2.3.9 Summary .....	43
 3. DETERMINING THE SOLID-STATE INTERACTIONS BETWEEN OLIGOMER AND POLYMER.....	 44
3.1 Introduction.....	44
3.2 Experimental .....	46
3.2.1 Materials .....	46
3.2.2 Methods.....	47
3.3 Results and Discussion .....	48
3.3.1 Characterization of oligomer and polymer purity and molecular weight.....	48
3.3.2 Characterization of the surface morphology of blended films.....	49
3.3.3 Analysis of molecular packing in blended films.....	51
3.3.4 Characterization of crystallinity and thermal properties.....	55

3.3.5 Charge transport properties of blended films.....	57
3.3.6 Summary .....	60
4. FRACTIONATION AND CRYSTALLIZATION OF OLIGOMERS IN SUPERCRITICAL FLUID.....	62
4.1 Introduction.....	62
4.1.1 Processing and Crystallization Techniques .....	62
4.1.2 Crystallization from solution .....	62
4.1.3 Crystallization from vapor .....	64
4.1.4 Properties of supercritical fluids .....	66
4.2 Experimental.....	67
4.2.1 Materials .....	67
4.2.2 Methods.....	68
4.3 Results and Discussion .....	69
4.3.1 Crystallization of small molecules in supercritical carbon dioxide.....	69
4.3.2 Crystallization of rubrene in supercritical hexane .....	76
4.3.3 Fractionation and crystallization of oligothiophenes in supercritical hexane .....	80
4.3.4 Characterization of PBTTT crystal species molecular weight .....	83
4.3.5 Infrared spectroscopy of BTTT1.5 Crystals .....	86
4.3.6 Characterization of BTTT1.5 crystal habit .....	87
4.3.7 Characterization of BTTT1.5 unit cell parameters and molecular packing relative to the crystal axis.....	90
4.3.8 Characterization of BTTT1.5 molecular coupling in crystals .....	93
4.3.9 Comparison of BTTT1.5 crystals generated in supercritical hexane with BTTT1.5 crystals generated <i>via</i> traditional solution recrystallization.....	95

4.3.10 Summary .....	97
5. FINAL COMMENTS AND OUTLOOK .....	99
5.1 Conclusions .....	99
BIBLIOGRAPHY .....	101

## LIST OF TABLES

Table	Page
<b>Table 2.1</b> MALDI-ToF expected molecular weights, observed molecular weights, and molecular weights and polydispersity index (PDI) determined by gel permeation chromatography (GPC). .....	23
<b>Table 2.2</b> Melting and crystallization temperatures as well as the enthalpy of melting for DDQT-1 through DDQT-6. ....	25
<b>Table 2.3</b> Ionization potentials of DDQT oligomers as determined by UPS. ....	36
<b>Table 2.4</b> Wavelengths of maximum absorbance and the optical band gaps for solutions and thin films of DDQT oligomers. ....	37
<b>Table 2.5</b> Effective conjugation lengths and wavelength of maximum absorbance for an infinite polymer for selected systems. ....	41
<b>Table 3.1</b> Surface roughness of films with various oligomer/polymer compositions. ....	51
<b>Table 3.2.</b> Mobilities, threshold voltages, and on/off current ratios for transistors fabricated from films with various oligomer/polymer compositions. ....	59
<b>Table 4.1</b> Molecular weight of potential structures for PBTTT degradation. ....	85
<b>Table 4.2</b> Wavenumbers of aromatic and aliphatic (alkyl) C-H stretching modes as observed by FTIR spectroscopy. ....	87

## LIST OF FIGURES

Figure	Page
<b>Figure 1.1</b> Schematics of an organic photovoltaic (left) and field-effect transistor (right) devices. ....	4
<b>Figure 1.2</b> Cartoons depicting charge transport in single crystal, semicrystalline, and primarily amorphous films of organic semiconductors. ....	9
<b>Figure 1.3</b> The free energy landscape (a), relation between crystal area, energy, and length (b), and cartoon depicting P3HT chain packing within a crystal (c). ....	10
<b>Figure 2.1</b> Plot of P3HT mobility as a function of regioregularity (a), out-of-plane (b) and in-plane (c) diffraction of P3HT films with various regioregularities. ....	14
<b>Figure 2.2</b> Plot depicting the mobility of P3HT as a function of molecular weight and spin-coating solvent. ....	15
<b>Figure 2.3</b> Atomic force micrographs of various morphologies obtained from different molecular weights and coating methods for P3HT. ....	16
<b>Figure 2.4</b> Model illustrating the factors which limit conjugation in conjugated polymers. ....	18
<b>Figure 2.5</b> DDQT repeat unit of PQT-12. ....	19
<b>Figure 2.6</b> Scheme for the synthesis of DDQT oligomers. ....	20
<b>Figure 2.7</b> Gel permeation chromatography traces (A) and MALDI-ToF spectra for DDQT oligomers. ....	23
<b>Figure 2.8</b> Differential scanning calorimetry traces (second heating cycle) for DDQT-1 through DDQT-6 (endo down) (a) and a plot of melting point and enthalpy of melting as a function of oligomer length (b). ....	25
<b>Figure 2.9</b> DDQT-2 (top) and DDQT-3 (bottom) crystal structures, as viewed down the <i>c</i> axis, demonstrating the change in packing motif from “lamellar herringbone” to a lamellar structure. ....	27

<b>Figure 2.10</b> DDQT-2 (left) and DDQT-3 (right) molecules within their respective crystal structures. ....	28
<b>Figure 2.11</b> Transmission electron micrograph of a DDQT-3 crystal belt with an overlay of the molecular packing (alkyl side chains removed for clarity) (A), selected area electron diffraction from the crystal (B), and SAED pattern calculated from the bulk crystal structure (C). ....	29
<b>Figure 2.12</b> Grazing incidence X-ray scattering of DDQT 1 to DDQT-6 films (a-f), respectively.....	31
<b>Figure 2.13</b> Height (a-f) and phase (g-l) atomic force micrographs (10 $\mu\text{m}$ x 10 $\mu\text{m}$ ) of DDQT-1 through DDQT-6 films, respectively.....	34
<b>Figure 2.14</b> Atomic force micrographs of DDQT-5 films, 1 $\mu\text{m}$ x 1 $\mu\text{m}$ , height (left) and phase (right).. ....	35
<b>Figure 2.15</b> Ultraviolet photoelectron spectra (left) and a plot of ionization potential as a function of DDQT oligomer length. ....	36
<b>Figure 2.16</b> Normalize UV-vis spectra for solutions and thin films of DDQT oligomers.....	37
<b>Figure 2.17</b> Wavelength of maximum absorbance as a function of the number of thiophene repeat units for selected systems. ....	40
<b>Figure 2.18</b> Results from the quantum mechanical geometric optimization of alkylthiophene-thienothiophene dimer. ....	41
<b>Figure 3.1</b> Molecular structures of BTTT-3 and PBTTT (left), and gel permeation chromatography traces for BTTT-3 and PBTTT (right).....	49
<b>Figure 3.2</b> Atomic force micrographs of films with various oligomer/polymer compositions.. ....	50
<b>Figure 3.3</b> Atomic force micrographs of a 1:5 (polymer:oligomer) film demonstrating terraced morphology (a), and the terraced morphology (b) and a schematic (c) for highly crystalline, annealed, high molecular weight film of PBTTT. ....	51
<b>Figure 3.4</b> Grazing incidence wide angle X-ray scattering diffractograms of films with various oligomer/polymer compositions. ....	53



<b>Figure 3.5</b> Cartoon of pure BTTT-3 crystallites and crystallites which have incorporated PBTTT into their structure.....	55
<b>Figure 3.6</b> Differential scanning calorimetry traces for the side chain and backbone melting regions of BTTT-3 (a) and PBTTT (b) (endo down). .....	56
<b>Figure 3.7</b> Transfer curves ( $V_{DS} = -60$ V) (a) and a characteristic output curve (5:1 blend) (b) for transistors fabricated from films with various oligomer/polymer compositions, as well as a plot of hole mobility as a function of film composition.....	58
<b>Figure 3.8</b> Plot of the surface roughness and mobility values for films with various oligomer/polymer compositions.....	59
<b>Figure 3.9</b> Cartoon of the morphology of a pure BTTT-3 film (left), and a majority BTTT-3 film in which polymer has been incorporated, connecting the crystallites (right).....	60
<b>Figure 4.1</b> Cartoon of crystallization using the physical vapor transport recrystallization method.....	65
<b>Figure 4.2.</b> Phase diagram for carbon dioxide, illustrating the conditions for the supercritical phase. ....	67
<b>Figure 4.3</b> Image of the 110 mL pressure reactor in the reflux geometry. ....	70
<b>Figure 4.4</b> Schematic of solvent flow inside the reactor in the reflux geometry. ....	71
<b>Figure 4.5</b> Schematic of the reactor used by Laudise, <i>et al.</i> , for the crystallization of quartz in supercritical (hydrothermal) water. ....	71
<b>Figure 4.6</b> Solubility data for caffeine in carbon dioxide .....	73
<b>Figure 4.7</b> Images of caffeine crystals grown on the polyimide-lined walls of the reactor (A), on the polyimide film removed from the reactor (B), and optical micrographs of the crystals demonstrating their size and purity (C, D). ....	74
<b>Figure 4.8</b> Images of the polycrystalline source naphthalene and the material recrystallized in supercritical CO <sub>2</sub> . ....	75
<b>Figure 4.9</b> X-ray diffraction data for naphthalene crystals (left) and images of the crystals and inset of BFDH crystal habit (right). ....	76

<b>Figure 4.10</b> Image of the 110 mL reactor in the diffusive geometry (left) and temperature profile for the reactor during operation (right). .....	78
<b>Figure 4.11</b> Density and viscosity of hexane at 900 PSI as a function of temperature. Data from NIST Chemistry Webbook. <sup>105</sup> .....	79
<b>Figure 4.12</b> Schematic illustrating the recrystallization of rubrene by diffusion through supercritical hexane. ....	80
<b>Figure 4.13</b> Image of the small pressure reactor in the diffusive geometry.....	81
<b>Figure 4.14</b> Temperature profile for the small pressure reactor. ....	82
<b>Figure 4.15</b> Schematic of the steel pressure reactor (A), molecular structure of PBTTT (B), and optical micrograph of the as-grown crystals (C). ....	83
<b>Figure 4.16.</b> MALD-ToF data for the crystals and source polymer. ....	84
<b>Figure 4.17</b> Fourier transform infrared spectra of the BTTT1.5 crystals, PBTTT material recovered from the residual hexane solution after recrystallization, and unpurified source material. ....	87
<b>Figure 4.18</b> Atomic force phase (A) and height (B) micrographs of a BTTT1.5 crystal. Profile of the crystal, demonstrating the sharp facets of the crystals, with 120° angles between faces. ....	88
<b>Figure 4.19</b> Scanning electron micrograph of a tilted BTTT1.5 crystal which has been bisected. ....	89
<b>Figure 4.20</b> A series of scanning electron micrographs “stitched” together.....	89
<b>Figure 4.21</b> Optical micrograph of BTTT1.5 crystals. ....	90
<b>Figure 4.22</b> Transmission electron micrograph and selected area electron diffraction of a single BTTT1.5 crystal. ....	91
<b>Figure 4.23</b> Polarization-resolved photoluminescence data (A) and a photoluminescence image of a PBTTT1.5 crystal and schematic of the crystal, with labeled axes (B).....	92
<b>Figure 4.24</b> Schematic of a potential unit cell. ....	93
<b>Figure 4.25</b> Time and polarization resolved photoluminescent responses (B-E)of a single BTTT1.5 crystal (A). ....	95

**Figure 4.26** Synthetic scheme of BTTT1.5 and the photoluminescent spectra of the solution (blue), polycrystalline film (grey), crystal grown in supercritical hexane (green), and crystal grown in hexane at ambient conditions (red). .....97

# CHAPTER 1

## INTRODUCTION

### 1.1 Organic Semiconductor Overview

#### 1.1.1 Traditional Semiconductors

Inorganic semiconductors such as silicon have been instrumental to the development of modern electronics due to their ability to transport charge carriers (electrons and/or holes) through their crystal lattice. Generally, dopants, *i.e.* atoms which have energy levels close to the conduction or valence band edges, are used to produce mobile charges at room temperature. Charge transport occurs through the molecular orbitals (bands) which are delocalized throughout the covalently bonded crystal.

#### 1.1.2 $\pi$ -Conjugated Systems

In order for electrons or holes to move throughout a molecule, the wave function must be distributed across multiple atoms. This phenomenon is well described by molecular orbital theory, which explains how both sigma and pi bonds are formed by overlapping atomic orbitals of neighboring atoms.  $Sp^2$  hybridized carbon is the foundation of organic semiconductors, as the  $p_z$  orbitals located orthogonal to the sigma bonds may form pi bonds through which charges may flow. In comparison with sigma bonds, which are localized between atoms, electrons in the pi bonds are delocalized and are thus much more polarizable which helps to further stabilize charge carriers on surrounding atoms and molecules.

Unlike inorganic semiconductors, where all atoms in the crystal lattice are covalently bound, organic semiconductors assemble through intermolecular forces, such as  $\pi$ - $\pi$  stacking and van der Waals' interactions. As a result, charge transport occurs

largely through tunneling or “hopping” between molecular orbitals, particularly the ground-state highest occupied molecular orbitals (HOMO) and lowest unoccupied molecular orbitals (LUMO) for holes and electrons, respectively, of neighboring molecules. This hopping between localized states, as opposed to band transport, is due to the polaronic nature of charge carriers in organic crystallites; the phonons present in the lattice structures have sufficient energy at room temperature to disrupt spatial coherence, and this effect is magnified by the presence of defects in the structure.<sup>1</sup> While this arrangement limits the speed at which charges can move through organic systems, the non-covalent nature of assembly allows the materials to be solution-processed, forming flexible, lightweight semiconducting solids.<sup>2-4</sup> Additionally, if registration of molecular orbitals between neighboring molecules is sufficient, the wave function may be distributed across an entire crystal, resulting in band transport if not disrupted by molecular vibrations (typically at low temperatures). This effect has been observed in single crystals of rubrene, a benchmark small molecule organic semiconductor.

Organic semiconductors are particularly appealing because their processability offers the opportunity for low-cost, flexible electronics which can be fabricated without the stringent and intense environments that inorganic semiconductors require. Additionally, the tailorability of molecular semiconductors allows for a nearly infinite variety conjugated materials; virtually all of the electronic and physical properties of organic semiconductors can be tuned for specific applications.

### **1.1.3 Charge Transport in Crystalline Materials**

Charge transport is readily measured and characterized in organic field-effect transistors (OFETs). Charge carriers, i.e. electrons and/or holes, migrate from source to

drain electrodes under an electric field which is produced by a gate electrode separated from the active layer by a dielectric.<sup>5</sup> The region of the organic semiconductor in contact with the dielectric is affected by the induced field; only the material within a few nanometers of the interface makes up the conducting channel. At their most basic, organic photovoltaics (OPVs) consist of two electrodes, an anode and a cathode, separated by (typically intermixed phase of) a p-type (hole-transporting) and an n-type (electron-transporting) semiconductor (Figure 1.1).<sup>6</sup> In OPVs, electrons are excited across the band gap of a p-type organic semiconductor by incident light to form an electron-hole pair, known as an exciton. This exciton then diffuses to an interface between the p-type and n-type semiconductor, typically a fullerene, by the built-in potential between the electrodes. Once the exciton reaches the interface, it is separated into an electron and hole due to the lower LUMO energy of the n-type material, and the charges are transported to their respective electrodes. The efficiency by which this process takes place is reflected in the short circuit current,  $J_{sc}$ , of the device, and thus must be optimized to produce efficient OPVs. In both OFETs and OPVs, the mobility of the charge carriers is paramount.<sup>7</sup>

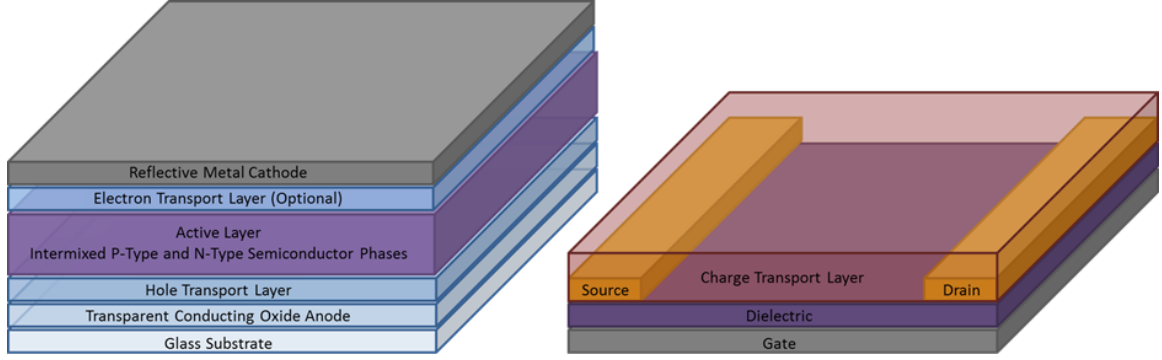


**Figure 1.1** Schematics of an organic photovoltaic (left) and field-effect transistor (right) devices.

In the absence of external fields (e.g. applied voltages in OFETs and built-in potential in OPVs), charge drift in organic semiconductors is diffusive in nature and can be represented as

$$\langle x^2 \rangle = nDt \quad \text{Eq. 1}$$

The mean-square displacement of charges is equal to the product of the diffusion constant,  $D$ , the time,  $t$ , and a scalar which represents the dimensionality of the system ( $n = 2, 4$ , or  $6$  for 1-D, 2-D, and 3-D systems, respectively). Charge mobility,  $\mu$ , is related to the diffusion coefficient according to the Einstein-Smoluchowski equation:

$$\mu = \frac{eD}{k_B T} \quad \text{Eq. 2}$$

where  $e$  is the charge of an electron and  $k_B$  is the Boltzmann constant. The mobility can also be defined as the dependence of charge velocity,  $v$ , on the electric field,  $F$ .

$$\mu = \frac{v}{F} \quad \text{Eq. 3}$$

Therefore, the units of mobility are commonly

$$\frac{1}{s} \times \frac{1}{V/cm^2} = cm^2 V^{-1} s^{-1} \quad \text{Eq. 4}$$

Charge transport in high-mobility crystalline regions is distinct from low-mobility amorphous regions, thus, for a semicrystalline system, the effective mobility can be approximated according to

$$\frac{1}{\mu_{eff.}} = \frac{1}{\mu_{Cryst.}} + \frac{1}{\mu_{Amor.}} \quad \text{Eq. 5}$$

This relation shows that the amorphous regions dominate the effective mobility, significantly limiting the observed charge transport.<sup>2,8</sup> Electronically, amorphous regions and defects in the crystal structure result in carrier traps that are energetically between the highest occupied molecular orbital (HOMO) and lowest unoccupied molecular orbital (LUMO) bands. At room temperature, thermal energy,  $kT$ , where  $k$  is the Boltzmann constant and  $T$  is temperature, is sufficient to excite electrons out of the trap states. This is formalized in the multiple trap-and-release model.<sup>9</sup> Using this depiction, the relationship between the observed mobility,  $\mu$ , and intrinsic mobility,  $\mu_0$ , can be described by

$$\mu = \mu_0 \frac{\tau_{diff}}{\tau_{diff} + \tau_{tr}} \quad \text{Eq. 6}$$

where  $\tau_{diff}$  is the average time of charge diffusion between traps and  $\tau_{tr}$  is the average time of carrier retention in a shallow (i.e. within a few  $kT$  of the band edge) trap. Thus, for virtually defect-free crystals where  $\tau_{diff} \gg \tau_{tr}$ , mobility is maximized and  $\mu \approx \mu_0$ .

Mobility is most commonly measured in a field-effect transistor configuration. In this geometry, an insulating dielectric separates the conducting channel from the gate which modulates current flow. When a sufficient voltage is applied between the source and gate electrodes ( $V_G$ ), charge carriers accumulate at the interface of the organic semiconductor and the dielectric. These charges are then transported along this interface,



up to a few nanometers in height, from the source to drain electrodes due to the voltage applied between those electrodes ( $V_{SD}$ ). In the linear regime, the current increases with  $V_{SD}$ , and the relationship between current ( $I_{SD}$ ) and voltage can be expressed as

$$I_{SD} = \frac{W}{L} \mu C (V_G - V_T) V_{SD} \quad \text{Eq. 7}$$

where  $W$  and  $L$  are the channel width and length, respectively,  $C$  is the capacitance of the gate dielectric, and  $V_T$  is the threshold voltage at which current begins to increase. This behavior is observed when  $V_{SD}$  is considerably lower than  $V_G$ . When  $V_{SD}$  is comparable to or larger than  $V_G$ , the conducting channel near the drain is “pinched-off,” resulting in the saturation regime. Here, the relationship between  $I_{SD}$  and  $V_{SD}$  is

$$I_{SD} = \frac{W}{2L} \mu C (V_G - V_T)^2 \quad \text{Eq. 8}$$

#### 1.1.4 Motivation

Because of their solution-processable nature, organic semiconductors have been the subject of intense research for applications in OPVs and OFETs for radio frequency identification (RFID) tags.<sup>5,10-16</sup> The two main classes of organic semiconductors are small molecules, typically acenes and other polycyclic aromatic hydrocarbons, and polymers, such as polythiophenes. It has been difficult to characterize the intrinsic optoelectronic properties of polymer semiconductors in the solid state because their properties are heavily dependent on their processing and resulting morphology. Additionally, the nature of polymerization produces an inherently disperse material; a range of molecular weights is produced for any given synthesis and the product may contain defects in the coupling of monomeric units.

Thus, the study of the physics of charge transport in organic materials has largely been focused around small molecules. In particular, rubrene has been used as a

benchmark research material because large crystals can be routinely fabricated using the physical vapor transport (PVT) deposition method.<sup>17</sup>

## **1.2 Structure-Property Relationships**

### **1.2.1 Overview**

Charge transport in organic semiconductors is strongly dependent on the physical and electronic structures at multiple length scales.

### **1.2.2 Molecular Structure**

At the molecular level, the band structure of a material is highly dependent on its molecular structure. Both the moieties present on an organic semiconductor as well as its geometry in both the solvated and solid states will have a strong impact on the energy levels and density of states of its electronic structure. The presence of electron-rich groups increases the energy level of the highest occupied molecular orbital (HOMO) of a given organic semiconductor, while electron-poor groups decrease the energy level of the lowest unoccupied molecular orbital (LUMO). These effects have recently been used in concert to create so-called “donor-acceptor” (DA) copolymers which have significantly smaller band gaps than traditional polymer semiconductors such as polythiophenes.

The presence of substituents, particularly alkyl sidechains on polymers and acetylene-linked silyl groups on polycyclic aromatic hydrocarbons, has a large effect on both the solubility and solid state packing. Bulkier groups tend to increase the solubility, but can have a deleterious effect on solid-state charge transport because of the increased separation between conjugated cores/backbones. However, the careful tuning of side groups can also be used to modify the crystal packing so that there is increased wave function overlap between neighboring molecules. The magnitude of this electronic

coupling is referred to as the transfer integral, with its strength decreasing rapidly with distance.<sup>2</sup> Thus, a tight, carefully aligned packing of molecules is essential for efficient charge transport through a crystal. Alkyl side chains can interact via London dispersion forces to produce a more tightly packed crystal, particularly with a lamellar arrangement. Additionally, inter- and intramolecular interactions such as sulfur-sulfur interactions and hydrogen bonding can increase the tightness of molecular packing in the crystal structure and the planarity of conjugated systems.

### **1.2.3 Morphology**

The morphology of organic semiconductor thin films can be broken into two main components which will be central to this dissertation: crystallinity and connectivity. The crystallinity of a solid is of the utmost importance for charge transport to occur; charge transfer between molecules is critically dependent on the spacing between molecules and the regular tight packing within crystals minimizes the distance that a charge must travel between molecular orbitals. As a corollary, grain boundaries between crystallites, as well as the presence of non-crystalline, amorphous material, are significant barriers to charge transport, as the coupling between molecules across the boundary is significantly lower than that within the crystal.<sup>18-24</sup> In connection with this actuality, the connectivity between crystallites of a polycrystalline material also plays a significant role in transporting charges between crystallites. Polymers have a distinct advantage over semiconducting small molecules in this regard, as “tie chains” can transport charges along their backbones, electronically connecting the crystallites in which they are included (Figure 1.2).

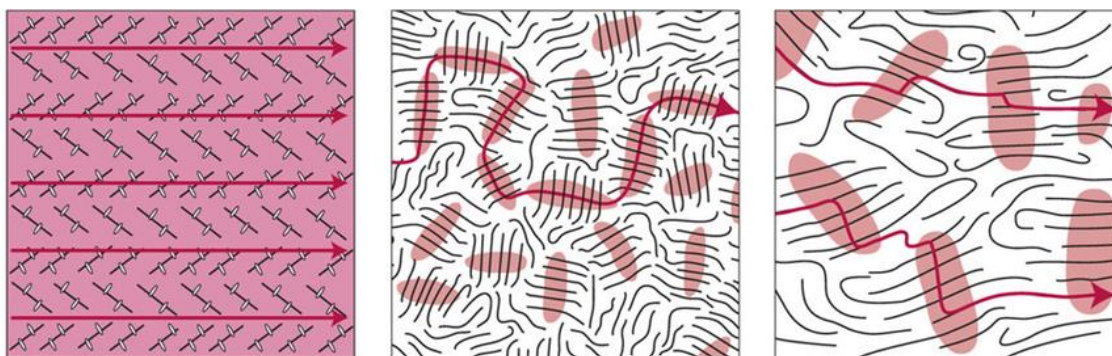


**Figure 1.2** Cartoons depicting charge transport in single crystal, semicrystalline, and primarily amorphous films of organic semiconductors. Reprinted from Podzorov, V. Conjugated polymers: Long and winding polymeric roads. *Nat. Mater.* **12**, 947–8 (2013).<sup>25</sup>

#### 1.2.4 Single Crystal Measurements

By removing the morphological component of a semiconducting solid, which is highly dependent on processing conditions, it is possible to characterize the intrinsic properties of an organic semiconductor in its crystalline state. Thus, single crystals are used to determine the charge transport properties of a material in the absence of morphological defects found in a semicrystalline film. This approach has been used with great success to directly probe the physics of charge transport in small molecule organic semiconductors. Furthermore, organic field effect transistors which use a single crystal as their active layer components exhibit performance which is orders of magnitude higher than their thin film counterparts. This is largely due to the absence of grain boundaries which inhibit charge transport between the electrodes.<sup>18,26,27</sup> Unfortunately, there are currently no generally applicable methods for forming single crystals of polymer semiconductors due to the large entropic barriers of polymer crystallization (Figure 1.3).<sup>28</sup>

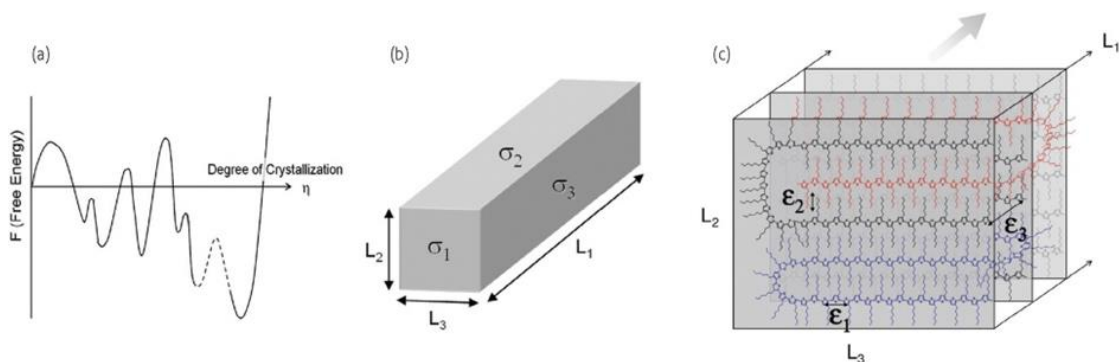


**Figure 1.3** The free energy landscape (a), relation between crystal area, energy, and length (b), and cartoon depicting P3HT chain packing within a crystal (c). Reprinted from Lim, J. A., Liu, F., Ferdous, S., Muthukumar, M. & Briseno, A. L. Polymer semiconductor crystals. *Mater. Today* **13**, 14–24 (2010).<sup>28</sup>

### 1.2.5 The Role of Oligomers

The structure-property relationships of polymers are complex due to the ill-defined nature of a given polymer system. Polymerization results in materials that are inherently disperse in molecular structure, including varying chain lengths and couplings. The properties observed are often a (weighted) average of the molecular structures present, and thus it can be difficult to draw meaningful, broadly applicable conclusions by studying a single system. Additionally, the observed properties are highly dependent on processing conditions, making it difficult to directly correlate the semiconducting properties of a material with its (again, ill-defined) molecular structure. The virtual absence of suitable crystallization methods constitutes an enormous barrier toward producing a reliable method, i.e. single-crystal measurements, for characterizing polymer semiconductors.

Oligomers suffer from essentially none of these shortcomings while maintaining similar molecular structures to their parent polymers. By using a bottom-up synthetic method, akin to small molecule synthesis, their structure can be well-defined without

variations in coupling, regioregularity, or chain length. Furthermore, their short length reduces the entropic barriers of crystallization, and single crystals may be formed from solution. As such, they are excellent model systems for related polymers.

#### **1.4 Dissertation Overview**

This dissertation explores three approaches for using oligomers to characterize their parent polymers. The first study, presented in Chapter 2, is the characterization of a series of well-defined oligomers to observe the transition from monomer to polymer. The knowledge obtained is essential for determining the minimum length at which an oligomer exhibits properties equivalent to the polymer. The second study examines the role that oligomers play when present in polymer thin films. Films of oligomers are known to exhibit poor semiconducting properties, and the research presented in Chapter 4 deconvolutes the molecular charge transport properties from those that are morphological in nature. Finally, in Chapter 5, an approach for fractionating and crystallizing oligomers from an alternative solvent phase, *i.e.* supercritical fluids, is discussed and the resulting crystals are characterized. In total, this dissertation represents a foundation for using oligomers as representative systems for studying semiconducting polymers.

## CHAPTER 2

### CHARACTERIZING THE TRANSITION FROM MONOMER TO POLYMER

#### 2.1 Introduction

Polythiophenes are among the most-researched organic semiconductors due to their excellent combination of good performance, low cost, and high processability for both organic field-effect transistors (OFETs) and organic photovoltaics (OPVs).<sup>15,16,29,30</sup> The performance of these materials is strongly related their solid-state morphology, and this relationship has been the focus of a tremendous number of studies.<sup>23,31–36</sup> While this research has produced invaluable conclusions with regard to the nature of the charge transport in disperse polymer films, it remains challenging to draw definitive conclusions about the intrinsic optical and electronic properties of polymer semiconductors. These challenges arise from the inherent variation in polymer systems: batch-to-batch variations in both the molecules themselves, including chain length and regioregularity, as well as the conditions under which their processed, such as coating techniques/conditions and post-treatment can significantly alter the resulting properties of the material under study.<sup>14,37–39</sup> In order to determine the intrinsic maximum potential of these materials, well-defined systems must be studied.<sup>28</sup>

The variation in the properties of polythiophenes has been observed since they were first synthesized. In 1980, Yamamoto, *et al.*, synthesized unsubstituted polythiophenes by the polycondensation of 2,5-dibromothiophene.<sup>40</sup> They found that, while the polymer exhibited low conductivity ( $10^{-11} \Omega^{-1} \text{ cm}^{-1}$ ), it could be doped with iodine to become conducting ( $10^{-4} \Omega^{-1} \text{ cm}^{-1}$ ). However, the characterization and

application of this material were extremely limited because of its insolubility. To enhance the solubility of this new class of materials, Sato, *et al.*, polymerized thiophenes bearing long alkyl (hexyl, octyl, dodecyl, octadecyl, icosyl) side chains, and found that the resulting polymers were soluble in common organic solvents such as chloroform.<sup>41</sup> Moving forward, Sirringhaus, *et al.*, demonstrated that the molecular structure has strong effects on the morphology and resulting electronic properties of these materials (Figure 2.1).<sup>42</sup> Because the 3-alkylthiophene monomer is asymmetric, a dimer in the polymer can be linked in different configurations: “head-to-tail,” or “head-to-head”/“tail-to-tail.” OFETs fabricated from thin films of spin-coating poly(3-hexylthiophene) (P3HT) exhibited charge carrier mobilities of less than  $10^{-4} \text{ cm}^2 \text{ V}^{-1} \text{ s}^{-1}$  for P3HT with 70% head-to-tail couplings (i.e. 70% “regioregular”), while the mobility of 96% regioregular P3HT was  $\sim 10^{-1} \text{ cm}^2 \text{ V}^{-1} \text{ s}^{-1}$ , an improvement of 3 orders of magnitude. The researchers found that the more regioregular polymer exhibited increased crystallinity, as evidenced by sharper X-ray scattering reflections, and was oriented with the thiophene backbone perpendicular to the surface (“edge-on”), while the less regioregular polymer exhibited more disorder and parallel to the surface (“face-on”).



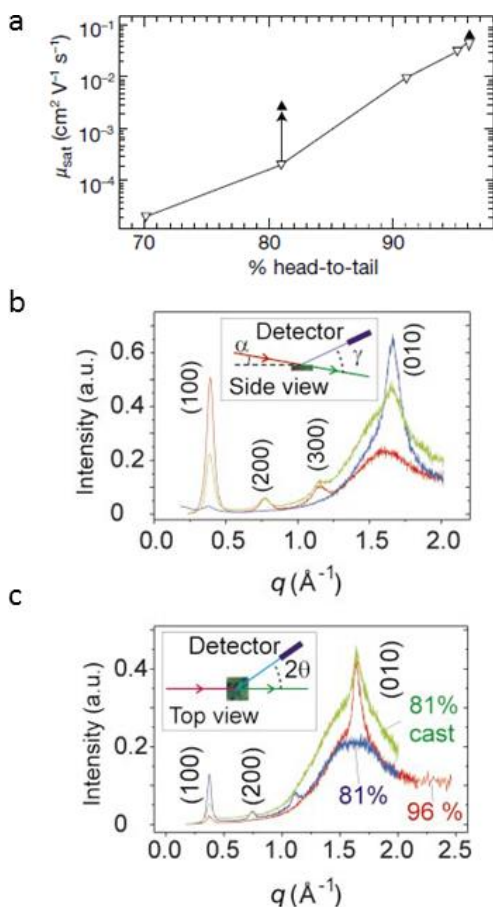


**Figure 2.1** Plot of P3HT mobility as a function of regioregularity (a), out-of-plane (b) and in-plane (c) diffraction of P3HT films with various regioregularities. Reprinted from Sirringhaus, H. *et al.* Two-dimensional charge transport in self-organized, high-mobility conjugated polymers. *Nature* **401**, 685–688 (1999).<sup>42</sup>

Building upon the previous research, Kline, *et al.*, demonstrated that the morphology and electronic properties of P3HT thin films is also highly dependent on the molecular weight of the polymer as well as the processing conditions during casting (Figure 2.2).<sup>23</sup> Films of low molecular weight ( $M_n \sim 3$  kDa) polymer which were spin-cast at 2000 rpm from chloroform exhibited  $\sim 100\times$  lower mobility than those which were drop-cast from chloroform, spin-cast from a solvent with lower vapor pressure (e.g. xylene), or spin-cast and subsequently annealed. For high molecular weight polymer ( $M_n \sim 10\text{-}40$  kDa), this effect was still present, but had a much lower impact, with a difference

of only ~5x in mobility. Additionally, mobility increased monotonically with increasing molecular weight over the range studied. This demonstrated that the intrinsic performance of these materials is strongly convoluted with morphology, making it difficult to assess the true nature of charge transport in these polymeric materials.

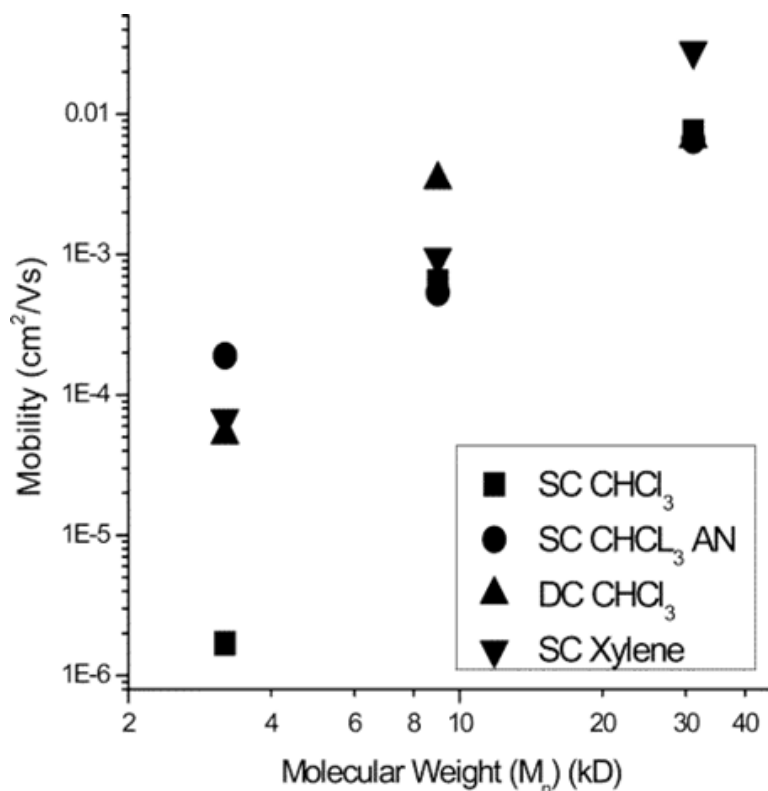


**Figure 2.2** Plot depicting the mobility of P3HT as a function of molecular weight and spin-coating solvent. Reprinted from Kline, R. J. *et al.* Dependence of Regioregular Poly(3-hexylthiophene) Film Morphology and Field-Effect Mobility on Molecular Weight. *Macromolecules* **38**, 3312–3319 (2005).<sup>23</sup>

The variation in morphology, particularly the transition from rod-like crystallites in low molecular weight, slowly deposited films to nodule-like, smooth films of high molecular weight polymer rapid cast by spin coating, was observed and characterized by Verilhac and coworkers (Figure 2.3).<sup>43</sup> Low molecular weight oligomers are not as entropically frustrated by entanglements when being deposited from solution, especially if the kinetics of drying are slow enough for the conjugated materials to self-organize,

such as during drop casting. In contrast, it is difficult for high molecular weight materials to reach a thermodynamic global minimum during deposition due to the free energy landscape, which contains countless local energy minima as there are large barriers to disentanglement and organization over long coherence lengths.

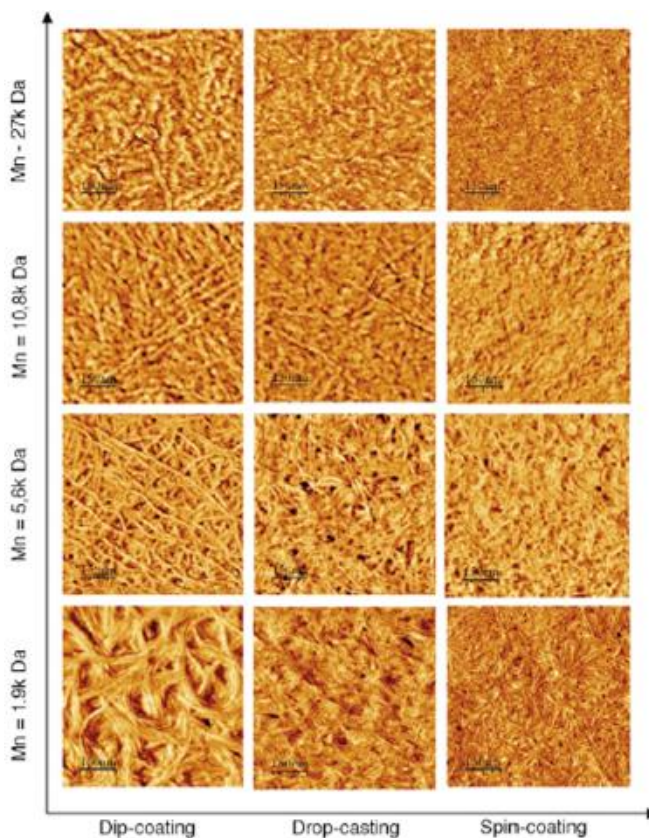


**Figure 2.3** Atomic force micrographs of various morphologies obtained from different molecular weights and coating methods for P3HT. Reprinted from Verilhac, J. M. *et al.* Effect of macromolecular parameters and processing conditions on supramolecular organisation, morphology and electrical transport properties in thin layers of regioregular poly(3-hexylthiophene). *Synth. Met.* **156**, 815–823 (2006).<sup>43</sup>

Oligomers are potentially excellent model systems for their polymer counterparts due to their well-defined molecular structures.<sup>44–49</sup> This strategy has been employed to examine the spectroscopic properties of “ $\beta$ -blocked” oligothiophenes of up to 96 thiophene units in length, revealing a lack of convergence for these highly planar molecules.<sup>47</sup> The evolution of optical and electronic properties of long, 3-octyl-

substituted oligothiophenes was also studied.<sup>48</sup> Additionally, long, polydisperse oligothiophenes (*ca.* 80 thiophene units) were used to characterize polymer packing on highly oriented pyrolytic graphite (HOPG), revealing the nature of the chain packing.<sup>45</sup> Studies such as these have formed a basis for further, more complete investigation of relevant oligothiophenes. A thorough characterization of all of the relevant properties of a series of oligomers is necessary to draw meaningful conclusions about the evolution from small molecule to polymer and fundamental to defining this transition.

For an oligomer of a given length to be representative of a longer polymer, it must mirror a number of significant properties. In particular, the electronic structure, crystal structure, and thin-film packing must align closely with what is known or theorized of the polymer. By characterizing a series of pure oligomers we have determined at what length an oligomer loses some of its small molecule characteristics and begins behaving as the related polymer. This length represents the “shortest polymer” and is an excellent target for further studies to more deeply investigate the intrinsic properties of that polymer family free from the traditional hindrances of such characterizations. The results of this research are expected to benefit both experimentalists, as a well-defined oligomer system is inherently more crystalline and the effects of morphology can be deconvoluted from molecular and crystal structures, and theoreticians will be able to explore the electronic properties of the polymer via techniques such as density functional theory (DFT) calculations while minimizing computational costs.

The optoelectronic properties of conjugated oligomers and polymers are known to evolve with increasing chain length, particular in the low-molecular weight regime. While aromatic systems are generally depicted as planar, the single bonds between

neighboring thiophene rings of polythiophenes allows for freedom of rotation, and this rotation is further increased by the presence of bulky alkyl side chains, drawing the rings out of plane and decreasing the  $\pi$  wavefunction overlap. This results in a deviation of  $E^\theta$  from the expected band gap  $E_g$ . Additionally, the Peierls distortion from bond length alternation along the polymer backbone,  $E^{\delta r}$ , further limits the band gap; the unfavorable energy increase from the longer bonds is outweighed by the increased stability garnered from the lower bonds. Additionally, the aromatic resonance energy,  $E^{Res}$ , effects from electron-rich or electron-poor substituents,  $E^{Sub}$ , and interchain coupling in the solid state,  $E^{int}$ , can further modify the band gap away from the expected planar, isolated state (Figure 2.4).<sup>50</sup>

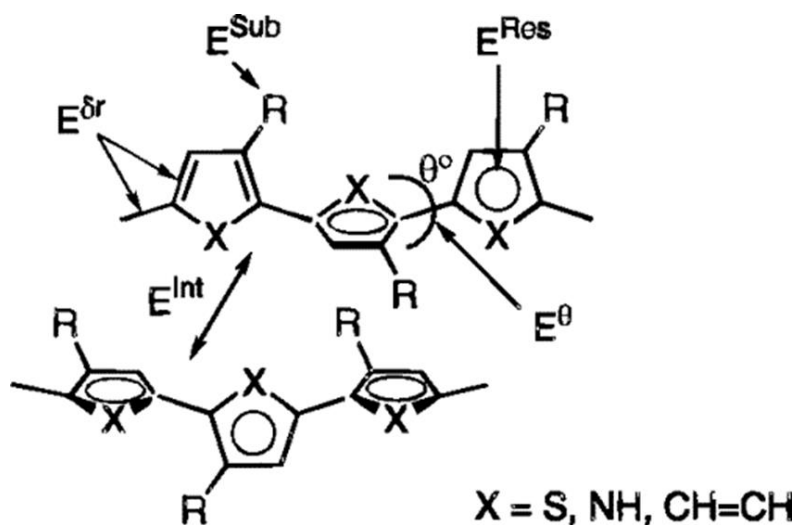


**Figure 2.4** Model illustrating the factors which limit conjugation in conjugated polymers. Reprinted from Roncali, J. *Synthetic Principles for Bandgap Control in Linear  $\pi$ -Conjugated Systems*. *Chem. Rev.* **97**, 173–206 (1997).<sup>50</sup>

The HOMO increases in energy with increasing conjugation length, and the LUMO decreases in energy with increasing conjugation length due to the increased density of states at the frontier orbitals. This has an overall effect of reducing the band gap with increasing conjugation length.

Poly[bis(3-dodecyl-2-thienyl)-2,2'-dithiophene -5,5'-diyl] (PQT-12) is a semicrystalline polythiophene which exhibits mobilities greater than  $0.1 \text{ cm}^2 \text{ V}^{-1} \text{ s}^{-1}$ .<sup>51</sup> In particular, the crystalline nature of the polymer, which improves with annealing, is strongly correlated with the charge transport properties of the material. As such, model systems for PQT-12 crystallites are highly desirable. Here, 3,3''-didodecylquaterthiophene (DDQT) oligomers, which correspond to repeat units of PQT-12, with  $n = 1-6$  are characterized (Figure 2.5). The evolution of crystalline, morphological, and optoelectronic properties with increasing molecular length is analyzed.

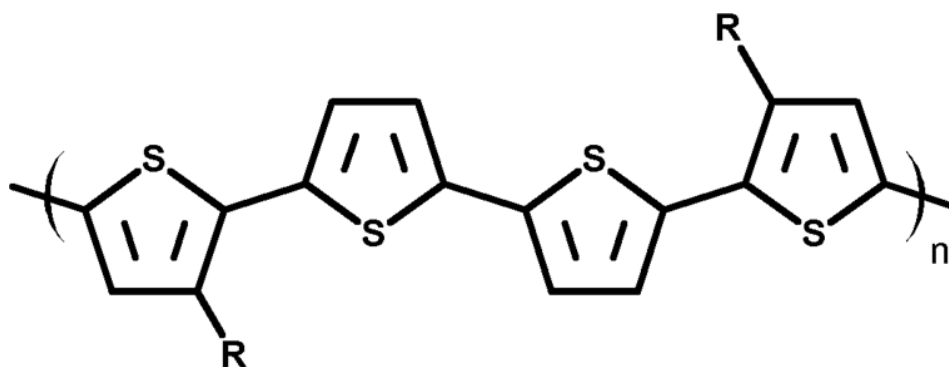


**Figure 2.5** DDQT repeat unit of PQT-12.

## 2.2 Experimental

### 2.2.1 Materials

The oligomers were synthesized by Dr. Lei Zhang *via* Stille coupling (Figure 2.6).<sup>52</sup> All chemicals were purchased from commercial suppliers and used without further purification. The monomer, didodecyl-2,2':5',2'':5'',2''':5''',2''''-quaterthiophene, was synthesized according to the literature.<sup>44</sup> Building blocks were brominated with *n*-bromosuccinimide (NBS) or stannylated with *n*-butyl lithium followed by trimethyltin chloride. The Stille coupling steps used  $\text{Pd}(\text{PPh}_3)_4$  as a catalyst. All solvents used during

the synthesis and characterization were purchased from Fisher Scientific and were used without further purification. Silicon wafers were purchased from Addison Engineering.

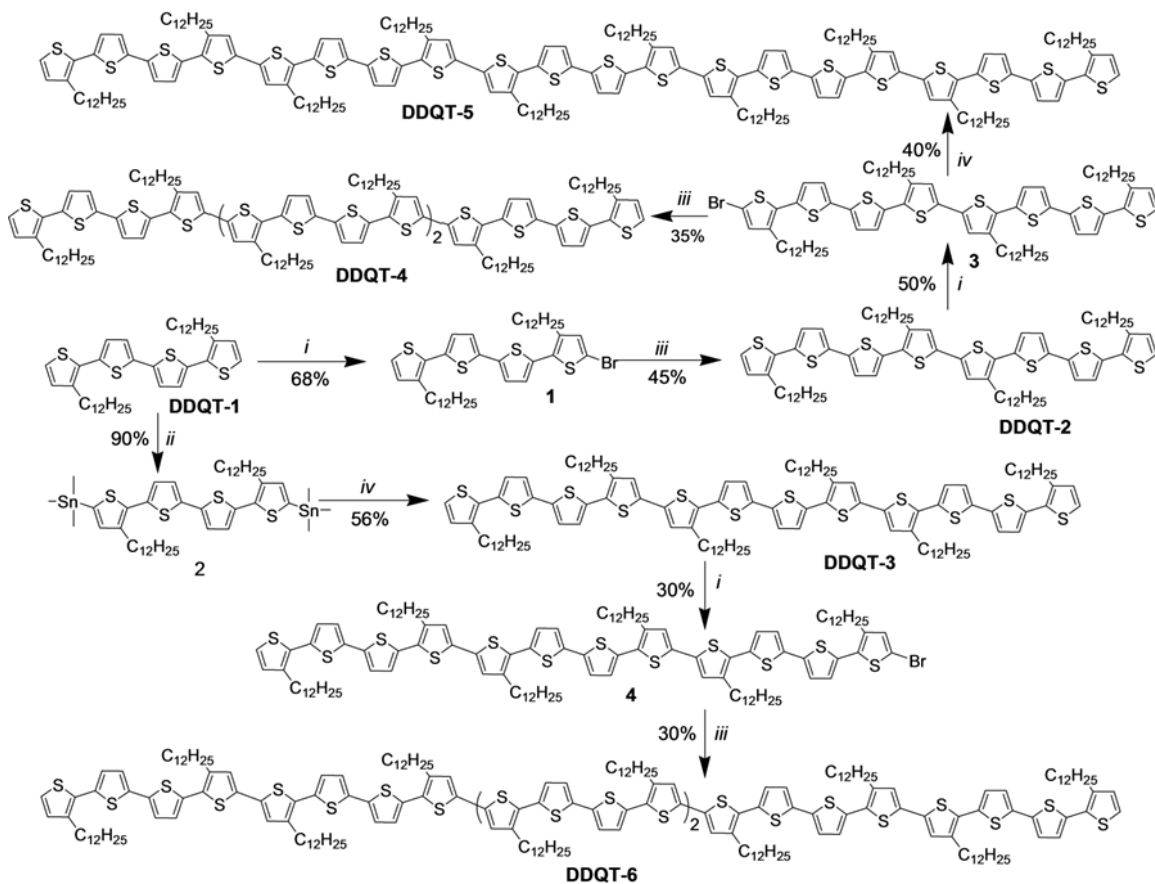


**Figure 2.6** Scheme for the synthesis of DDQT oligomers. Reagents and Conditions: (i) NBS, AcOH/chloroform (1:1), 0 °C to room temperature; (ii) BuLi, trimethyltin chloride, THF, -78 °C to room temperature; (iii) bis(tri-*n*-butyltin), Pd(PPh<sub>3</sub>)<sub>4</sub>, toluene, 115 °C; (iv) **2**, Pd(PPh<sub>3</sub>)<sub>4</sub>, toluene, 115 °C; (v) **1**, Pd(PPh<sub>3</sub>)<sub>4</sub>, toluene, 115 °C.<sup>52</sup>

## 2.2.2 Methods

Matrix-assisted laser desorption ionization time-of-flight (MALDI-TOF) mass spectrometry was performed using a Bruker Biflex III mass spectrometer with terthiophene as matrix. Samples were prepared by mixing equal volumes of 25 mg/mL terthiophene in chloroform with 0.1 mg/mL sample in chloroform and drop casting the mixed solution onto a polished steel target plate. Linear ion mode was used with a 25 kV accelerating voltage.

Differential scanning calorimetry (DSC) measurements were taken using a TA Instruments Q1000 DSC with heating and cooling rates of  $10 \text{ K min}^{-1}$  under a flow of nitrogen. Approximately 5 mg of material was loaded into an aluminum pan which was subsequently hermetically sealed.

Single crystal structure determination *via* X-ray diffraction was performed by Dr. Sean Parkin at the University of Kentucky.

A JEOL JEM-2000FX transmission electron microscope (TEM) was used for TEM imaging and selected-area electron diffraction (SAED). CrystalMaker software was used to calculate electron diffraction patterns from the unit cell of the bulk crystal structure.

Grazing-incidence X-ray diffraction was performed by Dr. Feng Liu at the Stanford Synchrotron Radiation Lightsource (SSRL) on beam lines 2-1, and 11-3.

Atomic force microscopy (AFM) images were obtained using a Veeco Dimension 3100 AFM in tapping mode with a scan rate of 1 Hz. Samples were prepared by spin coating the materials from a 2 mg/mL chloroform solution at 2000 rpm for 30 sec onto silicon wafers with a 300 nm thermal oxide ( $\text{SiO}_2$ ) surface layer which were cleaned with detergent, deionized water, acetone, and isopropanol, then treated by UV-ozone for 10 minutes.

Ultraviolet photoelectron spectroscopy (UPS) measurements were performed using an Omicron Nanotechnology Electron Spectroscopy for Chemical Analysis Instrument (ESCA+S) with a He laser (1  $\alpha$  emission line). Samples were spun cast from a 2 mg/mL chloroform solution at a rate of 2000 RPM for 30 sec onto doped conducting silicon wafers, cleaned with detergent, deionized water, acetone, and isopropanol, then



treated by UV-ozone for 10 minutes, with a 50 nm silver layer thermally evaporated onto the surface immediately before spin coating.

Ultraviolet-visible (UV-vis) spectroscopy was performed using a Shimadzu 3600 UV-VIS-NIR spectrophotometer. Solutions of the materials under study were dissolved in chloroform and their concentrations adjusted to produce absorbances of 0.3 – 1.0. The path length of the quartz cuvettes used was 1 cm.

Semi-empirical quantum mechanical simulations were performed using the ArgusLab software suite. The Parameterized Model number 3 (PM3) method was used for geometry optimization and the simulations were run in a closed shell (RHF) configuration until a solution converged at  $10^{-10}$  kcal/mol.

## **2.3 Results and Discussion**

### **2.3.1 Evaluating oligomer molecular weight and purity**

To ensure the purity and molecular structure of the synthesized oligomers, gel permeation chromatography (GPC) and matrix-assisted laser desorption ionization time-of-flight (MALDI-ToF) mass spectrometry were used to characterize the oligomers. The results show that the oligomers are truly monodisperse with the expected molecular weights (667 Da per repeat unit) (Table 2.1). However, DDQT-6 may have some slight high molecular weight impurities. This result is critical to validate the remainder of the results, as the goal of this research is to characterize the pure oligomers and their differences in thermal, crystalline, morphological, and optoelectronic properties.

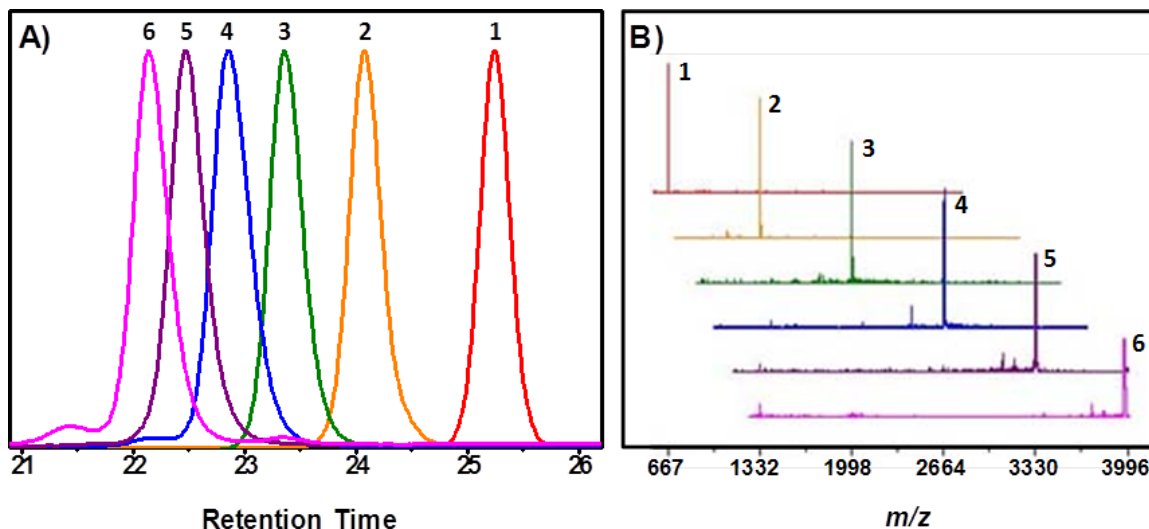


**Figure 2.7** Gel permeation chromatography traces (A) and MALDI-ToF spectra for DDQT oligomers.

**Table 2.1** MALDI-ToF expected molecular weights, observed molecular weights, and molecular weights and polydispersity index (PDI) determined by gel permeation chromatography (GPC).

Material	MS <sub>calc</sub> (m/z)	MS <sub>expt</sub> (m/z)	GPC (M <sub>n</sub> )	PDI
DDQT-1	667.15	666.60	649	1.01
DDQT-2	1332.67	1334.55	2284	1.01
DDQT-3	1997.41	1997.58	4694	1.01
DDQT-4	2662.15	2664.49	6456	1.02
DDQT-5	3327.68	3329.13	7404	1.01
DDQT-6	3992.18	3994.23	10753	1.02

### 2.3.2 Characterization of crystallinity and thermal properties

Long polythiophenes are exceptionally difficult to crystallize because of the entropic frustration associated with the chain rearrangement of the entangled polymers. While numerous positive intermolecular interactions, including  $\pi$ - $\pi$  interactions and van der Waals forces, induce crystallinity, the overall crystallinity is limited because of the large energetic barriers encountered when assembling large crystals from small, metastable crystallites.<sup>28</sup> Due to these conditions, polythiophene systems are generally classified as semicrystalline.

Small molecule semiconductors are not limited by the same entropic penalties associated with semiconducting polymers and the shorter oligothiophenes fall within this regime. The transition from small molecule oligomer (i.e. monomer) to frustrated polymer was characterized by differential scanning calorimetry (DSC) (Figure 2.8). From DDQT-1 to DDQT-3, the melting points ( $T_m$ ) steadily increased, although the melting enthalpy ( $\Delta H_m$ ) for DDQT-2 is substantially lower than DDQT-1 or DDQT-3. The unique crystal structure of DDQT-2, discussed below, contains bent alkyl side chains; this packing frustration may account for the lower overall crystallinity relative to DDQT-1 and DDQT-3. More importantly, a sharp drop in melting enthalpy is observed between DDQT-3 and DDQT-4, and this change in crystallinity is concurrent with the appearance of a second melting peak, indicating a phase transition. This behavior is indicative of the development of a liquid crystalline phase, and has been observed in other liquid crystalline systems.<sup>53</sup> The two endotherms correspond to the crystalline-to-liquid crystalline and liquid crystalline-to-isotropic(liquid) phase transitions, respectively. The alkyl side chains melt first, resulting in a liquid crystalline system, while the backbones melt at a higher temperature. The temperatures and enthalpies of melting and crystallization temperatures of the oligomers are summarized in Table 2.2. DDQT-4 through DDQT-6 exhibit two distinct melting endotherms, as noted.

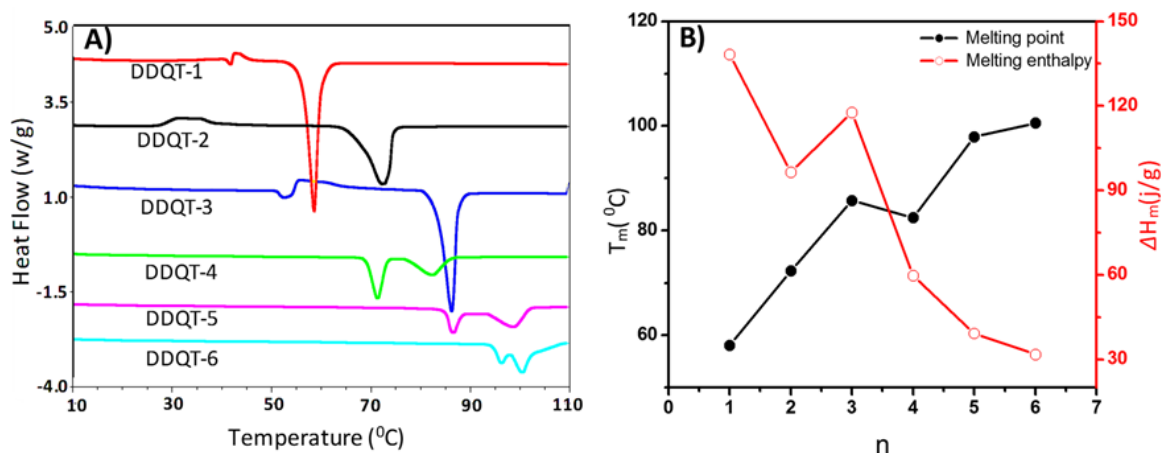


**Figure 2.8** Differential scanning calorimetry traces (second heating cycle) for DDQT-1 through DDQT-6 (endo down) (a) and a plot of melting point and enthalpy of melting as a function of oligomer length (b).

**Table 2.2** Melting and crystallization temperatures as well as the enthalpy of melting for DDQT-1 through DDQT-6.

Material	$T_m$ (°C)	$T_c$ (°C)	Enthalpy of melting (J/g)		
<b>DDQT-1</b>	58.59	17.71	138.3		
<b>DDQT-2</b>	72.34	15.85	96.46		
<b>DDQT-3</b>	86.25	29.06	117.7		
<b>DDQT-4</b>	71.29	82.53	53.49	32.66	27.19
<b>DDQT-5</b>	86.39	98.98	68.4	14.61	24.67
<b>DDQT-6</b>	95.95	100.67	77.68	7.15	24.72

These results indicate that a significant change in crystal packing and morphology occurs between DDQT-3 and DDQT-4. Additionally, the melting points and enthalpies continue to gradually rise and fall, respectively, from DDQT-4 to DDQT-6, suggesting that there is increased frustration in crystallizing the longer oligomer chains, as expected, but the nature of the packing does not significantly change beyond DDQT-4. Of particular note, the enthalpy of disrupting the polymer backbone interactions (i.e. melting) is essentially constant for DDQT-4 through DDQT-6, indicating that their overall order in the system is not changing significantly after the tetramer.

### 2.3.3 The evolution in crystal structure for short oligothiophenes

The predominant intermolecular interaction in unsubstituted aromatic systems is between the  $\pi$  electron cloud on the faces of the aromatic rings and the hydrogens of the peripheral C-H bonds. This interaction is present for unsubstituted thiophenes, resulting in a molecular packing of a herringbone structure within crystals. However, the alkyl side chains functionalized thiophenes interrupts this edge-to-face interaction, as the bulky groups prevent neighboring backbones from tightly packing in that fashion. Additionally, van der Waals forces between alkyl chains draw them to each other, producing a supplemental intermolecular interaction which must be accounted for in the crystal packing. This alkyl-alkyl interaction supports a lamellar arrangement of polymer backbones, with interacting (poly/oligo)thiophene stacks alternating with the alkyl side chain domains.

This interplay between edge-to-face and alkyl-alkyl interactions is particularly evident in examining the crystal structure of DDQT-2 (Figure 2.9). The molecules pack in a “lamellar herringbone” motif in which the backbones retain their unsubstituted-like herringbone packing, while the alkyl side chains pack together, with some of the terminal methyl groups even unfavorably bent out of plane. This relatively strange conformation also includes terminal thiophene rings which are *syn* to one another, while all of the other thiophenes along the backbone are *anti*. In contrast, DDQT-3 packs in a lamellar motif that is similar to that of the polymer. However, the “small molecule nature” of the oligomer is still present, with torsion angles as high as  $60^\circ$  for the terminal thiophene units, which are also *syn* to the neighbors. This packing structure may be stabilized by the numerous intermolecular interactions present at the four terminal thiophene rings at each

end of the oligomer, particularly C-H, S-H, and H-H interactions. However, the central thiophenes are all *anti* to one another (Figure 2.10). From this observation, it is concluded that quaterthiophenes must be at least three repeat units long to begin to obtain the conformation of the polymer. For oligomer of this length or longer, the majority of alkyl side chains will be in the *anti* configuration, mirroring that of the polymer.

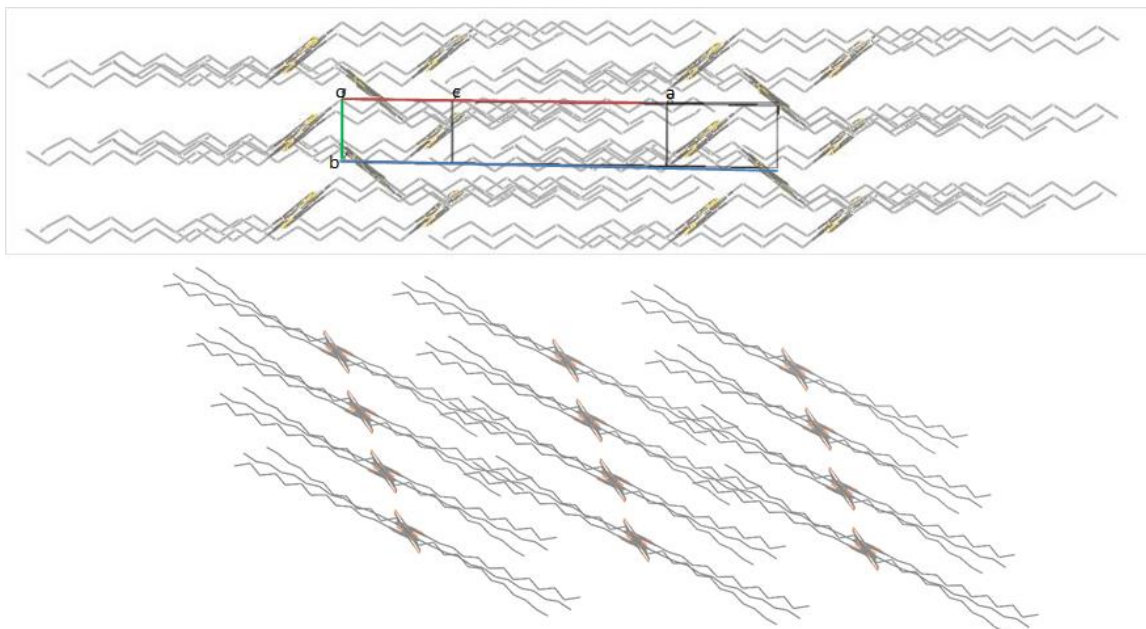


**Figure 2.9** DDQT-2 (top) and DDQT-3 (bottom) crystal structures, as viewed down the *c* axis, demonstrating the change in packing motif from “lamellar herringbone” to a lamellar structure.

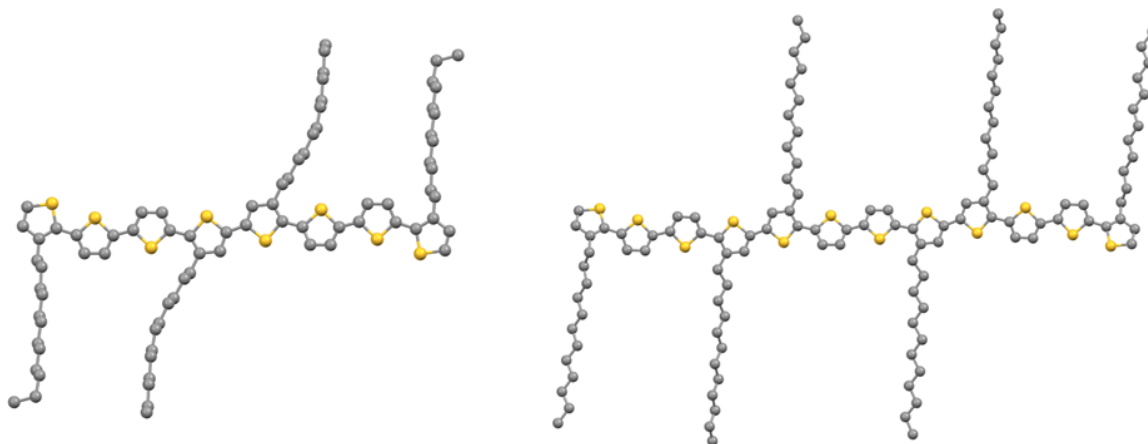


**Figure 2.10** DDQT-2 (left) and DDQT-3 (right) molecules within their respective crystal structures. The *syn* thiophene conformations are observed at the ends of both molecules, however the *anti* conformation is observed for thiophenes in the center of DDQT-3. Additionally, the terminal methyl groups of DDQT-2 are observed to be bent in an energetically unfavorable configuration.

### 2.3.4 Characterization of DDQT-3 single crystal by transmission electron microscopy

Single crystals of DDQT-3 were grown via the slow addition of ethanol to a hexane solution (3:1). These crystals were analyzed by selected area electron diffraction (SAED) transmission electron microscopy (TEM) (Figure 2.11). The diffraction pattern was characterized and correlated with the predicted diffraction pattern of the bulk crystal structure; excellent agreement between the expected and experimentally determined patterns was observed. The *a* and *b* lattice constants were determined to be 9.191 Å and 13.558 Å, respectively, in excellent agreement with those reported by Azumi *et al.* of 9.617 Å and 13.895 Å, respectively.<sup>54</sup> Additionally, the angle between the lattice vectors was observed to be 66.1°, in good agreement with the reported value of 72.9° for the bulk crystal.

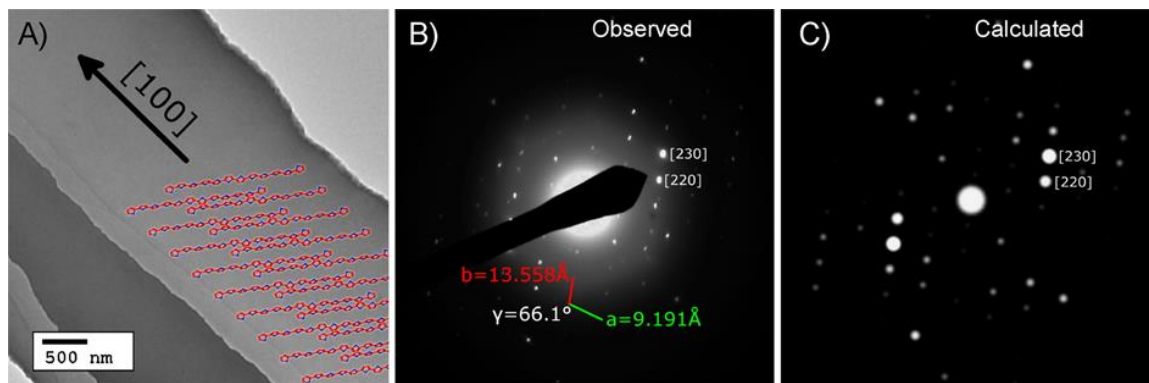


**Figure 2.11** Transmission electron micrograph of a DDQT-3 crystal belt with an overlay of the molecular packing (alkyl side chains removed for clarity) (A), selected area electron diffraction from the crystal (B), and SAED pattern calculated from the bulk crystal structure (C).

Correlating the observed crystal lattice with the crystal habit, the long axis of the crystal corresponds to the [100] direction, indicating that the major  $\pi$ - $\pi$  stacking direction is aligned with the crystal axis. This is in good agreement with the crystal packing of other conjugated materials, with the high-energy  $\pi$  face exhibiting the fastest growth, and thus longest axis of the crystal.<sup>55</sup> However, in contrast to the crystal orientation in small molecule conjugated crystals, such as hexathiapentacene, phthalocyanines, and hexabenzocoronenes, the molecular axis is tilted  $\sim 25^\circ$  with respect to the crystal axis for DDQT-3.<sup>56,57</sup> This off-axis tilt is due to the “slip” (lateral translation) of oligothiophene backbones relative to one another to maximize the positive interactions and accommodate the bulky alkyl side chains. This slip limits the total molecular orbital overlap, in turn limiting the charge transport through the crystal.

### 2.3.5 Characterization of DDQT oligomer packing in thin films

The most common organic semiconductor devices (transistors and photovoltaics) typically utilize a thin layer of less than 100 nm of semiconductor material for their charge-transporting layers. Furthermore, large interfacial effects as well as kinetic



trapping can cause the molecular packing in thin films to differ substantially from that observed in the bulk crystal structure. Because of this, the characterization of molecular packing in thin films is extremely important for understanding the electronic behavior of these materials.<sup>19,58-60</sup> Grazing incidence X-ray diffraction (GIXD) allows one to probe the packing of molecules in their thin film state and was used to probe the crystal packing of DDQT oligomer films spun onto silicon substrates (Figure 2.12).

The highly crystalline nature of DDQT-1 and DDQT-2 is very apparent from their diffractograms. DDQT-1 exhibits peaks which correspond well with the  $a$  and  $b$  axes of the bulk crystal structure, suggesting that no polymorphism is present and the crystals are in the equilibrium state. Indexing the peaks, the in-plane unit cell was compatible with the bulk crystal structure ( $a = 5.59 \text{ \AA}$ ,  $b = 12.27 \text{ \AA}$ ,  $\gamma = 100.7^\circ$ ) with  $a = 5.04 \text{ \AA}$ ,  $b = 12.85 \text{ \AA}$ , and  $\gamma = 98.3^\circ$ . In agreement with the crystal structure obtained for DDQT-2, the thin film diffraction exhibits peaks characteristic of a herringbone structure, as the first two in-plane diffraction peaks are not observed. Additionally, the (100) and higher order reflections are indicative of the spacing observed in the bulk crystal structure (*ca.*  $24 \text{ \AA}$ ).

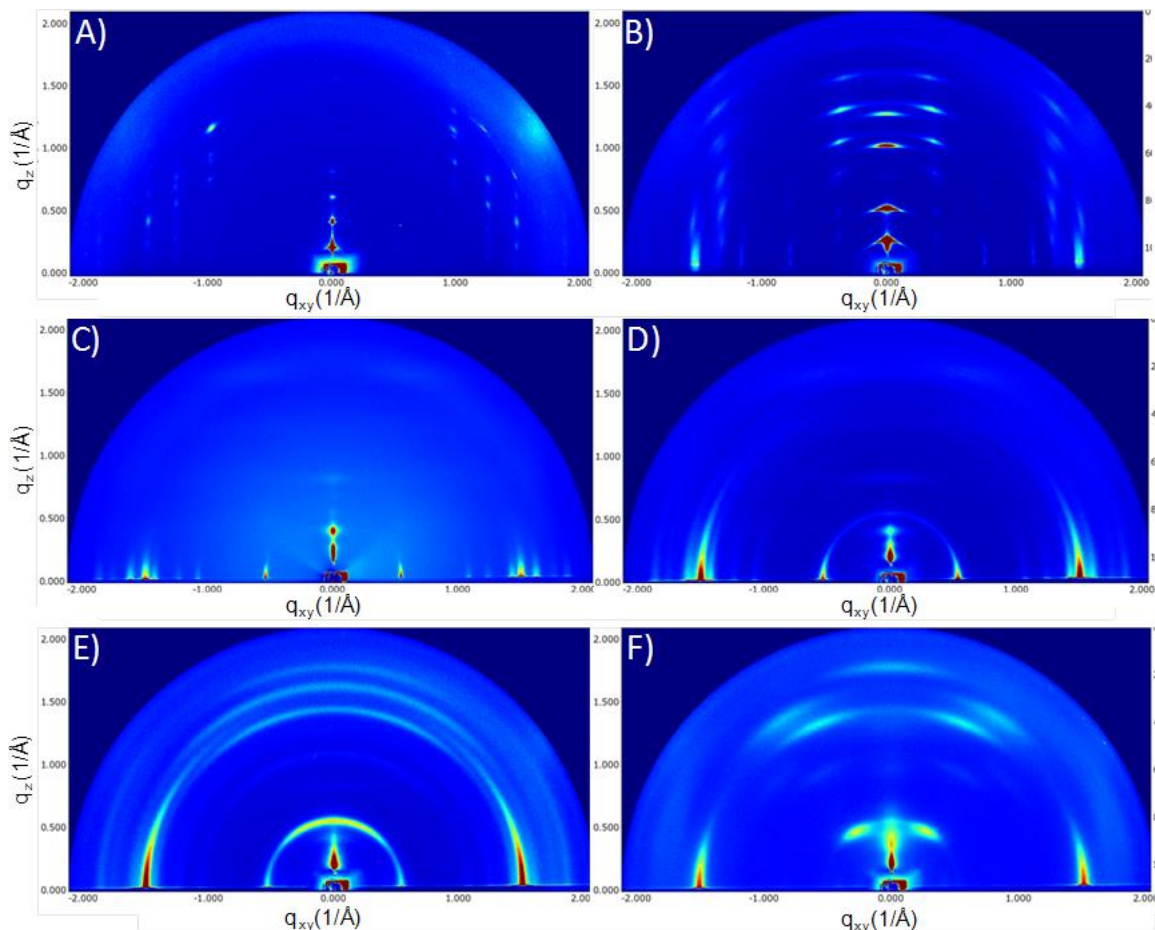


**Figure 2.12** Grazing incidence X-ray scattering of DDQT 1 to DDQT-6 films (a-f), respectively.

In contrast, the spectrum obtained from thin films of DDQT-3 is characteristic of an, albeit weak, lamellar order. The most prominent reflections are observed in-plane. Of special note, the peak located at  $1.62 \text{ \AA}^{-1}$  corresponds to  $3.87 \text{ \AA}$  in real space, which is the  $\pi$ - $\pi$  stacking distance. As the oligomers increase in length for DDQT-4-DDQT-6, this peak becomes more prominent, as it is the strongest interaction in more weakly crystalline systems, and is increasingly misoriented as the crystallites become smaller and less aligned with the substrate. In comparison to the previously reported GIXD spectra for PQT-12, the oligomers are substantially more crystalline.<sup>51</sup> In particular, the in-plane  $\pi$ - $\pi$  reflection at  $1.62 \text{ \AA}^{-1}$  remains intense, even for DDQT-6, the least crystalline

oligomer, while that reflection is slight for unannealed PQT-12 films, increasing slightly upon annealing. The out-of-plane reflection at  $1.50 \text{ \AA}^{-1}$ , which is most prominent in DDQT-5, is also the most conspicuous in as-cast PQT-12 films, suggesting that the packing and orientation of DDQT-5 crystallites is similar to that of PQT-12, although DDQT-5 is significantly more crystalline. In contrast to the previously discussed results, these data suggest that DDQT-5 or higher is more representative of the polymer, while DDQT-3 and DDQT-4 do not exhibit similar morphology to that of the polymer.

### **2.3.6 Characterization of morphology by atomic force microscopy**

Atomic force microscopy (AFM) was used to evaluate the surface morphology of DDQT oligomer thin films spun onto  $\text{SiO}_2$  (Figure 2.13). Micrographs DDQT-1 films displayed large, flat crystals which dominated the surface morphology. DDQT-2 films exhibited a terraced morphology which is indicative of a high degree of order. The monomolecular steps between terraces suggested that there was a high degree of crystallinity within these films, although charge transport may be limited at the grain boundaries between crystallites. Films of DDQT-3 and DDQT-4 exhibited significant roughness which may be attributed to a large number of smaller crystallites. AFM of DDQT-5 films revealed an exceptional surface morphology with micrometer-long, narrow crystallites. A closer scan reveals fibrils approximately 7 nm in width, which is equivalent to the contour length of a fully extended DDQT-5 backbone (Figure 2.14). Although no long-range order was observed, this locally ordered morphology suggested that DDQT-5 readily assembled into nanostructures which may be good model systems for the crystallites present in PQT-12 films. However, this fine structure is lost in DDQT-6 films. These data suggest that DDQT-5 oligomers may pack in their fully

extended conformation to produce well-ordered films while DDQT-6 is too long to maintain a fully extended, tightly packed morphology.

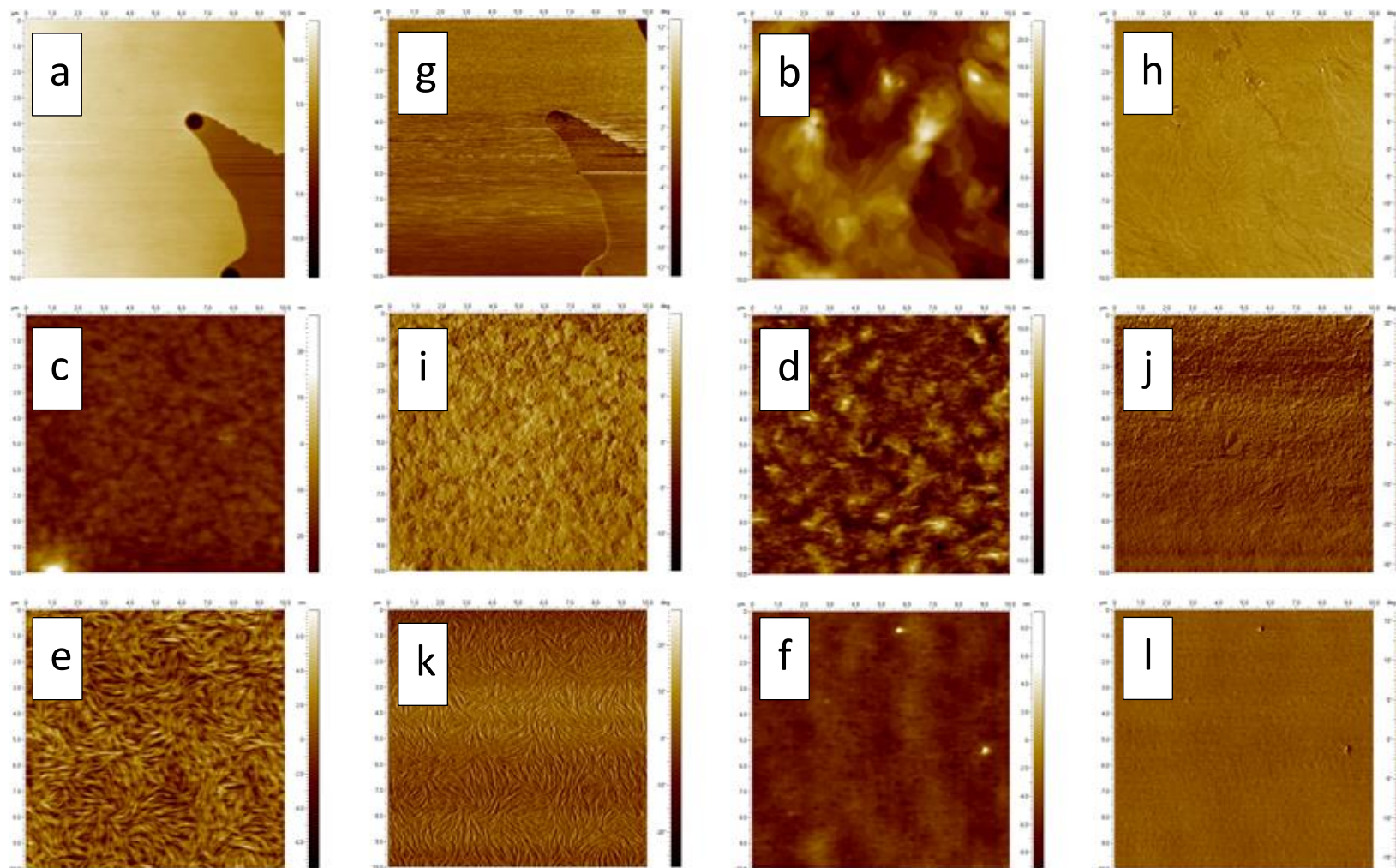


**Figure 2.13** Height (a-f) and phase (g-l) atomic force micrographs (10 μm x 10 μm) of DDQT-1 through DDQT-6 films, respectively.

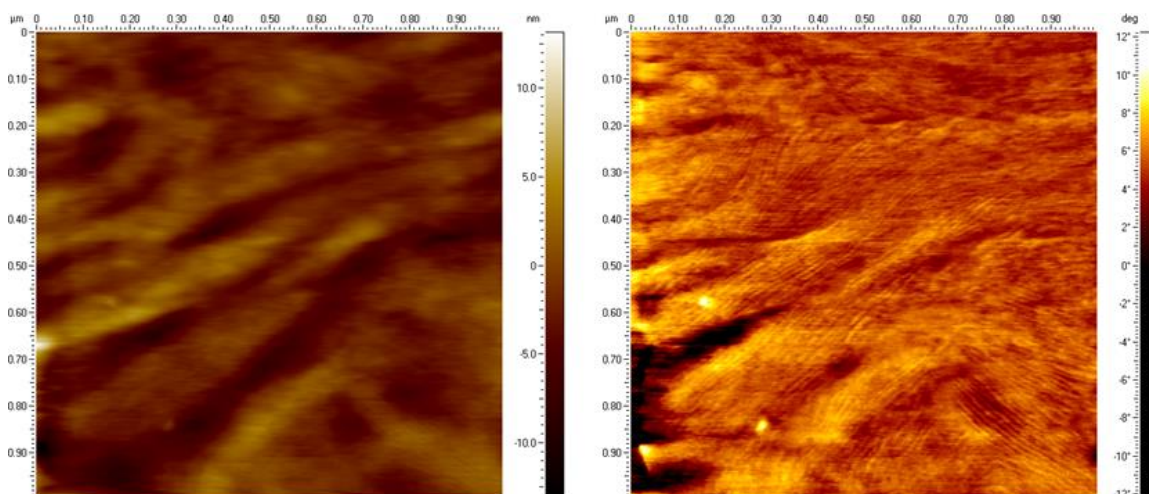


**Figure 2.14** Atomic force micrographs of DDQT-5 films, 1  $\mu\text{m}$  x 1  $\mu\text{m}$ , height (left) and phase (right). A lamellar morphology with a spacing of *ca.* 7 nm is observed, particularly in the lower right region of the phase contrast micrograph; these crystallites may comprise the fibrils observed in larger area scans.

### 2.3.7 Determination of ionization potentials of DDQT thin films

To evaluate the change in the energy levels of DDQT oligomers in the solid state, ultraviolet photoelectron spectroscopy (UPS) was used to measure the ionization potential (IP) (Figure 2.15). The IP is generally equated with the highest occupied molecular orbital (HOMO) energy level.<sup>61</sup> The IP is observed to fall (often depicted as a rising HOMO level) with increasing conjugation from DDQT-1 to DDQT-6. A slight drop is observed for DDQT-4, which may be attributed to a change in molecular packing and intermolecular coupling as observed via GIXD. Additionally, saturation of the energy levels are observed as the oligomers increase in length, with a 0.3 eV shift from DDQT-1 to DDQT-2, and only a 0.1 eV shift from DDQT-5 to DDQT-6 (Table 2.3).

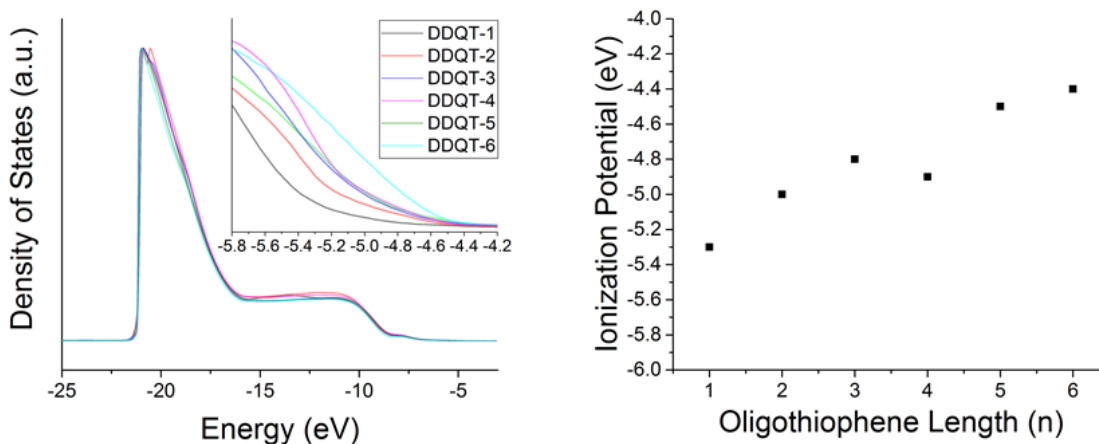


**Figure 2.15** Ultraviolet photoelectron spectra (left) and a plot of ionization potential as a function of DDQT oligomer length.

**Table 2.3** Ionization potentials of DDQT oligomers as determined by UPS.

Material	Ionization Potential (eV)
DDQT-1	-5.3
DDQT-2	-5.0
DDQT-3	-4.8
DDQT-4	-4.9
DDQT-5	-4.5
DDQT-6	-4.4

### 2.3.8 Evolution of optoelectronic properties and determination of effective conjugation length

While the morphology will have strong effects on the properties of a material under study, the electronic structure remains the basis of charge transport; for an oligomer to be truly representative of the polymer, the electronic structures must be equivalent. The optoelectronic properties of polymer semiconductors are their defining features and are the primary design criteria in the development of new molecular semiconductors. Thus, determining when the DDQT oligomers reach a sufficient length to be equivalent to PQT-12 in their orbital delocalization is essential to finding an appropriate model oligomer.

The aforementioned limitations on conjugation due to the Peierls instability and torsion between neighboring thiophene rings cause the orbital delocalization to saturate after a given length. This restricted delocalization in polymer semiconductors leads to a molecular distance, known as the effective conjugation length,  $n_{ecl}$ , after which further lengthening of the polymer chain does not affect the optoelectronic structure; an oligomer of this length or longer is optoelectronically commensurate with the polymer.

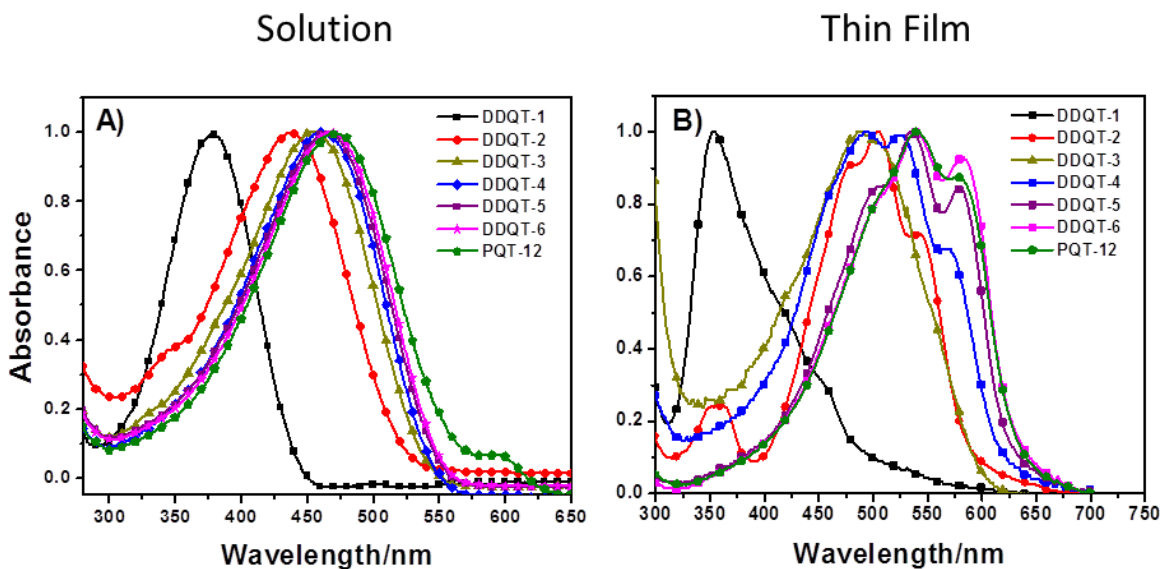


**Figure 2.16** Normalize UV-vis spectra for solutions and thin films of DDQT oligomers.

**Table 2.4** Wavelengths of maximum absorbance and the optical band gaps for solutions and thin films of DDQT oligomers.

Oligomer	$\lambda_{\max}$	$\lambda_{\max}$	$E_g$	$E_g$
	(nm) solution	(nm) thin film	(eV) solution	(eV) thin film
DDQT-1	378	355	2.82	2.59
DDQT-2	436	478, 506, 542	2.31	2.14
DDQT-3	457	492	2.30	2.11
DDQT-4	465	491, 523, 568	2.28	2.03
DDQT-5	468	538, 580	2.26	1.96
DDQT-6	470	540, 580	2.25	1.96



The most facile method for probing the optoelectronic structures of conjugated materials is optical spectroscopy, and this technique was used to characterize the evolution in band structure with increasing molecular length (Figure 2.16) (Table 2.4). The change in energetic levels of the frontier orbitals, *i.e.* highest occupied molecular orbital (HOMO) and lowest unoccupied molecular orbital (LUMO), as well as the resulting band gap, are the direct results of the increasingly delocalized wavefunctions with increasing molecular length. According to classic Kuhn theory, this relationship between band gap and oligomer length,  $n$ , can be modeled by

$$E_{abs}(n) = V_0 + \left( \frac{h^2}{4mL_0^2} - \frac{V_0}{4} \right) \frac{1}{n + 0.5}$$

Where  $h$  is Planck's constant,  $m$  is the mass of an electron,  $L_0$  is the average length of a conjugated bond, and  $V_0$  is a correction factor for the Peierls distortion.<sup>62</sup> This model is accurate for the shorter oligomers, up to DDQT-4, giving a linear relationship of  $E_{abs}$  (eV) = 3.48/ $n$  + 2.42; the change in absorption with increasing conjugation length, *i.e.* the slope, of 3.48/ $n$  is similar to that for unsubstituted polythiophenes (3.76/ $n$ ).<sup>63</sup> Unfortunately, this treatment does not hold for higher molecular weight oligomers and polymers, and a clear deviation from linearity is observed for the DDQT series. Furthermore, it predicts an absorption of 2.42 eV for PQT-12, significantly smaller than the experimental value 2.68 eV which was measured for the high molecular weight polymer ( $M_n = 28$  kDa). This is because the Kuhn formulation does not account for the inherent flexibility of the oligomers, *i.e.* out-of-plane torsion, and the resulting saturation is energy absorption; it essentially neglects the phenomenon of effective conjugation length.

Fortunately, an empirical relationship was discovered by Meier, *et al.*, in which the change in the energy of maximum absorption and oligomer length is treated as an exponential decay between the absorption of the monomer and polymer.<sup>64</sup> This relationship can be expressed as:

$$\lambda_{max}(n) = \lambda_{\infty} - (\lambda_{\infty} - \lambda_1)e^{-b(n-1)}$$

If one sets the wavelength of maximum absorption,  $\lambda_{max}$ , to within 1 nm (the resolution of most commercial spectrometers) of the infinite polymer,  $\lambda_{\infty}$ , and solves for  $n$ , the effective conjugation length can be determined:

$$n_{ecl} = \frac{\ln(\lambda_{\infty} - \lambda_1)}{b} + 1$$

In the DDQT series of oligomers, the wavelength of maximum absorption for a single thiophene monomer,  $\lambda_1$ , was 278 nm, while the wavelength of maximum absorption for the polymer,  $\lambda_{\infty}$ , was 470 nm. Fitting the data to this model, the convergence factor  $b$  is calculated to be 0.246. This treatment yield an effective conjugation length of 22.4 thiophene units, which corresponds to a length approximately midway between DDQT-5 and DDQT-6.

This analysis can be extended to other oligomeric systems and compared to analyze the relative planarity of different thiophene-based polymers (Figure 2.17) (Table 2.5). The molecular structure of poly[2,5-bis(3-dodecylthiophen-2-yl)thieno[3,2-*b*]thiophene] (PBTTT) is comparable to PQT-12, with dodecyl-bearing thiophenes flanking a central thienothiophene fused aromatic core comprising the monomer. Upon initial analysis, this structure might be expected to increase the planarity of the polymer due to the fused central rings, increasing the effective conjugation length. Oligomers of BTTT ( $n = 1-5$ ) were synthesized and characterized by the same methods used to

characterize the DDQT oligomers. It was found that the effective conjugation length of the BTTT oligomers was actually slightly lower ( $n_{ecl} = 21.6$ ) than that of the DDQT oligomers. This surprising result is likely due to the increased torsion along the backbone between the thienothiophene and neighboring thiophene rings. Semi-empirical quantum mechanical simulations were performed to evaluate this hypothesis, and they revealed that there is a significant amount of torsion, with the thienothiophene and thiophene rings being *syn* to one another, with a twist angle of  $47^\circ$  in the lowest energy conformation (Figure 2.18).

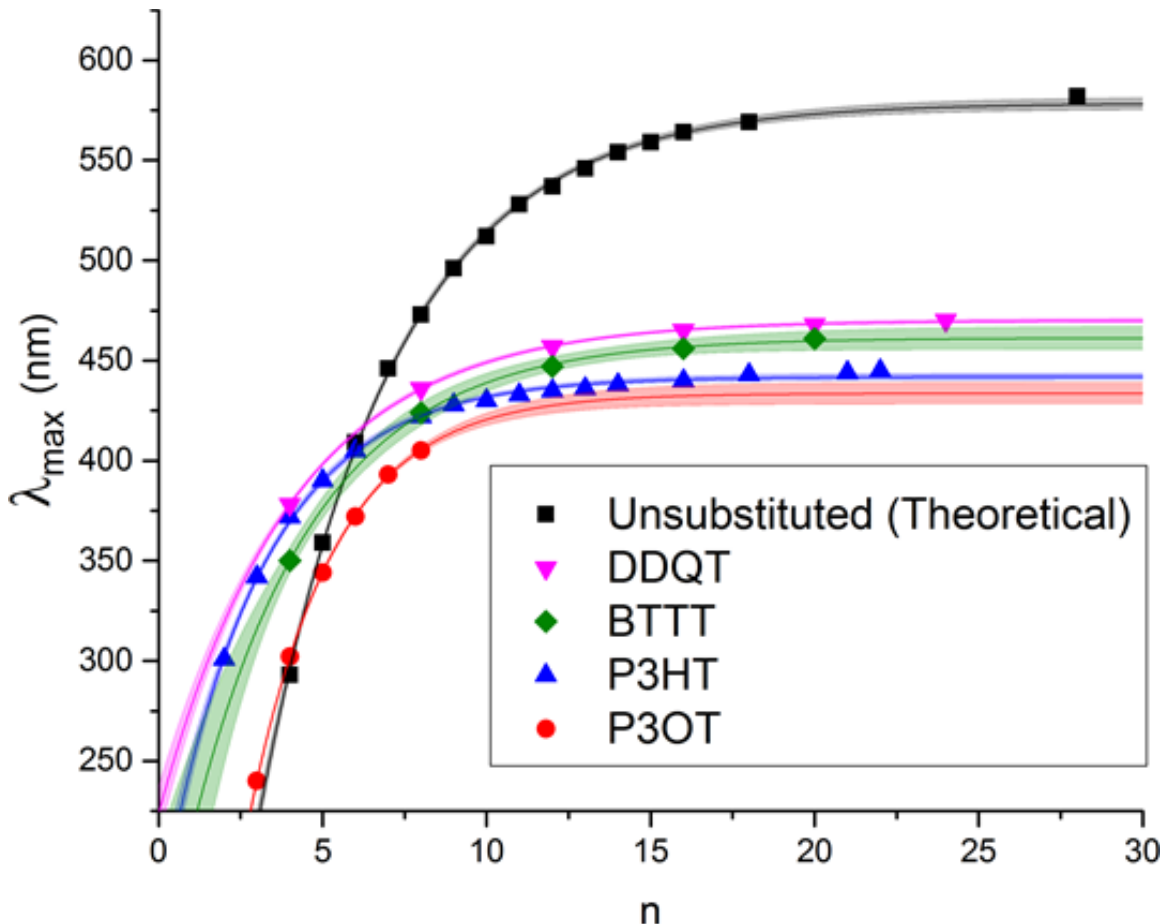


**Figure 2.17** Wavelength of maximum absorbance as a function of the number of thiophene repeat units for selected systems. The solid lines and shaded regions are fits and confidence intervals, respectively, of the exponential decay model to the data.

**Table 2.5** Effective conjugation lengths and wavelength of maximum absorbance for an infinite polymer for selected systems.

Oligomer	$n_{\text{ecl}}$	$\lambda_{\infty}$ (nm)
Unsubstituted (Theoretical) <sup>1</sup>	26.9	579
DDQT	22.4	470
BTTT	21.6	461
P3HT <sup>2</sup>	17.0	442
P3OT <sup>3</sup>	16.7	434

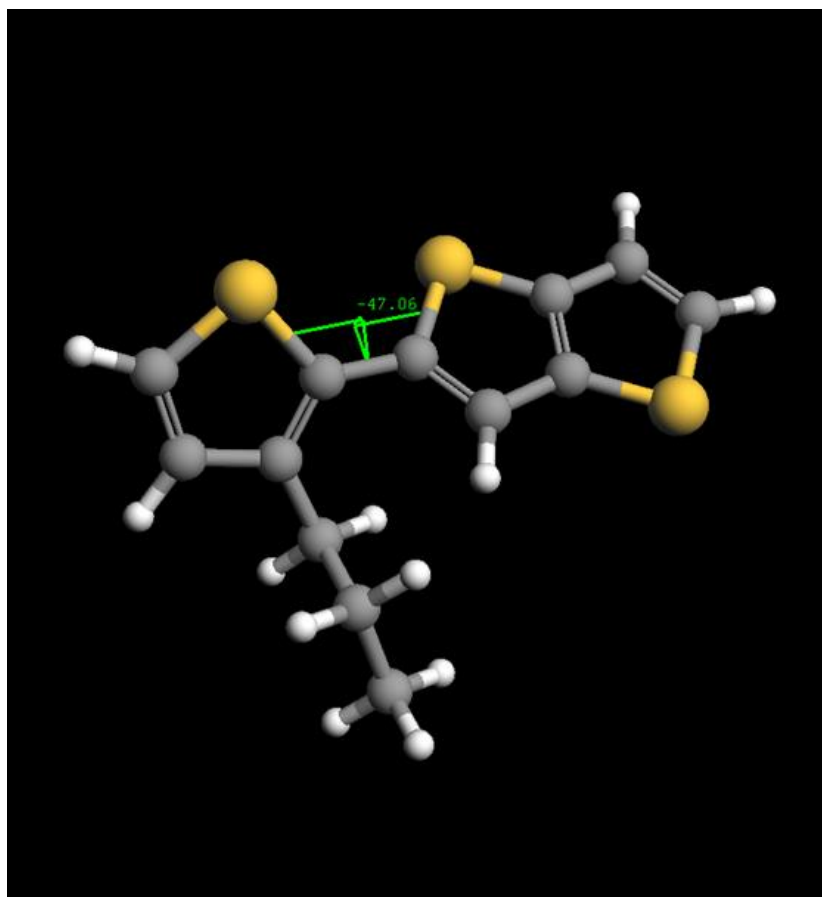


**Figure 2.18** Results from the quantum mechanical geometric optimization of alkylthiophene-thienothiophene dimer.

For comparison, a number of oligomeric systems reported in the literature were also compared to the evolution in optoelectronic properties of the synthesized oligomers. Bendikov and coworkers used density functional theory (DFT) quantum mechanical modeling at the B3LYP/6-31G(d) level, in conjunction with periodic boundary

conditions, to simulate the electronic structure of unsubstituted polythiophenes.<sup>65</sup> These simulations are necessary because unsubstituted polythiophenes are insoluble and therefore impossible to characterize via traditional solution-state spectroscopy. When analyzed using the effective conjugation length model described here, it was determined that the conjugation saturates at  $n = 26.9$ , substantially higher than DDQT or BTTT oligomers. Additionally, oligothiophenes bearing alkyl side chains on every thiophene unit have been reported in the literature. Heeney and coworkers reported a synthesis of pure poly(3-hexylthiophene) (P3HT) oligomers, and here, through this analysis, it was determined that the effective conjugation length is 17.0 repeat units.<sup>66</sup> This reveals that P3HT is significantly more twisted relative to quaterthiophene-based polymers which bear the same number of methylene side chain carbons per thiophene (24 carbons per 4 thiophene units). Additionally, the synthesis of oligothiophenes bearing longer octyl side chains was reported in the literature, and these longer alkyl chains reduced the effective conjugation length to 16.7 thiophene units because of the increased torsional forces.<sup>63</sup> These results demonstrate that oligo- and polythiophenes which bear fewer, longer solubilizing side chains remained more planar than those with greater, shorter side chains, increasing the absorption, and thus potentially performance in devices. Furthermore, the distribution of torsion afforded by individual thiophene units reduced the overall torsion of the system and increased the delocalization of orbital wavefunctions in comparison with fused systems. Finally, it should be emphasized that more twisted polymers with shorter effective conjugation lengths can be modeled with shorter oligomers, while longer oligomers are required to model more planar systems.

### **2.3.9 Summary**

This work characterized the evolution in crystalline, morphological, and optoelectronic properties for monodisperse, well-defined quaterthiophene oligomers of one to six repeat units in length. It was demonstrated that the crystallinity, particularly the presence of a liquid crystalline phase, becomes polymer-like for oligomers of at least 4 repeat units in length. It was shown that DDQT-2 is not an appropriate model for PQT-12 due to the herringbone packing of the oligomer. The effective conjugation length of PQT-12 was shown to be equivalent to the pentamer. Furthermore, the pentamer displayed crystalline, fibrillar nanostructures which may be excellent models for PQT-12 crystallites. As a whole, this work represents an approach for the characterization of oligomers to determine the shortest oligomer which may be used a representative model system for the polymer.

## CHAPTER 3

### DETERMINING THE SOLID-STATE INTERACTIONS BETWEEN OLIGOMER AND POLYMER

#### 3.1 Introduction

While organic photovoltaics and field-effect transistors have reached record efficiencies and mobilities, respectively, a complete, fundamental understanding of morphological control remains incomplete.<sup>19,67–70</sup> While the effects of solvents and coating methods have been extensively investigated, and the role of additives has been a continuing avenue of research, the role of one particular element present in virtually every polymerization is still not well understood: oligomers. These low molecular weight materials are at best neglected, at worst discarded, when synthesizing conjugated polymers for optoelectronic applications.<sup>31,36</sup> The “conventional wisdom” is that shorter polymer chains are simply impurities which may act as charge trapping sites, and while there have been some recent efforts to characterize pure oligomers, as discussed previously, the role of pure, well-defined oligomers in polymer thin films has not been thoroughly studied.<sup>10,52,71–73</sup>

The electronic performance of semiconducting organic films is heavily dependent on morphology, which can be broken down into two main components: crystallinity and connectivity.<sup>22</sup> Small molecule semiconductors typically exhibit high crystallinity, with films containing large crystalline grains; fast charge transport is expected within these grains.<sup>74,75</sup> However, the sharp grain boundaries between crystallites present large barriers to charge transport.<sup>28</sup> This relationship between crystallinity and charge transport

has been demonstrated by fabricating devices from single crystals, which exhibit exceptionally high mobilities, and from polycrystalline films of the same material in which charge transport is severely retarded.<sup>8,76</sup> High molecular weight films, in contrast, produce relatively smooth films with small polymer crystallites, yet retain high charge mobility due to the interconnected nature of the grains.<sup>22</sup> These “tie chains” which connect crystallites through the amorphous interfaces transport charge carriers along their backbones.<sup>77</sup>

Polythiophenes are prototypical semicrystalline polymer semiconductors and are among the best-studied organic semiconducting materials.<sup>22</sup> poly[2,5-bis(3-dodecylthiophen-2-yl)thieno[3,2-*b*]thiophene] (PBTTT) is one of the best-performing polythiophenes due to its relatively high crystallinity in thin films; numerous intermolecular interactions including  $\pi$ - $\pi$  stacking between the conjugated backbones and hydrophobic van der Waals interactions between the alkyl side chains.<sup>24,78</sup> Similar to DDQT oligomers, BTTT trimers pack similarly to the polymer in a lamellar configuration. In contrast, BTTT-1 packs in a two-dimensional fashion and BTTT-2 shows significant misorientation relative to the substrate according to grazing incidence X-ray diffraction studies. Additionally, BTTT-3 is still well within the “oligomer” regime, as it is below the effective conjugation length and thus the optoelectronic structure of the molecule is distinct from that of high molecular weight PBTTT. Thus, BTTT-3 is an excellent representative oligomer with which to study the interaction between oligomers and polymers.

The goal of this research is to determine how conjugated oligomers and polymers interact in the solid state by characterizing the morphological and electronic properties of



blended films. A particular focus is the relationship between crystallinity imparted by the oligomer, connectivity imparted by the polymer, and the resulting charge transport properties.

Previous studies have examined blending traditional aliphatic polymers with semiconducting polymers and small molecules to examine the phase behavior of blended films. Arias, *et al.*, characterized films consisting of PQT-12 blended with poly(methyl methacrylate) and discovered that vertical phase separation occurred, with PQT-12 lying closest to the surface-modified substrate.<sup>79</sup> In a separate study, Salleo and coworkers blended rubrene, a small molecule semiconductor, with polystyrene (PS) and poly(4-vinylpyridine) (P4VP).<sup>80</sup> Those researchers noted that the choice of non-conjugated binding polymer affected the resulting crystal structure of the rubrene crystallites present in the blended films. Additionally, phase separation was also observed. The research reported here is fundamentally different, as BTTT-3 and PBTTT were not expected to exhibit phase separation and, in fact, formed a continuous phase. As a corollary, strong intermolecular interactions between oligomer and polymer of the same type of material are generally expected and the effects of these interactions are reported.

## **3.2 Experimental**

### **3.2.1 Materials**

The oligomer BTTT-3 oligomer was synthesized *via* Stille coupling by Dr. Lei Zhang. The polymer PBTTT was synthesized by Thomas McCarthy-Ward *via* Stille coupling under microwave conditions as reported in the literature.<sup>78</sup> All solvents used were purchased from Fisher Scientific and were used without further purification. Silicon wafers were purchased from Addison Engineering.

### 3.2.2 Methods

Matrix-assisted laser desorption ionization time-of-flight (MALDI-TOF) mass spectrometry was performed using a Bruker Biflex III mass spectrometer with terthiophene as matrix. Samples were prepared by mixing equal volumes of 25 mg/mL terthiophene in chlorobenzene with 0.1 mg/mL sample in chlorobenzene and drop casting the mixed solution onto a polished steel target plate. Linear ion mode was used with a 25 kV accelerating voltage.

Gel permeation chromatography (GPC) was performed with an Agilent PL-GPC 220. Trichlorobenzene heated to 135 °C was the elution solvent and molecular weight was determined against polystyrene standards.

Atomic force microscopy (AFM) images were obtained using a Veeco Dimension 3100 AFM in tapping mode with a scan rate of 1 Hz. Samples were prepared by spin coating the materials from a 2 mg/mL chlorobenzene solution at 2000 rpm for 1 min onto silicon wafers with a 300 nm thermal oxide (SiO<sub>2</sub>) surface layer which were cleaned with detergent, deionized water, acetone, and isopropanol, then treated by UV-ozone for 10 minutes.

Grazing-incidence X-ray diffraction was performed by Edmund Kingsland Burnett at the Stanford Synchrotron Radiation Lightsource (SSRL). Samples were prepared by spin coating the materials from a 2 mg/mL chlorobenzene solution at 2000 rpm for 1 min onto silicon wafers which were cleaned with detergent, deionized water, acetone, and isopropanol, then treated by UV-ozone for 10 minutes.

Differential scanning calorimetry (DSC) measurements were taken using a TA Instruments Q1000 DSC with heating and cooling rates of 1 K min<sup>-1</sup> and 5 K min<sup>-1</sup> for

the BTTT-3 and PBTTT melting regions, respectively, to obtain clear endotherms under a flow of nitrogen. Approximately 5 mg of materials were deposited into an aluminum pan by drop casting from a chlorobenzene solution. The pans were hermetically sealed prior to heating.

Field-effect transistors were fabricated by spin coating the materials from a 2 mg/mL chlorobenzene solution at 2000 rpm for 1 min onto lithographically patterned silicon wafers with a 300 nm thermal oxide (SiO<sub>2</sub>) surface layer. Channel lengths were 125 μm and channel widths were 3000 μm. All electrical measurements were performed in ambient conditions using a standard probe station connected to a Keithley 4200-SCS Parameter Analyzer.

### **3.3 Results and Discussion**

#### **3.3.1 Characterization of oligomer and polymer purity and molecular weight**

A main focus of the study is to have a very well-defined system with which to evaluate the interactions between oligomer and polymer. If the polymer was to have a large low molecular weight component, it would be difficult to draw conclusions about the effects of added oligomer. Thus, the molecular weights of BTTT-3 and PBTTT were characterized by gel permeation chromatography (GPC). The oligomer, BTTT-3, was synthesized using a bottom-up approach *via* Stille coupling which resulted in a very well-defined structure. GPC is known to overestimate the molecular weight of short conjugated oligomers because it is typically calibrated with polystyrene (PS) standards. Polystyrene is a fairly flexible polymer while BTTT-3 is more rod-like, and thus the hydrodynamic volume of BTTT-3 is equivalent to that of a much longer PS chain. The molecular weight of BTTT-3 was measured to be 3337 Da due to this effect, however, a

narrow polydispersity index (PDI) of 1.01 was still observed. Therefore, the molecular weight of BTTT-3 was unambiguously characterized by matrix-assisted laser desorption ionization time-of-flight (MALDI-ToF) mass spectrometry, and the molecular weight was determined to be 1917 Da, which corresponds exactly to BTTT-3. The molecular weight of PBTTT was determined to be 24.9 kDa, equivalent to roughly 40 repeat units, with a PDI of 1.67. As demonstrated by the GPC traces, the PBTTT used for this study contained minimal low molecular weight oligomer (Figure 3.1).

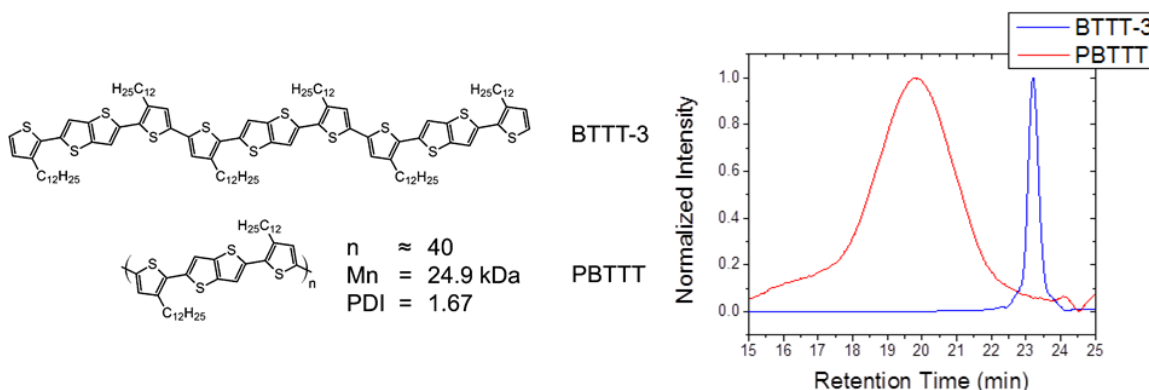


**Figure 3.1** Molecular structures of BTTT-3 and PBTTT (left), and gel permeation chromatography traces for BTTT-3 and PBTTT (right).

### 3.3.2 Characterization of the surface morphology of blended films

Film connectivity and homogeneity are essential for producing connected films which can facilitate transport charges. Atomic force microscopy (AFM) was performed to characterize the morphology of the blended films (Figure 3.2). “Films” of pure BTTT-3 spun coat onto SiO<sub>2</sub> consisted mainly of small 50-100 nm crystallites due to fast evaporation of the solvent, chloroform. The connectivity of these crystallites appeared to be minimal in evaluating the films via this method. However, films cast from a 1:5 blend of polymer to oligomer produced smooth films with a terraced surface structure. Additionally, the average surface roughness ( $R_q$ ) decreased from 34.0 Å to 9.3 Å. This

morphology has been previously observed for annealed pure PBTTT films, and is considered to exhibit very high molecular order, making it optimal for charge transport.<sup>33,81</sup> This terraced morphology has been attributed to the high degree of order for PBTTT films in which the side chains are interdigitated. The AFM data for the 1:5 blend is in good agreement with the previously reported work, with *ca.* 15 Å step heights for the terraces which correspond to one lamellar stack of PBTTT-C<sub>12</sub> in which *ca.* 6 methylene units are interdigitated.<sup>33</sup>

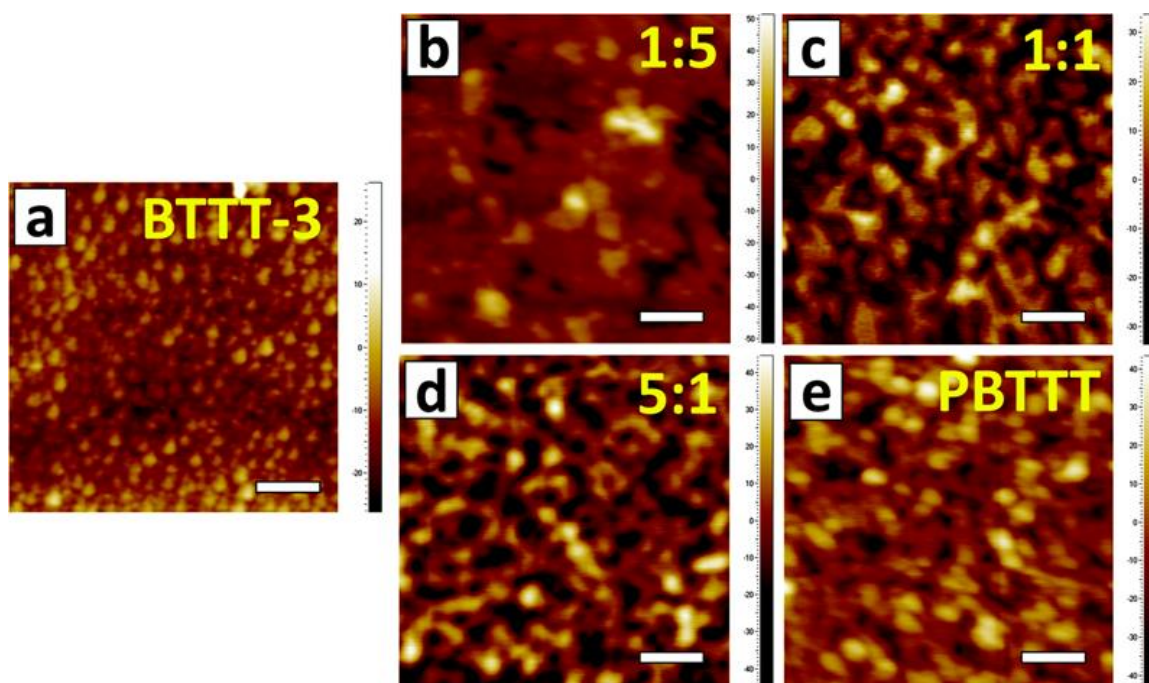


**Figure 3.2** Atomic force micrographs of films with various oligomer/polymer compositions..

In films which consisted of more polymer, a nodule-like structure was formed which is typical for unannealed conjugated polymer films. This morphology first appears in films consisting of 50% polymer, and increasing the amount of polymer present in the films did not significantly change the surface morphology. The surface roughness

increased slightly upon increasing the polymer concentration, with a maximum of 13.0 Å for the 5:1 polymer-to-oligomer films (Table 3.1).

**Table 3.1** Surface roughness of films with various oligomer/polymer compositions.

Film Composition (Polymer:Oligomer)	Roughness ( $R_q$ , Å)
BTTT-3	34.0
1:5	9.3
1:1	9.4
5:1	13.0
PBTTT	10.9

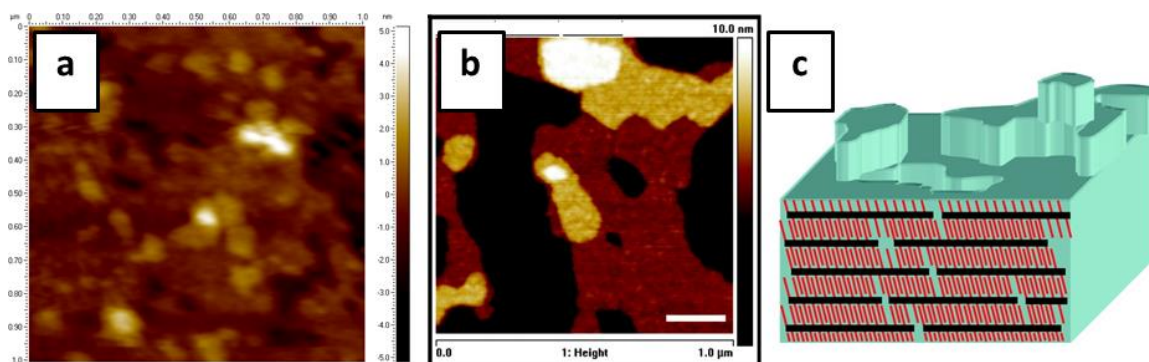


**Figure 3.3** Atomic force micrographs of a 1:5 (polymer:oligomer) film demonstrating terraced morphology (a), and the terraced morphology (b) and a schematic (c) for highly crystalline, annealed, high molecular weight film of PBTTT. The scales, both laterally and vertically, for both AFM scans are equivalent. (b) and (c) reprinted from DeLongchamp, D. M. *et al.* High Carrier Mobility Polythiophene Thin Films: Structure Determination by Experiment and Theory. *Adv. Mater.* **19**, 833–837 (2007).<sup>34</sup>

### 3.3.3 Analysis of molecular packing in blended films

The microstructure of the blended thin films was probed via grazing incidence X-ray scattering (GIXD) (Figure 3.4). This technique was used to evaluate the evolution in molecular packing for films which contained varying amounts of oligomer and polymer. Diffractograms of all of the films demonstrated that the molecules adopted an edge-on orientation, with  $Q_{xy}$  peaks appearing at *ca.*  $1.7 \text{ \AA}^{-1}$  which corresponds to the close  $\pi$ - $\pi$

stacking distance of *ca.* 3.7 Å. Single crystals of BTTT-3 were previously grown and characterized by X-ray scattering of these bulk crystals, however some disorder was observed, with layers slightly misoriented with respect to one another. However, the unit cell parameters were determined to be, approximately:  $a = 9.9 \text{ \AA}$ ,  $b = 12.4 \text{ \AA}$ ,  $c = 22.3 \text{ \AA}$ ,  $\alpha = 92^\circ$ ,  $\beta = 102^\circ$ ,  $\gamma = 101^\circ$ , with the volume of one molecule corresponding well with the unit cell volume. The BTTT-3 molecules in the thin film display some similarities with the bulk crystal packing but there are also some notable differences. The  $Q_z$  peaks observed in the diffractogram agree well with the  $c$  axis of the unit cell, which is the direction of side chain packing. This also supported the conclusion that the molecules pack with an edge-on orientation. However, the Bragg rods at  $Q_{xy} = 0.2 \text{ \AA}^{-1}$  did not correspond to the  $a$  or  $b$  unit cell parameters for the bulk crystal structure. Additionally, no other peaks which could correspond to  $a = 9.9 \text{ \AA}$  or  $b = 12.4 \text{ \AA}$  were observed, and thus the thin film phase of BTTT-3 was not equivalent to the bulk crystal phase. In their place, the Bragg rods at  $Q_{xy} = 0.2 \text{ \AA}^{-1}$ , which correspond to a real space length of *ca.* 3 nm, were attributed to fully extended BTTT-3 molecules, which are *ca.* 3 nm in length, packed end-to-end.

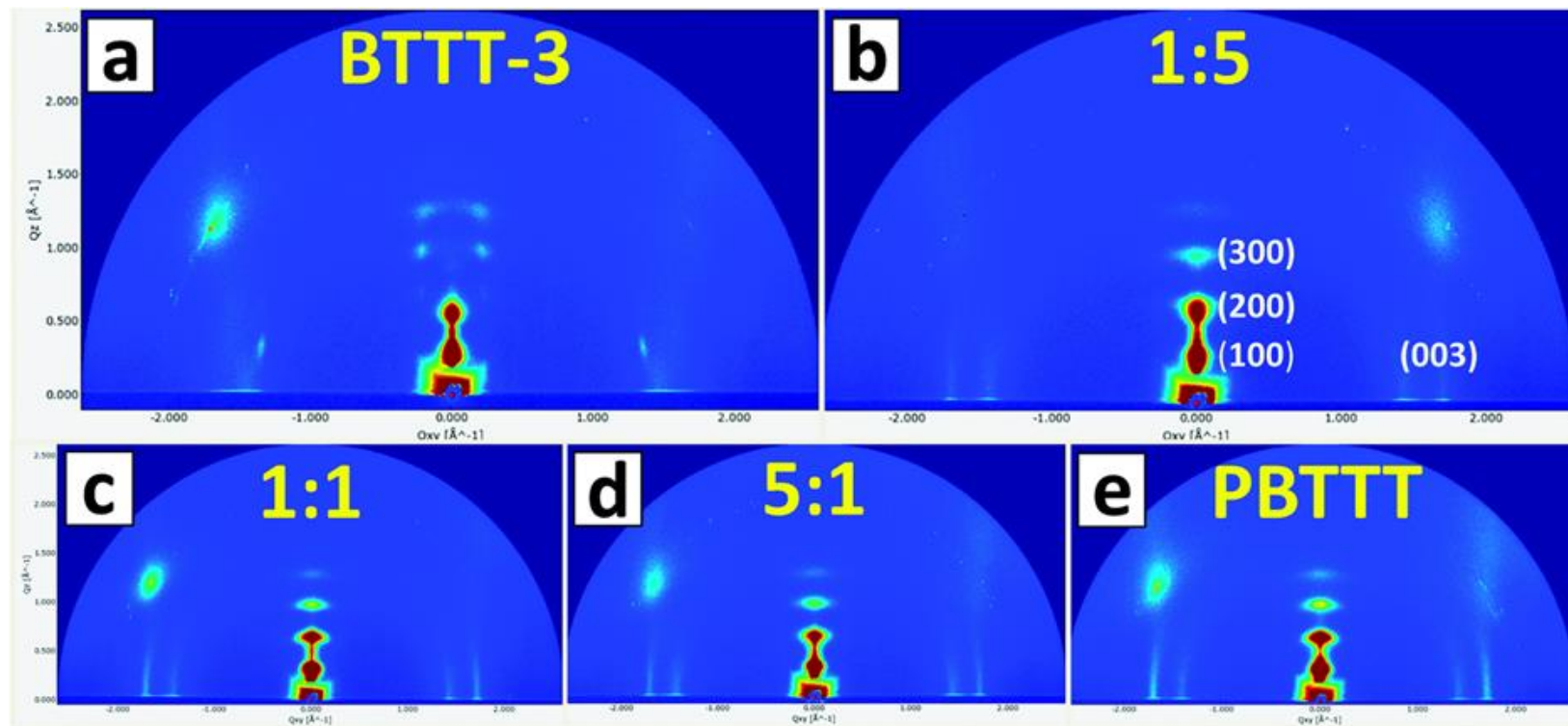


**Figure 3.4** Grazing incidence wide angle X-ray scattering diffractograms of films with various oligomer/polymer compositions.



Upon the addition of a nominal amount of polymer to the blend, the diffractogram changed dramatically, in good agreement with the change in morphology observed via AFM. The Bragg rods at  $Q_{xy} = 0.2 \text{ \AA}^{-1}$  were absent in the diffractogram of each blend which contained PBTTT, indicating that PBTTT was incorporated into BTTT-3 crystallites. Because BTTT-3 is fairly long in comparison to the monomer and other small molecules, and the intermolecular interactions with PBTTT are essentially the same of PBTTT with itself, there is no energetic driving force for phase separation, entropically or enthalpically. The polymer and oligomer chains form a fully mixed phase, as indicated by AFM, and the spatial coherence of the extended BTTT-3 chains is disrupted, quenching the in-plane  $Q_{xy} = 0.2 \text{ \AA}^{-1}$  peak. Furthermore, the oligomer and polymer interact strongly in this fully integrated phase; the  $\pi$ - $\pi$  stacking peak at  $Q_{xy}$  peaks =  $1.7 \text{ \AA}^{-1}$  remains present at all blend ratios (Figure 3.5).

Remarkably, with the disappearance of the Bragg rods of the BTTT-3 lattice, the diffractogram of the 1:5 polymer-to-oligomer blend closely mirrors that of the pure polymer film. The (100) peak and higher reflections (up to (300)), as well as the (003) reflection were readily indexed and are essentially the same for all films which contain a nominal amount of polymer. From this, it is concluded that the presence of PBTTT essentially guides the crystallization of BTTT-3 upon solidification into the film. The mechanism of solid-state morphology formation is in excellent agreement with the other data. As the polymer guides the oligomer crystallization, BTTT-3 crystallites connected with PBTTT were formed, producing a highly ordered material as demonstrated by the

terraced morphology observed in the AFM micrographs. This highly crystalline, connected film morphology is ideal for charge transport.

### BTTT-3



### BTTT-3 + PBTTT



**Figure 3.5** Cartoon of pure BTTT-3 crystallites and crystallites which have incorporated PBTTT into their structure.

#### 3.3.4 Characterization of crystallinity and thermal properties

To further characterize the solid-state interactions between oligomer and polymer, differential scanning calorimetry (DSC) was performed (Figure 3.6). Samples were prepared by mixing the materials in solution and drop casting them into the DSC pans which were then hermetically sealed. The data reported here was obtained during the second heating cycle to erase the thermal history of the casting/solidification method. In the sample which contained pure BTTT-3, two endotherms were observed due to the liquid crystalline nature of longer BTTT oligomers and polymers. The first melting peak at *ca.* 62 °C was attributed to the melting of the dodecyl side chains, producing a liquid crystalline phase, while the oligomer backbone melted at 95 °C.

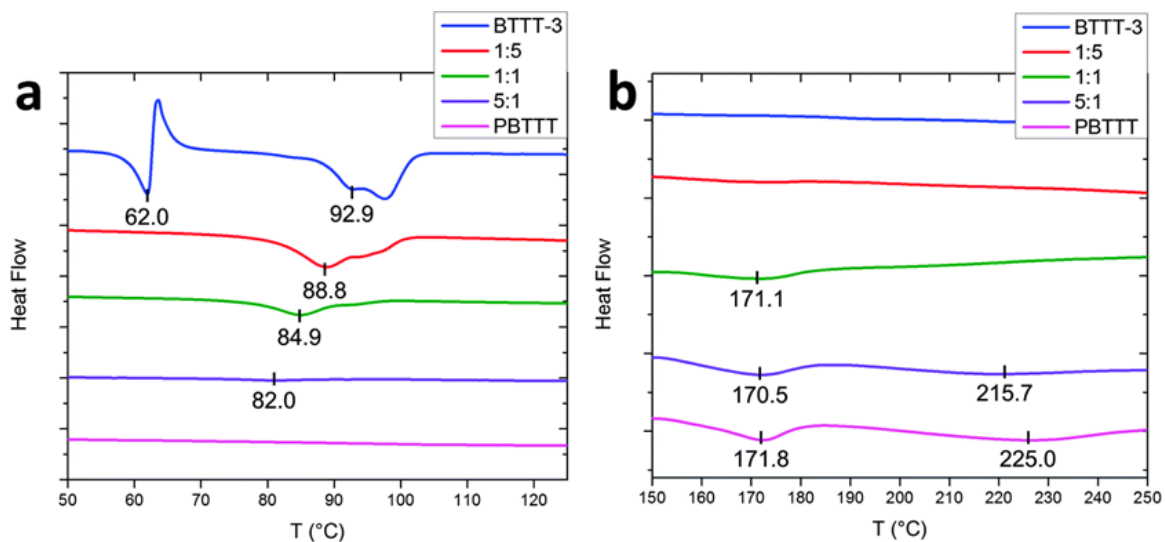


**Figure 3.6** Differential scanning calorimetry traces for the side chain and backbone melting regions of BTTT-3 (a) and PBTTT (b) (endo down).

Of particular note is the disappearance of the oligomer side chain melting peak for all samples which contained polymer. For these samples, a melting peak appeared at *ca.* 171 °C which is attributed to the side chain melting. Additionally, with the increase of the amount of polymer in the system, the BTTT-3 backbone melting endotherm was lowered in magnitude, as expected. The melting point of these crystallites was also depressed, indicating that the crystallites were decreasing in size and purity; this result demonstrates that the oligomers and polymers are, in fact, integrating at the molecular level. Furthermore, the PBTTT backbone melting endotherm, observed at 225 °C for the pure polymer, is also decreased in magnitude in blends which contain BTTT-3 and the melting point was substantially lowered. This result also strongly indicated that PBTTT and BTTT-3 were interacting at the molecular scale. Interestingly, the side chain melting point for blends which contained polymer remained relatively constant. This suggests that the side chains of the oligomer and polymer were fully intermixed and their enthalpic interaction were essentially the same as PBTTT-PBTTT side chain interactions.

However, the shorter nature of the BTTT-3 backbones and the associated free volume associated with the backbone chain ends allowed them to melt in the majority BTTT-3 crystallites.

### 3.3.5 Charge transport properties of blended films

Field-effect transistors (FETs) were fabricated using films consisting of BTTT-3 and PBTTT as the charge transporting layers. The charge transport response of these devices is depicted in Figure 3.7 and the mobilities, threshold voltages, and on/off current ratios are reported in Table 3.2. FETs in which BTTT-3 was the active layer exhibited low mobility,  $2.5 \pm 1.3 \times 10^{-4} \text{ cm}^2 \text{ V}^{-1} \text{ s}^{-1}$ , as expected from the poorly connected morphology; the enhanced crystallinity of these films was not sufficient for charges to be transported efficiently through the film. Remarkably, the addition of a small amount of polymer, with a 1:5 polymer-to-oligomer blend or higher polymer concentrations, drastically increases the charge transport properties of the thin film field-effect transistors. The films which were comprised of 83% oligomer exhibited mobilities of  $2.0 \pm 0.8 \times 10^{-1} \text{ cm}^2 \text{ V}^{-1} \text{ s}^{-1}$ , virtually identical to those of the high molecular weight polymer film. Additionally, the 1:1 blend of oligomers and polymers produced was used to produce devices that exhibited mobilities of  $2.8 \pm 0.2 \times 10^{-1} \text{ cm}^2 \text{ V}^{-1} \text{ s}^{-1}$ , marginally higher than that of the polymer and the highest mobilities recorded for all systems tested. The devices fabricated from a 5:1 blend of polymer-to-oligomer exhibited slightly lower mobilities,  $6.4 \pm 2.0 \times 10^{-2} \text{ cm}^2 \text{ V}^{-1} \text{ s}^{-1}$  than the other blends which contained both species. Interestingly, this is likely a similar ratio to what would be expected in the products of a normal polymerization, with a small amount of oligomer remaining with the majority product being polymer. The lower mobility exhibited by these blends may be due to the

presence of enough BTTT-3 in the system to passivate PBTTT crystals and limit the connectivity of the crystals, but not enough to significantly enhance the overall crystallinity of the film. The DSC data supported this conclusion, with an extremely small endotherm corresponding to BTTT-3 melting and the endotherms for PBTTT melting also being smaller than that of the pure PBTTT films. Additionally, the 5:1 films exhibited higher surface roughness than other films which contained PBTTT. In total, this indicated that a small amount of oligomer can actually lower the total crystallinity of a film while also disrupting charge transport due to the short, unconnected nature of the BTTT-3 chains. In contrast, higher loadings of oligomer increased the mobility due to the increased crystallinity of the systems. Additionally, these systems maintained a high degree of connectivity due to the presence of PBTTT which acted as tie-chains between crystallites. Furthermore, a comparison of the roughness as determined by AFM with the mobilities of the film reveals a good correlation between the smoothness of the film, which indicates blending and order of molecular species, with effective charge transport (Figure 3.8).

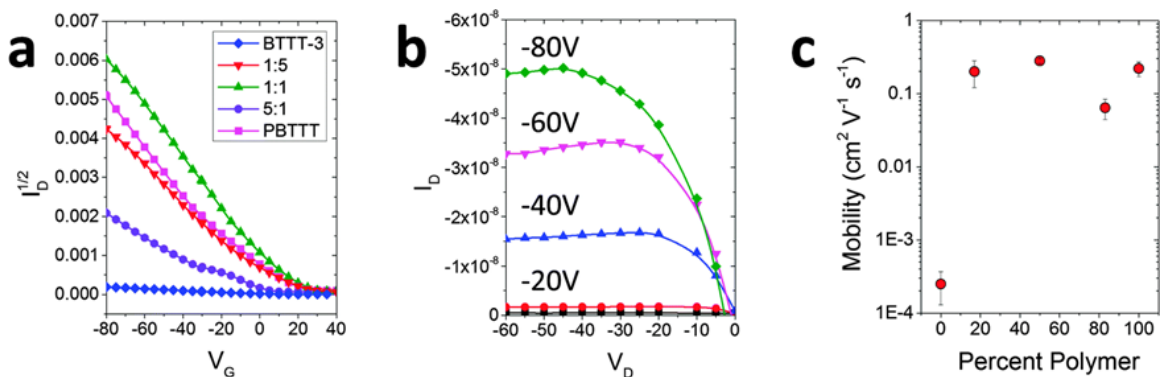


**Figure 3.7** Transfer curves ( $V_{SD} = -60$  V) (a) and a characteristic output curve (5:1 blend) (b) for transistors fabricated from films with various oligomer/polymer compositions, as well as a plot of hole mobility as a function of film composition.

**Table 3.2.** Mobilities, threshold voltages, and on/off current ratios for transistors fabricated from films with various oligomer/polymer compositions.

Sample	Mobility ( $\text{cm}^2 \text{V}^{-1} \text{s}^{-1}$ )	$V_{\text{Threshold}}$ (V)	$I_{\text{On/Off}}$
BTTT-3	$2.5 \pm 1.3 \times 10^{-4}$	$-2.9 \pm 10.9$	$10^3$
1:5	$2.0 \pm 0.8 \times 10^{-1}$	$5.4 \pm 10.3$	$10^3 - 10^4$
1:1	$2.8 \pm 0.2 \times 10^{-1}$	$10.8 \pm 4.8$	$10^3 - 10^4$
5:1	$6.4 \pm 2.0 \times 10^{-2}$	$5.7 \pm 9.9$	$10^3$
PBTTT	$2.2 \pm 0.5 \times 10^{-1}$	$0.8 \pm 1$	$10^3 - 10^4$

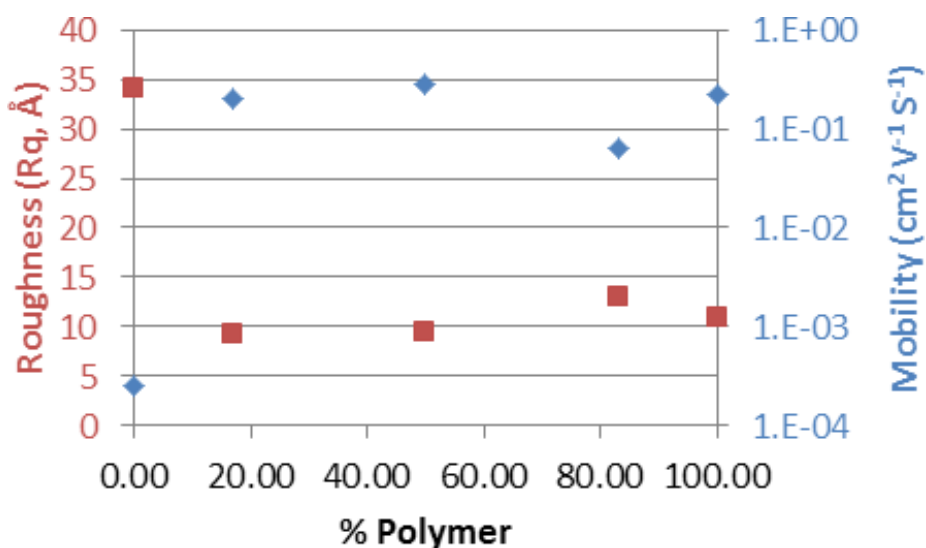


**Figure 3.8** Plot of the surface roughness and mobility values for films with various oligomer/polymer compositions.

These results represent a new approach for producing high-performance devices. By incorporating two species which strongly interact, particularly oligomer and polymer of the same monomeric structure, one can separate the effects of crystallinity from those of connectivity. Additionally, these data demonstrated that oligomers are not simply impurities or charge trapping sites, as evidenced by the high mobility for films which are comprised of 83% low molecular weight oligomer. A shorter species may be used to increase the overall crystallinity of the system, producing better order and thus higher charge mobility through the crystallites. In conjunction with the highly crystalline nature

of the system, a longer species which interacts strongly with, and is thus integrated into the crystallites of, the shorter species may be incorporated into the blend to increase the connectivity of the resulting film (Figure 3.9). This connectivity is essential for obtaining high charge carrier mobility over length scales longer than the dimensions of the crystallites.

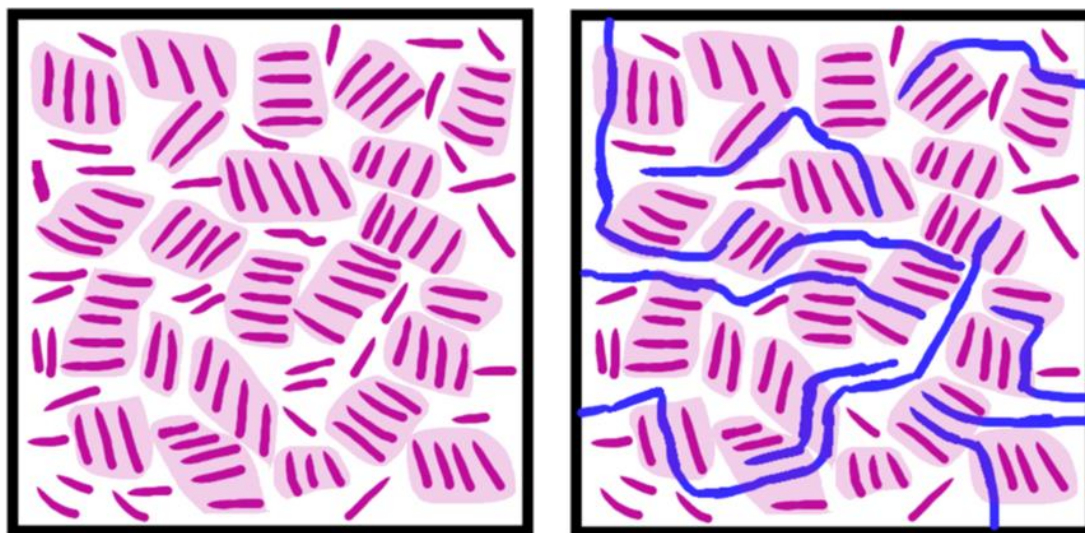


**Figure 3.9** Cartoon of the morphology of a pure BTTT-3 film (left), and a majority BTTT-3 film in which polymer has been incorporated, connecting the crystallites (right).

### 3.3.6 Summary

This work evaluated the molecular interactions between a representative oligomer, BTTT-3, and high molecular weight polymer, PBTTT. It was shown that these species were well-integrated at the molecular level. Furthermore, the connectivity between BTTT-3 crystallites imparted by a minimal amount of PBTTT was demonstrated to dramatically increase the charge transport properties of blended thin films. The morphology of these films was thoroughly characterized and correlated with the performance of field-effect transistors based on these blends. This study serves as a counterexample to the common notion that oligomers act as charge-trapping sites in

polymer films. Furthermore, the results suggest that it may be beneficially to selectively increase the oligomer content of polymer-based electronic devices to increase the crystallinity of the charge-transporting layers.



## **CHAPTER 4**

### **FRACTIONATION AND CRYSTALLIZATION OF OLIGOMERS IN SUPERCRITICAL FLUID**

#### **4.1 Introduction**

##### **4.1.1 Processing and Crystallization Techniques**

The process of crystallization is centered on the kinetics and thermodynamics of precipitation. Molecules associate with one another, forming a solid from a liquid, vapor, or solution phase. When the enthalpic benefits of molecular interactions in the solid state outweigh the entropic gains of the molecules remaining independent, such as when temperature is decreased, precipitation is favorable. While the maximization of positive enthalpic interactions is produced by forming crystalline structures, the kinetics by which this process occurs controls the rate of solidification and the final energy minimum of the transition. The rate of crystal growth, as well as final crystallinity, are determined by such factors as supersaturation, rate of mass transport to the crystal, and number of nucleating sites.<sup>82-84</sup>

##### **4.1.2 Crystallization from solution**

Organic semiconductors are subject to solution deposition methods such as spin coating and shear coating which are relatively fast techniques which greatly accelerate the formation of solid films. These thin films are typically semicrystalline, as the interaction between large pi surface areas of conjugated materials are quite strong and sufficient to impart crystallinity, however the kinetics are too rapid and the number of nucleation sites is too high to approach complete crystallization of a film, i.e. the

formation of a single crystal. Post-processing techniques have been used to improve the crystallinity of solid films, including thermal and solvent vapor annealing, by allowing further mobility of the molecules so that they may rearrange themselves and lower the overall energy of the system. These methods result in films with better charge carrier mobilities by producing more crystalline films which contain better registration between neighboring molecules as well as a decrease in trap states.

The relationship between concentration and solubility (i.e. the supersaturation) must be well controlled to generate large crystals from solution. Concentration may be controlled by either reducing the amount of solvent present or increasing the amount of solute in the system, while solubility may be controlled by modulating the solvent quality. A classic crystallization technique is slowly cooling a saturated solution of material. As the temperature of the solution decreases, the solvent quality, and thus solubility, decreases concurrently, producing a supersaturated state; the lowering the temperature reduces in the entropic component of the free energy of the system. As this occurs, the free energy gain from the enthalpy of crystallization drives the solute towards precipitation and, if kinetics allow, the material will crystallize. Similarly, supersaturation may be induced by removing solvent through evaporation and crystallization proceeds similarly. By controlling the amount of solvent present in the ambient environment, such as through using a chamber saturated with solvent vapor, the evaporation rate, and thus precipitation rate, may be controlled.<sup>55,85</sup>

Crystallization from solution is ubiquitous for the crystallization of soluble small molecules, including organic semiconductors. Tetraazapentacene functionalized with (triisopropylsilyl)ethynyl groups (TIPS-TAP) has been drop-cast from solution to form

large crystals ( $>100\ \mu\text{m}$ ) upon solvent evaporation. By using two different solvent systems with different solvating powers but similar evaporation rates, the researchers demonstrated the dependence of crystallization on the kinetics of precipitation. For the solvent system in which TIPS-TAP was highly soluble ( $\sim 15\ \text{mg/mL}$ ), a large mass of material rapidly precipitated upon the evaporation of the solvent. However, for the solvent system with lower TIPS-TAP solubility ( $\sim 1\ \text{mg/mL}$ ), precipitation proceeded more gradually and the kinetics of TIPS-TAP crystallization allowed the crystals to form.<sup>86</sup>

While solution crystallization has been very successful for small molecules, polymer semiconductors are difficult to crystallize due to the large entropic penalty of ordering long, flexible molecules. This has severely limited the number of techniques available for the crystallization of conjugated polymers. One specialized method was developed by Reiter, *et al.*, to crystallize poly(3-hexylthiophene) (P3HT) from solution.<sup>87</sup> Unfortunately, it is difficult to extend this technique to other conjugated polymers because it is reliant on using the liquid monomer as a solvent; the system is very expensive and simply cannot be used for polymers which have solid monomers, and is thus relatively unattractive as a routine method.

#### **4.1.3 Crystallization from vapor**

Crystallization from vapor using the physical vapor transport method (PVT) is a common method for purifying and crystallizing small molecule semiconductors.<sup>88</sup> In this technique, a horizontal quartz tube is subjected to a heating gradient and the crude material to be crystallized is placed in the hottest zone (Figure 4.1). The temperature for the zone is chosen so that the material sublimates and is then transported through the tube

either by an inert carrier gas, such as nitrogen or argon, or diffusion if the system is placed under vacuum. Once the vapor-phase material reaches a cooler zone, it resolidifies; because there exists a temperature gradient, heavier impurities may be deposited in a relatively hot area, the target material will solidify in a slightly cooler area, and lighter impurities are transferred further to a still cooler area (or exhausted out of the system). If the conditions, particularly the temperature gradient and gas flow rate, are carefully tuned, the desired material may be transported slowly enough so that crystallization may occur as the semiconductor is being deposited. Unfortunately, this method is not applicable to polymeric materials, as they exhibit negligible vapor pressure; they will simply melt and degrade instead of subliming.

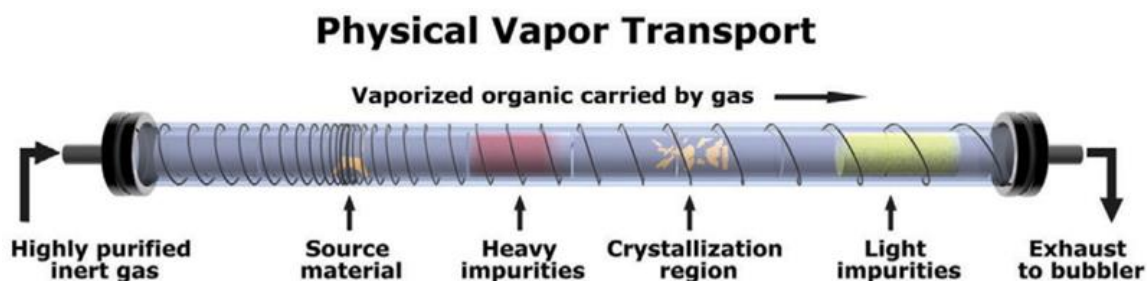


**Figure 4.1** Cartoon of crystallization using the physical vapor transport recrystallization method. Reprinted from Reese, C. & Bao, Z. Organic single-crystal field-effect transistors. *Mater. Today* **10**, 20–27 (2007).<sup>89</sup>

Large, centimeter-scale crystals of a benchmark small molecule semiconductor, rubrene (5,6,11,12-tetraphenyltetracene), are routinely formed via this method in our lab and others.<sup>90</sup> The crystals produced via this method are of sufficient quality, both in size and purity, for the intrinsic properties of rubrene to be characterized. Because of this crystalline perfection, a landmark study demonstrating the Hall effect in organic semiconductors was able to be conducted by Podzorov, *et al.*<sup>91</sup> Furthermore, the large transfer integrals present, combined with the virtual absence of charge-trapping defects,

allowed for the fabrication of transistors with mobilities of up to  $30 \text{ cm}^2 \text{ V}^{-1} \text{ s}^{-1}$ .<sup>92</sup> The availability of single crystals was an absolute necessity for these studies, among others, as variations in morphology would obfuscate the intrinsic properties of the materials.

#### **4.1.4 Properties of supercritical fluids**

By increasing the pressure and temperature of a solvent which is a liquid or gas at ambient conditions past the respective critical pressure and temperature of the material, it becomes a supercritical fluid. The literature is rich with examples of the modification of solvation properties by modulating the pressure and/or temperature of a solvent under supercritical conditions.<sup>93-97</sup> In particular, a distinct rise in solubility is often observed near the critical pressure of gases, as the density increases rapidly; this increased density greatly enhances the solvent-solute intermolecular interactions (Figure 4.2). Furthermore, the properties of supercritical fluids lie between those of liquids and gases, providing liquid-like solvation power with the diffusive behavior of a gas. The tunable nature of supercritical fluids with respect to solubilizing power makes them especially attractive for separation processes and, as described here, developing controlled conditions for the recrystallization of organic materials.

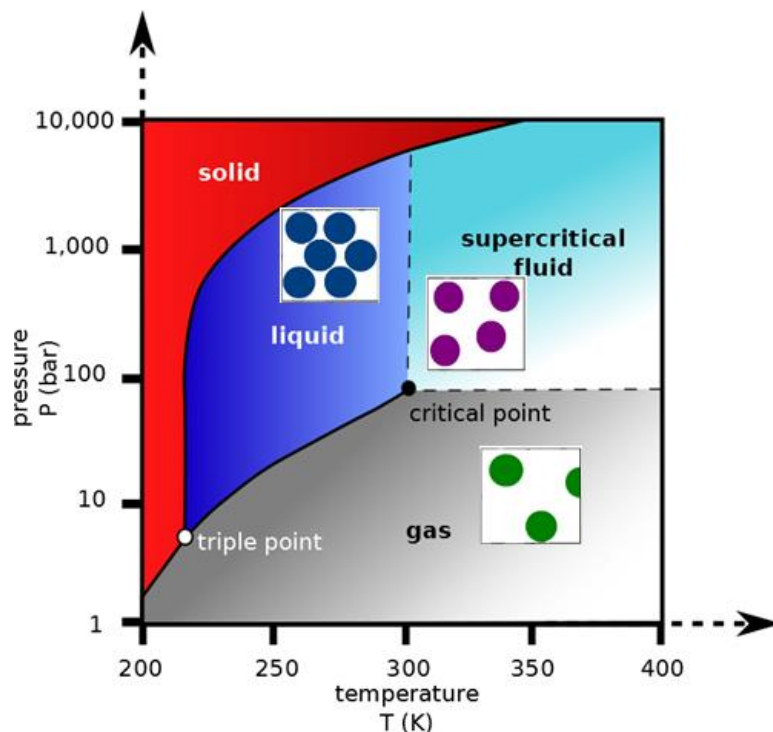


**Figure 4.2.** Phase diagram for carbon dioxide, illustrating the conditions for the supercritical phase. Reprinted from the UCDavis webpage.<sup>98</sup>

## 4.2 Experimental

### 4.2.1 Materials

The polymer PBTTT-C12 was purchased from Luminescence Technology Corp. It was characterized using gel permeation chromatography (GPC) with an Agilent PL-GPC 220. Trichlorobenzene heated to 135 °C was the elution solvent and molecular weight was determined against polystyrene standards. The number-average molecular weight was determined to be 20.3 kDa with a polydispersity index (PDI) of 3.60. All solvents used were purchased from Fisher Scientific and were used without further purification. For the synthesis of BTTT1.5, 5,5'-dibromo-4,4'-didodecyl-2,2'-bithiophene was purchased from BioFine International and all other reagents used were purchased from Sigma-Aldrich Co. Scintillation grade naphthalene was purchased from Acros

Organics. Rubrene was purchased from Sigma-Aldrich Co. All materials were used without further purification unless otherwise specified.

All stainless steel pressure equipment used was purchased from High Pressure Equipment Company. Rope heaters and thermocouples were purchased from OMEGA Engineering Inc. Aluminum foil was purchased from Fisher Scientific. Carbon dioxide, “bone dry” grade, was purchased from Airgas, Inc.

#### **4.2.2 Methods**

Optical micrographs were obtained with an Amscope MU1000 10 megapixel digital camera attached to a Zeiss Axio Scope.A1 microscope.

X-ray diffraction (XRD) data were obtained using a Panalytical X-Pert X-Ray Powder Diffractometer. Cu-K $\alpha$  X-ray radiation, wavelength = 1.54 Å, was generated from a Cu anode at 45 kV and 40 mA. A 0.5 degree Soller slit and Ni filter, to block K $\beta$  radiation, were used on the incident beam to improve resolution and accuracy. The diffractometer was calibrated with a single-crystal Si wafer. The Gonio scans proceeded with a step size of 0.02 degrees over a 2 $\theta$  range of 5-60°.

Matrix-assisted laser desorption ionization time-of-flight (MALDI-TOF) mass spectrometry was performed using a Bruker MicroFlex mass spectrometer in linear ion mode. No matrix was used due to the high absorbance and low molecular weight of the materials under study.

Fourier transform infrared spectroscopy data was obtained with a PerkinElmer Frontier FT-NIR/MIR Spectrometer in the attenuated total reflectance configuration.

Scanning electron micrographs (SEM) were obtained with an FEI Magellan 400 XHR-SEM. The images were analyzed using ImageJ.

A JEOL JEM-2000FX transmission electron microscope (TEM) operating with an accelerating voltage of 200 kV was used for TEM imaging and selected-area electron diffraction (SAED).

## **4.3 Results and Discussion**

### **4.3.1 Crystallization of small molecules in supercritical carbon dioxide**

Supercritical fluids were used as a transport medium for the crystallization of conjugated organic materials. One of the most commonly used supercritical fluids is supercritical carbon dioxide (scCO<sub>2</sub>). Carbon dioxide, being nontoxic and nonflammable, is considered a “green,” environmentally friendly solvent that can be used in place of halogenated solvents in many situations. Additionally, it is naturally abundant, as it exists in high-purity reservoirs, is a common byproduct of many industrial syntheses, including ammonia, hydrogen, and ethanol, and is, of course, a common product of fossil fuel combustion.<sup>99</sup> From a process perspective, scCO<sub>2</sub> is a very attractive medium because the critical point (critical temperature,  $T_c$ , is 31.1 °C and critical pressure,  $P_c$ , is 1070 PSI), which are easily accessible conditions through the use of steel high-pressure reactors. Furthermore, CO<sub>2</sub> is a gas at room temperature and thus is easily removed from the system at the end of the process.

Because of these attractive solvent properties, a system for the recrystallization of organic materials in supercritical CO<sub>2</sub> was developed. In the initial configuration, the semicrystalline organic material was loaded into the bottom of a 110 mL cylindrical steel pressure reactor (length: 47.0 cm, internal diameter: 1.67 cm) which was subsequently charged with CO<sub>2</sub> (Figure 4.3). The lower portion of the pressure vessel was then heated with a thermocouple-regulated rope heater and the full vessel was pressurized through the



use of a syringe pump filled with CO<sub>2</sub>. The upper portion of the steel reactor was exposed to the ambient air, producing a zone which was significantly cooler than the lower heated area. This geometry was designed to produce refluxing conditions, with the lower, hot solvent exhibiting a lower density than the upper, cold solvent which had a higher density (Figure 4.4). The reflux geometry reported here is similar to that used by Laudise, *et al.*, for the crystallization of quartz under hydrothermal conditions (Figure 4.5).<sup>100</sup> However, a notable different between the system described here and the one used by Laudise for generating quartz crystals is that the quartz crystallization was seeded by previously formed crystal sheets, while the crystallization of reported here occurred by a self-seeded process.



**Figure 4.3** Image of the 110 mL pressure reactor in the reflux geometry.

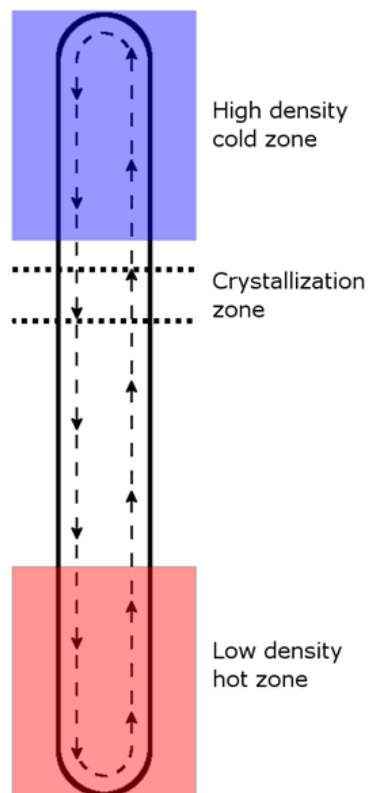


**Figure 4.4** Schematic of solvent flow inside the reactor in the reflux geometry.

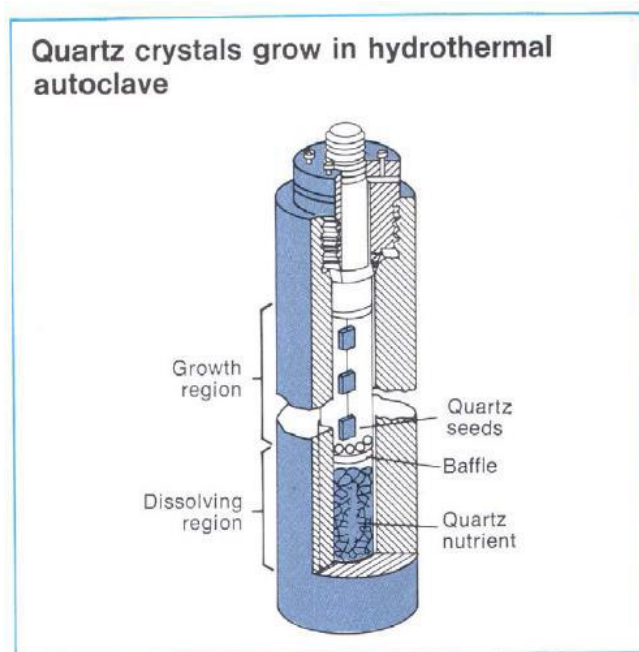


**Figure 4.5** Schematic of the reactor used by Laudise, *et al.*, for the crystallization of quartz in supercritical (hydrothermal) water. Reprinted from Laudise, R. A. Hydrothermal Synthesis of Crystals. *Chem. Eng. News* **65**, 30–43 (1987).<sup>100</sup>

One of the most well-known applications of supercritical CO<sub>2</sub> is the extraction of caffeine from coffee. Because the solubility parameters of caffeine in scCO<sub>2</sub> are well-understood, the appropriate conditions for caffeine recrystallization were determined and used for initial experiments. 200mg of caffeine was added to bottom of the 110 mL cylinder, and the lower zone of the reactor was heated to 175 °C, while the upper zone, exposed to the ambient environment, was measured to be 75 °C. The reactor was then pressurized to 2200 PSI. This produced a strong solubility gradient, with the caffeine being *ca.* 8 times more soluble in the hot zone dissolution zone than in the cold precipitation/recrystallization zone (Figure 4.6).<sup>101</sup> The solution was refluxed in this geometry for 16 hours, cooled, and then the CO<sub>2</sub> was vented to the atmosphere. Macroscopic single crystals of caffeine, with lengths up to several millimeters, were obtained (Figure 4.7).

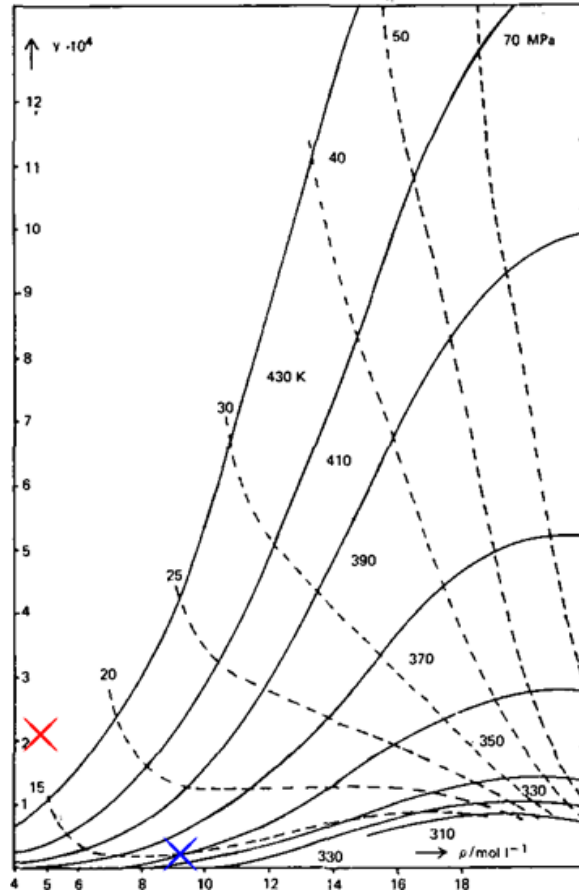


**Figure 4.6** Solubility data for caffeine in carbon dioxide (reprinted from Lentz, H., Gehrig, M. & Schulmeyer, J. Dynamic solubility measurements of caffeine in carbon dioxide and in carbon dioxide saturated with water. *Phys. B+C* **139-140**, 70–72 (1986).<sup>101</sup> The conditions present in the hot and cold regions of the reactor are denoted by red and blue Xs, respectively.

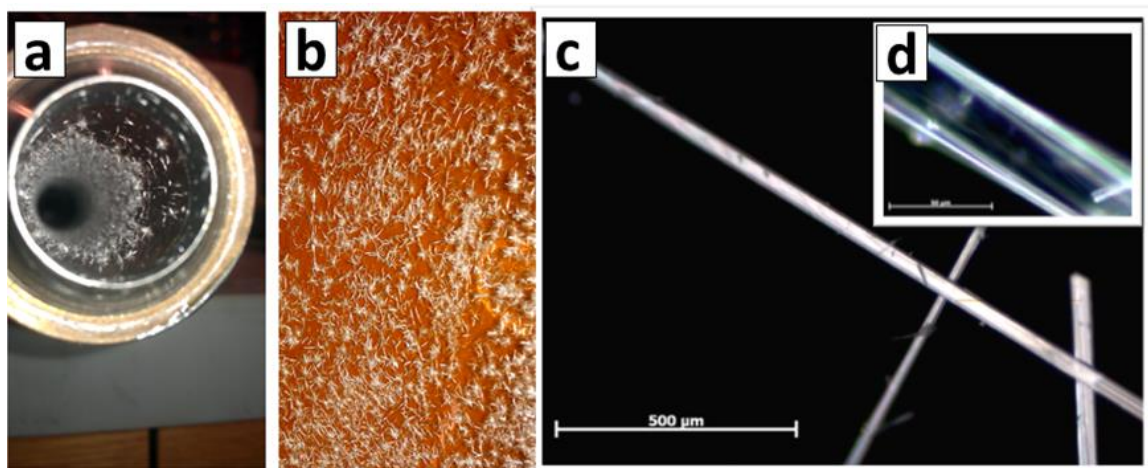


**Figure 4.7** Images of caffeine crystals grown on the polyimide-lined walls of the reactor (A), on the polyimide film removed from the reactor (B), and optical micrographs of the crystals demonstrating their size and purity (C, D).

Linear acenes are among the best-studied small molecule semiconductors, with their fused aromatic ring structure imparting high degrees of delocalization. A simple model for this class of materials is naphthalene, which is known to be soluble in supercritical  $\text{CO}_2$ . For this recrystallization, 200 mg of scintillation grade naphthalene was loaded into a porous aluminum foil boat which was placed in the lower zone of the vertical cylinder and the reactor was then charged with  $\text{CO}_2$ . This lower area was heated to 60 °C at 3000 PSI, producing a density of 0.196 g/mL, while the upper zone remained at 30 °C, resulting in a solvent density of 0.219. Under these conditions, the semicrystalline source naphthalene was dissolved in the lower hot region and was then transported upward by the solvent flux. As the solution cooled in the upper region, the naphthalene precipitated out of the solution and fell back down to the lower hot zone where the amorphous material could quickly dissolve while the crystalline region remained in the solid state due to the strong intermolecular interactions and long-range order. This cycle repeated throughout the crystallization, producing large, millimeter-

scale naphthalene crystals which were hexagonal in shape (Figure 4.8). This crystal habit was in good agreement with the crystal structure and Bravais, Friedel, Donnay and Harker (BFDH) crystal morphology.

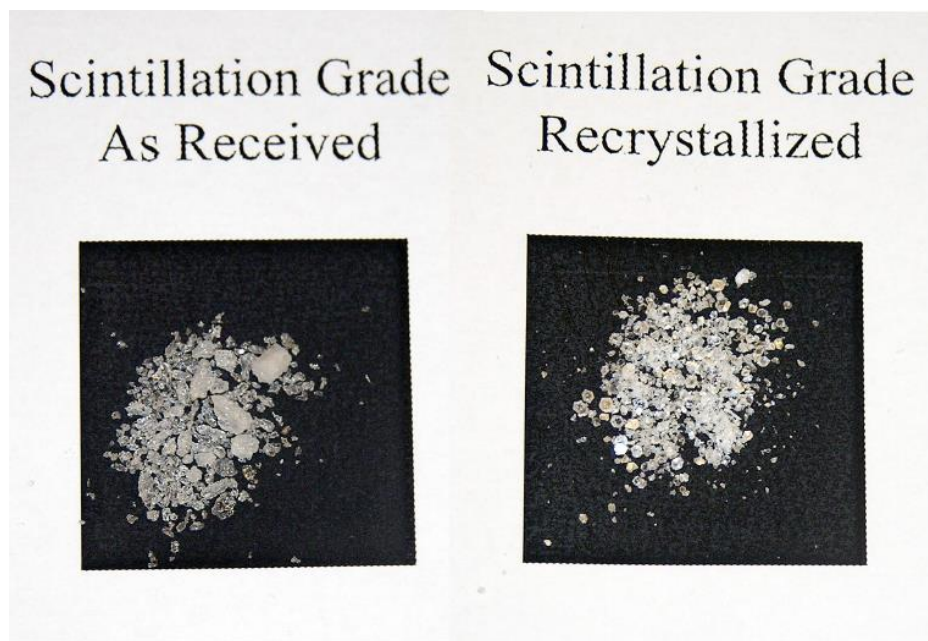


**Figure 4.8** Images of the polycrystalline source naphthalene and the material recrystallized in supercritical CO<sub>2</sub>.

To characterize the long-range order of these crystals, X-ray diffraction (XRD) was performed, with the large, plate-like crystals lying flat on the sample stage. The observed reflections were in excellent agreement with the d-spacing, 8.54 Å, in the (001) direction of the unit cell, and the multiple higher-order reflection peaks indicated excellent long-range order (Figure 4.9).

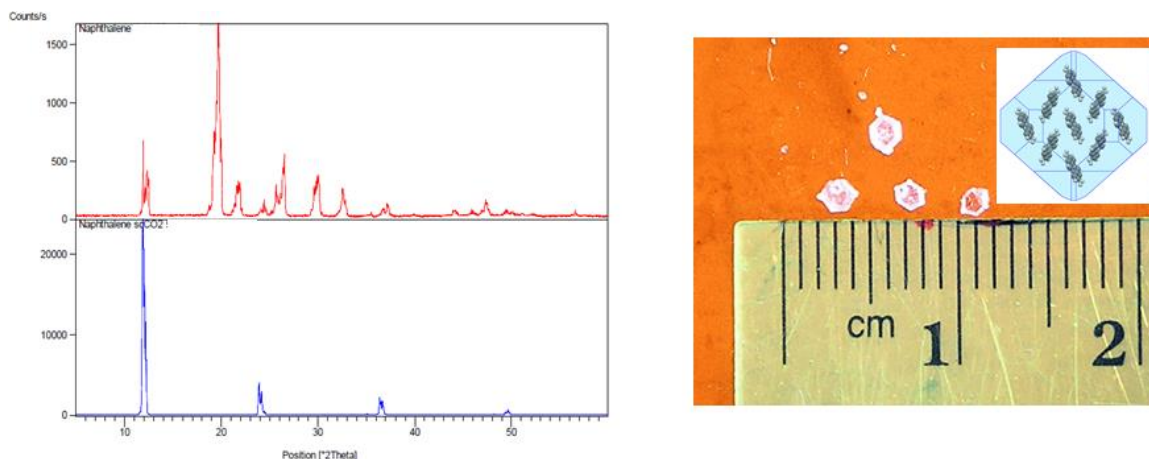


**Figure 4.9** X-ray diffraction data for naphthalene crystals (left) and images of the crystals and inset of BFDH crystal habit (right).

#### 4.3.2 Crystallization of rubrene in supercritical hexane

Unfortunately, the longer acenes which display significantly higher delocalization, as well as oligo- and polythiophenes have very limited solubility in scCO<sub>2</sub>. However, these materials were suspected to be soluble in supercritical hexanes (scHex), and thus the solvent system for recrystallization was switched to this more powerful solvent. Although the reaching the supercritical point of hexane ( $T_c = 234.5\text{ }^\circ\text{C}$ ,  $P_c = 438\text{ PSI}$ ) requires significantly higher temperatures than scCO<sub>2</sub>, the range of conditions was accessible via standard rope heaters. Additionally, the solubilities of these conjugated materials in supercritical fluid were expected to increase dramatically near their melting points which were generally above 200 °C. Additionally, the materials studied herein display sparing solubility in boiling hexanes at atmospheric pressure, which is ideal for crystallization using this method. The cold crystallization zones of these reactors are 35 °C ~ 90 °C, and therefore the limited solubility will cause the materials to crystallize in these regions while being dissolved in the hotter regions.

Rubrene is a benchmark small molecule organic semiconductor which exhibits very high hole mobilities, greater than  $10 \text{ cm}^2 \text{ V}^{-1} \text{ s}^{-1}$ , in the single crystal state.<sup>102</sup> This molecule is typically purified and crystallized via physical vapor transport (PVT), to produce the crystals for charge transport measurements. Solution-phase crystallization of rubrene has been somewhat limited, as many solvent systems and processing techniques generate crystals with molecular packings which are not ideal for charge transport, *i.e.* polymorphs.<sup>103,104</sup> In particular, the triclinic form of rubrene is often generated when crystallizing from solution, and the ideal orthorhombic crystals have never been generated during crystallization from hexane.

In order to make the supercritical crystallization reactor more similar to PVT in terms of molecular transport, an alternative geometry was constructed. In this configuration, the upper zone was heated while the lower zone was cooled and the semicrystalline source material, inside a porous aluminum foil boat, was placed in the hot upper zone (Figure 4.10). This setup resulted in diffusive transport throughout the reactor; in the reflux geometry, solvent flux transported the material to be crystallized up and down the reactor as the solvent was heated and cooled. The diffusive transport geometry leveraged the wide range of accessible solvent densities in the supercritical state to create a strong, stable temperature gradient. For hexane, the hot zone at  $275 \text{ }^\circ\text{C}$  was calculated to have a density of  $0.261 \text{ g/mL}$  at  $750 \text{ PSI}$ , while the cold zone of  $60 \text{ }^\circ\text{C}$  was calculated to have a density of  $0.629 \text{ g/mL}$  at the same pressure, an increase of  $141\%$ . Moreover, the density over this range of conditions is continuous; there is no abrupt change in density as the phase changes from supercritical to liquid as the hexane cools. This large density gradient minimized solvent flow, establishing a well-defined



temperature gradient. For comparison, the density of boiling hexane (68.7 °C) is 0.613 g/mL while room temperature (20 °C) hexane has a density of 0.659 g/mL, an increase of 7.5%, at atmospheric pressure. Even extending the cooling to -95 °C increases the density to only 0.762 g/mL, a 24% increase over the density at boiling. Thus, the strong density gradient accessible via the supercritical state is extremely beneficial for establishing a temperature gradient (Figure 4.11).

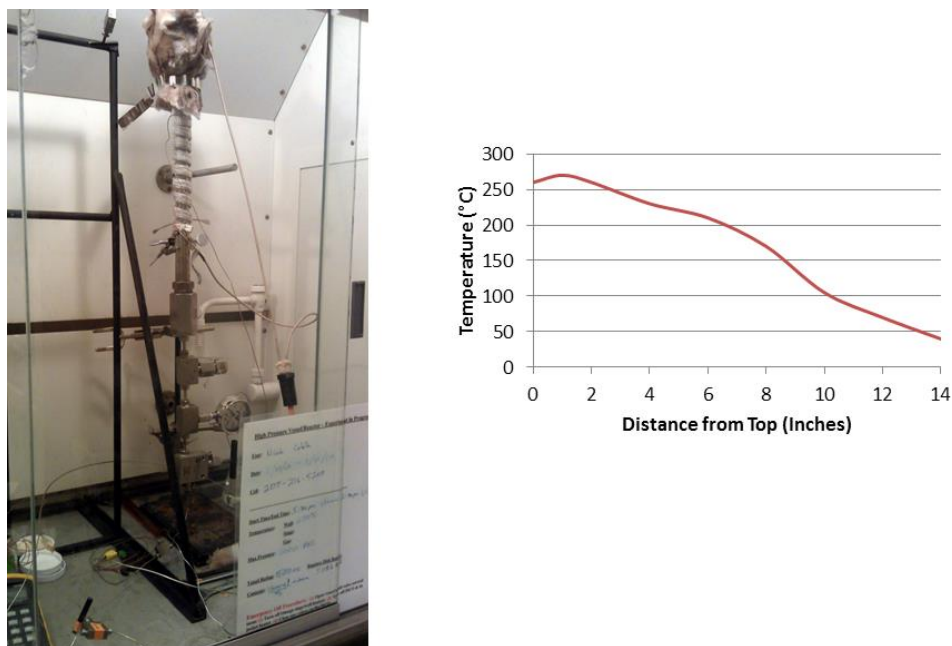


**Figure 4.10** Image of the 110 mL reactor in the diffusive geometry (left) and temperature profile for the reactor during operation (right).

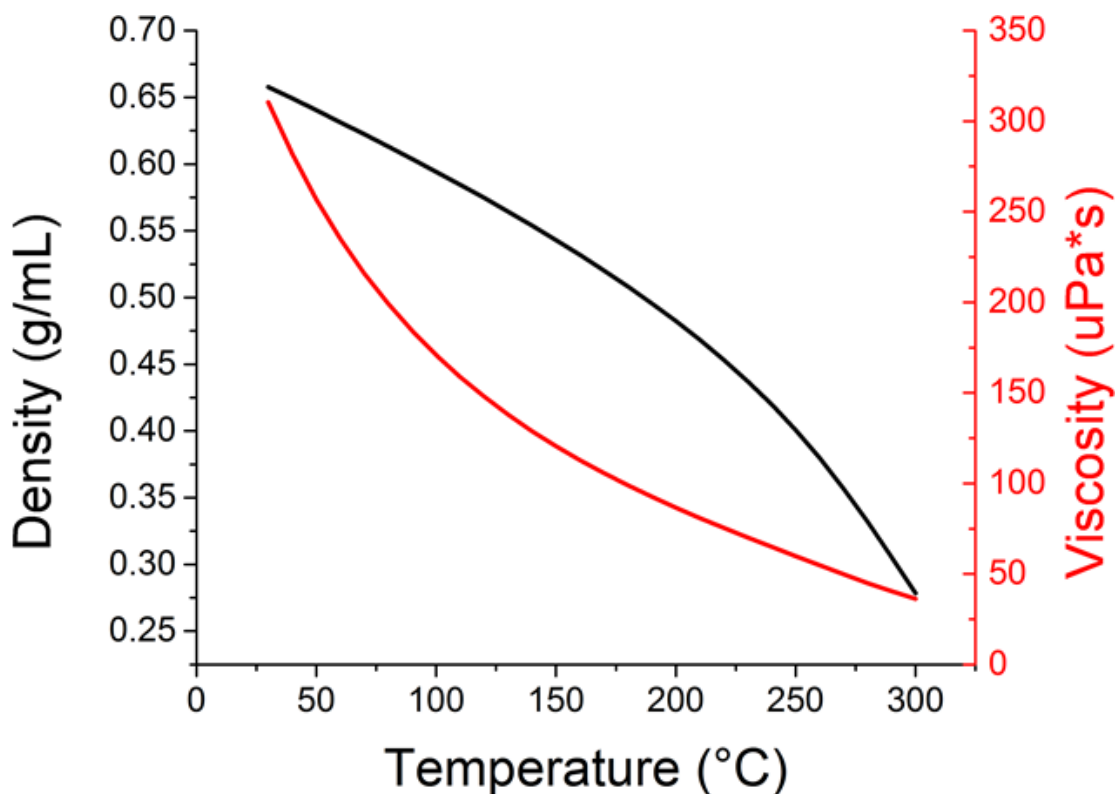


**Figure 4.11** Density and viscosity of hexane at 900 PSI as a function of temperature. Data from NIST Chemistry Webbook.<sup>105</sup>

Initially the reflux geometry was used to attempt to recrystallize rubrene in supercritical hexane. Unfortunately, this geometry produced an amorphous/semicrystalline film and no significant crystallization was observed. Thus, the diffusive geometry was used to crystallize rubrene from supercritical hexane. This allowed the semicrystalline source material to dissolve in the hot region and diffuse down the reactor, crystallizing in the colder region at approximately 75 °C. Orthorhombic rubrene crystals were formed using this method. The dimensions of the crystals were determined to be *ca.* 200  $\mu\text{m}$  long, 130  $\mu\text{m}$  wide, and 50  $\mu\text{m}$  tall, with a facet angle of *ca.* 115° at the ends of the long [100] axes, in excellent agreement with the crystal habit previously reported orthorhombic rubrene crystals (Figure 4.12).<sup>89</sup> This is the first reported crystallization of orthorhombic rubrene from a hexane solution.

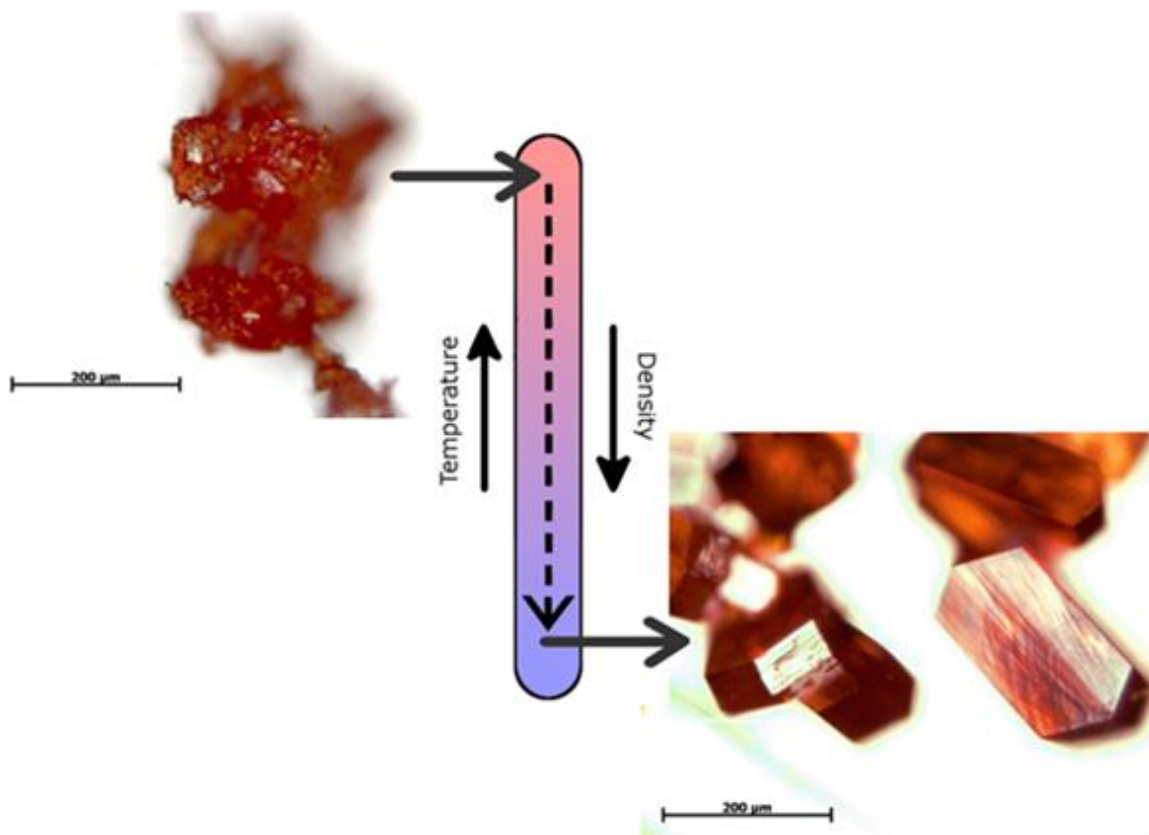


**Figure 4.12** Schematic illustrating the recrystallization of rubrene by diffusion through supercritical hexane. The polycrystalline source material was loaded into the upper portion of the reactor, which was then heated and pressurized. The rubrene diffused through the temperature and density gradient and crystallized in the lower, cooled region. The crystal habit corresponding to the orthorhombic crystal structure of rubrene is clearly observed.

#### 4.3.3 Fractionation and crystallization of oligothiophenes in supercritical hexane

Building upon the previous success in crystallizing rubrene in supercritical hexane, recrystallizations using poly[2,5-bis(3-dodecylthiophen-2-yl)thieno[3,2-*b*]thiophene] (PBTTT) was performed using similar conditions. Because of the higher cost associated with polythiophenes and other desirable polymer semiconductors, a new, smaller stainless steel pressure vessel was used for these experiments. The main crystallization cylinder was *ca.* 20 cm in length with a *ca.* 0.8 cm internal diameter, with a total volume of *ca.* 10 mL (Figure 4.13). This reduction in volume by 90% allowed for

the use of 90% less starting material. Approximately 5 mg of PBTTT was loaded into an aluminum foil boat which was placed in the upper, heated portion of the pressure vessel, and the recrystallization occurred with this diffusive transport geometry. The hot zone surrounding the sample was heated to 290 °C and the sealed vessel reached a pressure of 900 PSI, resulting in a solvent density of 0.27 g/mL in the heated zone (Figure 4.14).



**Figure 4.13** Image of the small pressure reactor in the diffusive geometry.

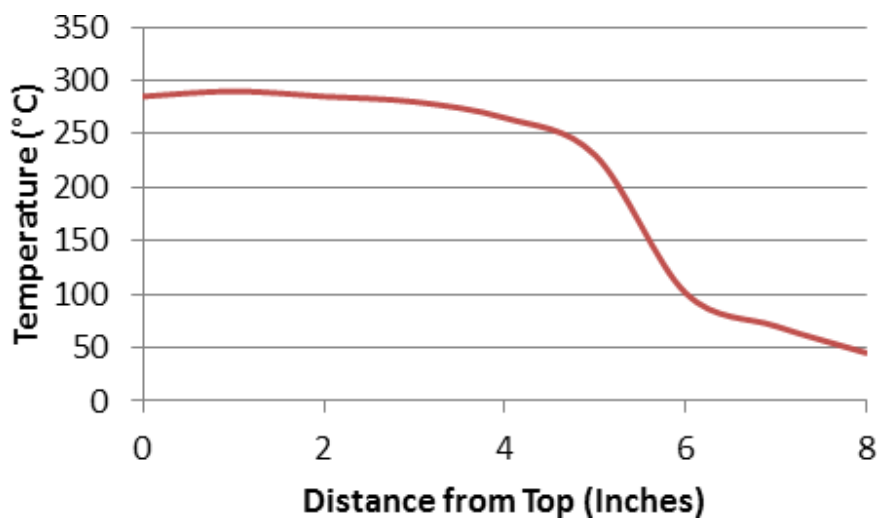


**Figure 4.14** Temperature profile for the small pressure reactor.

Remarkably, and in contrast to previous experiments, crystals were not formed in the cooler, lower region, but were found inside the aluminum sample boat. Instead of diffusing centimeters to tens of centimeters from the source material, the material diffused millimeters and crystals were nucleated on the rough aluminum surface. Long, needle-like crystals were observed; these crystals were *ca.* 200 nm in width and *ca.* 50  $\mu\text{m}$  in length. The experiment was repeated using the reflux geometry and the same results were obtained; crystals were only formed within the aluminum sample boat in the hot zone (Figure 4.15). Additionally, the recrystallization was relatively insensitive to the exact temperature and pressure during the procedure. Crystals were obtained with reactor temperatures of 250 – 320  $^{\circ}\text{C}$  and pressures of 600 – 3000 PSI.

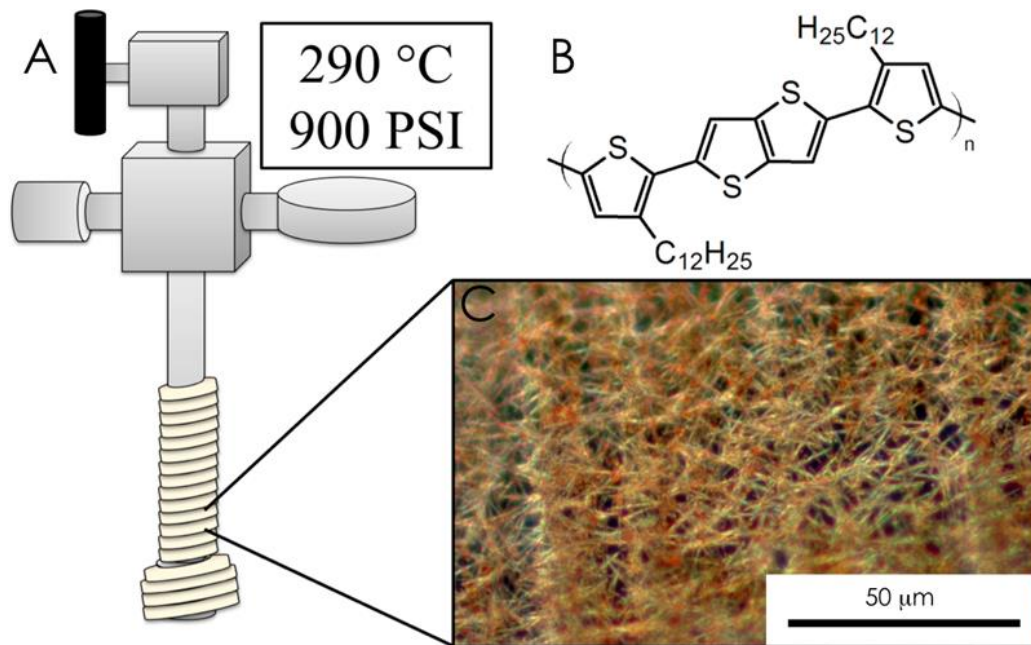


**Figure 4.15** Schematic of the steel pressure reactor (A), molecular structure of PBTTT (B), and optical micrograph of the as-grown crystals (C).

To ensure that it was truly the PBTTT which crystallized, the source PBTTT was purified *via* Soxhlet extraction with methanol, which removed all residual catalyst, and crystals were still obtained. This indicated that the crystallized material was not catalyst or other impurities. Additionally, the source PBTTT was purified *via* Soxhlet extraction with ethyl ether, which removed low molecular weight species, and no crystals were observed with this high molecular weight PBTTT. This indicated that it was primarily or solely low molecular weight PBTTT which crystallized into these crystalline needles.

#### 4.3.4 Characterization of PBTTT crystal species molecular weight

To determine the nature of the species crystallized *via* this process, matrix-assisted laser desorption ionization time-of-flight (MALDI-ToF) mass spectrometry was performed on the crystals. This revealed a single peak at  $m/z = 1140$  which is the molecular weight of the BTTT monomer with two additional bithiophene groups (BTTT1.5) (Figure 4.16). Additionally, the molecular weights of other potential PBTTT

fragments were calculated and compared with the molecular weight observed *via* MALDI-ToF, and the BTTT1.5 structure is the only possible molecule which is of the correct molecular weight (Table 4.1). Furthermore, MALDI-ToF analysis of the source polymer reveals a significant amount of BTTT1.5 present in the crude material and the molecular weight of BTTT1.5 in the source is equal to that of the crystals. Fractionation of aliphatic polymers has been reported previously, but this is the first observation of a concurrent fractionation and recrystallization of conjugated materials.

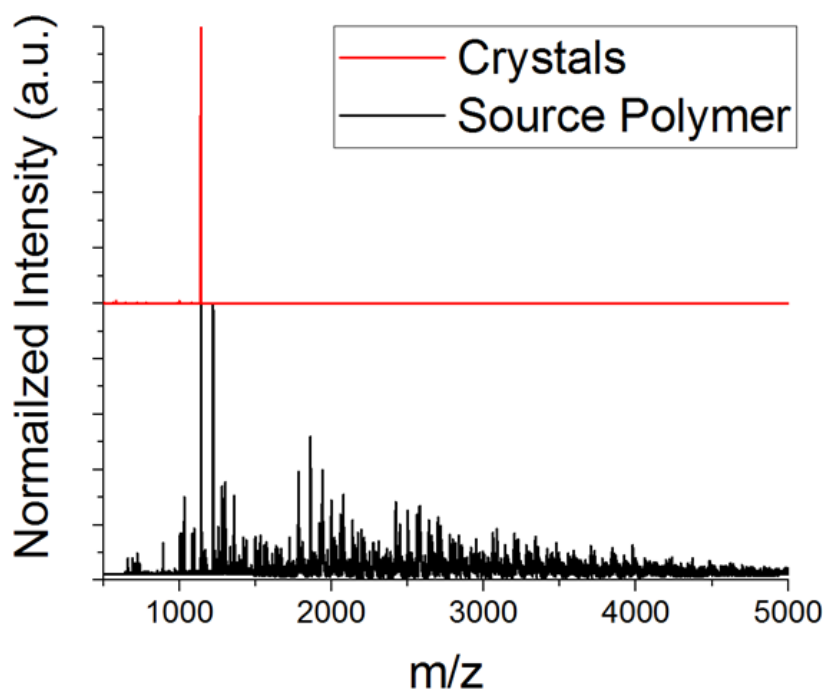


**Figure 4.16.** MALDI-ToF data for the crystals and source polymer. The crystals consisted of a single molecular species, demonstrating that the material was separated from the disperse source polymer. Additionally, a high concentration of BTTT1.5 is observed in the polymer.

**Table 4.1** Molecular weight of potential structures for PBTTT degradation. To identify any possible degradation products which may be present at the observed molecular weight of 1140 Da, the molecular weight of a series of PBTTT repeat units was calculated (tt = thieno[3,2-*b*]thiophene, t = dodecylthiophene). The possibility of alkyl chain scission was explored, however, the only structure with the target molecular weight was shown to be BTTT1.5

Target (m/z):	1140													
<b>Backbone structure</b>	<b>tt</b>	<b>t</b>	<b>t</b>	<b>tt</b>	<b>t</b>	<b>t</b>	<b>tt</b>	<b>t</b>	<b>t</b>	<b>tt</b>	<b>t</b>	<b>t</b>	<b>tt</b>	<b>t</b>
As synthesized	138	389	639	777	1028	1278	1416	1667	1917	2055	2306	2556	2695	2945
Without 1 dodecyl chain		220	471	609	859	1110	1248	1499	1749	1887	2138	2388	2526	2777
Without 2 dodecyl chains			302	441	691	942	1080	1330	1581	1719	1969	2220	2358	2608
Without 3 dodecyl chains					523	773	911	1162	1412	1550	1801	2051	2190	2440
Without 4 dodecyl chains						605	743	994	1244	1382	1633	1883	2021	2272
Without 5 dodecyl chains								825	1076	1214	1464	1715	1853	2103
Without 6 dodecyl chains									907	1046	1296	1546	1685	1935
<b>Backbone structure</b>	<b>t</b>	<b>t</b>	<b>tt</b>	<b>t</b>	<b>t</b>	<b>tt</b>	<b>t</b>	<b>t</b>	<b>tt</b>	<b>t</b>	<b>t</b>	<b>tt</b>	<b>t</b>	
As synthesized	250	501	639	890	1140	1278	1529	1779	1917	2168	2418	2556	2807	
Without 1 dodecyl chain	82	333	471	721	972	1110	1360	1611	1749	1999	2250	2388	2638	
Without 2 dodecyl chains		164	302	553	803	942	1192	1442	1581	1831	2081	2220	2470	
Without 3 dodecyl chains				385	635	773	1024	1274	1412	1663	1913	2051	2302	
Without 4 dodecyl chains					467	605	855	1106	1244	1494	1745	1883	2133	
Without 5 dodecyl chains							687	937	1076	1326	1577	1715	1965	
Without 6 dodecyl chains								769	907	1158	1408	1546	1797	
Without 7 dodecyl chains										989	1240	1378	1628	
Without 8 dodecyl chains											1072	1210	1460	
<b>Backbone structure</b>	<b>t</b>	<b>tt</b>	<b>t</b>	<b>t</b>	<b>tt</b>	<b>t</b>	<b>t</b>	<b>tt</b>	<b>t</b>	<b>t</b>	<b>tt</b>	<b>t</b>		
As synthesized	250	389	639	890	1028	1278	1529	1667	1917	2168	2306	2556		
Without 1 dodecyl chain	82	220	471	721	859	1110	1360	1499	1749	1999	2138	2388		
Without 2 dodecyl chains			302	553	691	942	1192	1330	1581	1831	1969	2220		
Without 3 dodecyl chains				385	523	773	1024	1162	1412	1663	1801	2051		
Without 4 dodecyl chains						605	855	994	1244	1494	1633	1883		
Without 5 dodecyl chains							687	825	1076	1326	1464	1715		
Without 6 dodecyl chains								907	1158	1296	1546			
Without 7 dodecyl chains									989	1128	1378			



#### **4.3.5 Infrared spectroscopy of BTTT1.5 Crystals**

Infrared spectroscopy was used to confirm the molecular identity of the BTTT1.5 crystals. As shown in Figure 4.17, the characteristic vibrational modes of the source material were retained in both the crystals and residual hexane solution, indicating that the supercritical conditions did not degrade or decompose PBTTT, as depicted in Table 4.2). The spectroscopic data obtained for BTTT1.5 crystals was obtained by analyzing the crystals on the aluminum boat in which they were formed, as an insufficient amount of crystallized material was generated for it to be analyzed independent of a substrate. Nevertheless, as the aluminum background was subtracted from the spectrum, the vibrational modes for aromatic and aliphatic C-H stretching was still observed and the “fingerprint” region closely resembles that of both the source polymer and the material deposited from the residual solution.

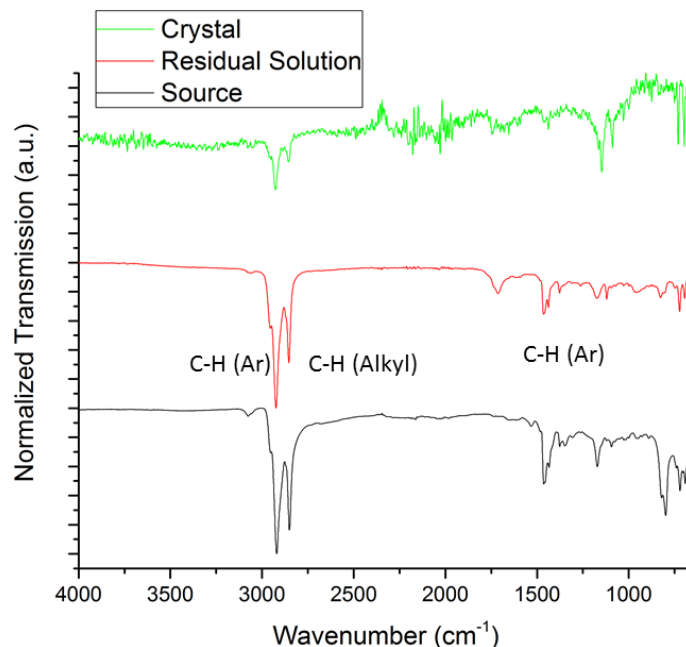


**Figure 4.17** Fourier transform infrared spectra of the BTTT1.5 crystals, PBTTT material recovered from the residual hexane solution after recrystallization, and unpurified source material.

**Table 4.2** Wavenumbers of aromatic and aliphatic (alkyl) C-H stretching modes as observed by FTIR spectroscopy.

Material	Aromatic C-H Stretch ( $\text{cm}^{-1}$ )	Alkyl C-H Stretch ( $\text{cm}^{-1}$ )
Crystals	2926	2855
Residual	2924	2853
Source	2920	2850

#### 4.3.6 Characterization of BTTT1.5 crystal habit

Numerous techniques were employed to characterize the crystal habit of the BTTT1.5 crystals. Atomic force microscopy (AFM) was used to characterize the dimensions and profile of the needle-like crystals (Figure 4.18). The micrographs revealed sharp, well-defined facets with angles of  $120^\circ$ , forming perfect hexagons in cross-section. Scanning electron microscopy (SEM) confirmed the hexagonal structure of the crystals (Figure 4.19). Additionally, SEM was used to characterize the average

crystal widths (the average length could not be determined due to the high aspect ratio and crystal fracture upon transfer) (Figure 4.20). A roughly Gaussian distribution of widths was observed which is consistent with a well-controlled, diffusion-mediated crystallization process. Furthermore, the average crystal width was determined to be  $196 \pm 72$  nm. This is in striking contrast to the widths observed via optical microscopy. Because these crystals interact very strongly with visible light (Figure 4.21), they appear to be much wider when viewed optically, and thus SEM was necessary to determine the true size of the crystals.

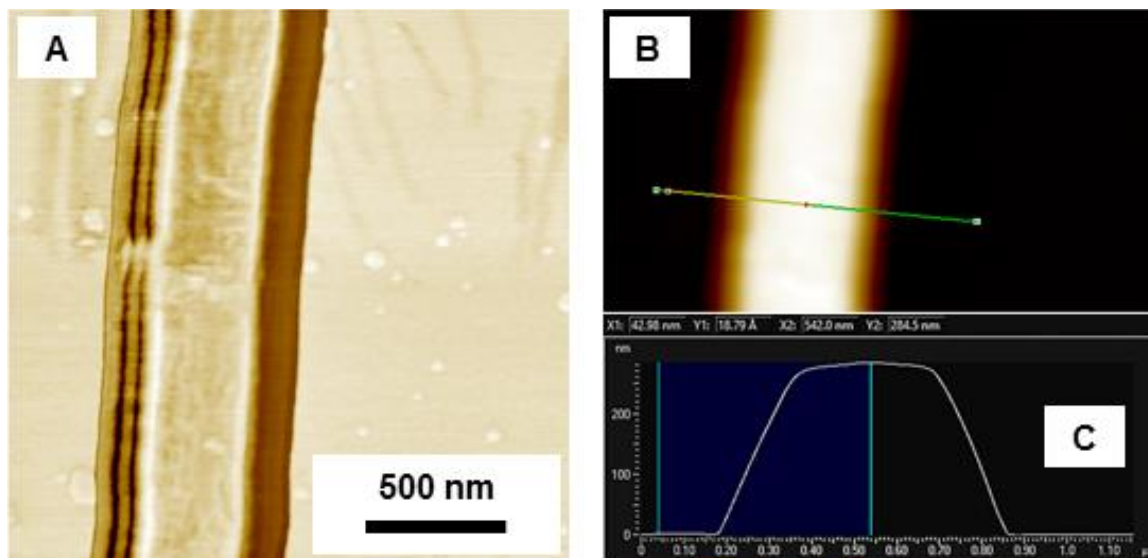


**Figure 4.18** Atomic force phase (A) and height (B) micrographs of a BTTT1.5 crystal. Profile of the crystal, demonstrating the sharp facets of the crystals, with  $120^\circ$  angles between faces.

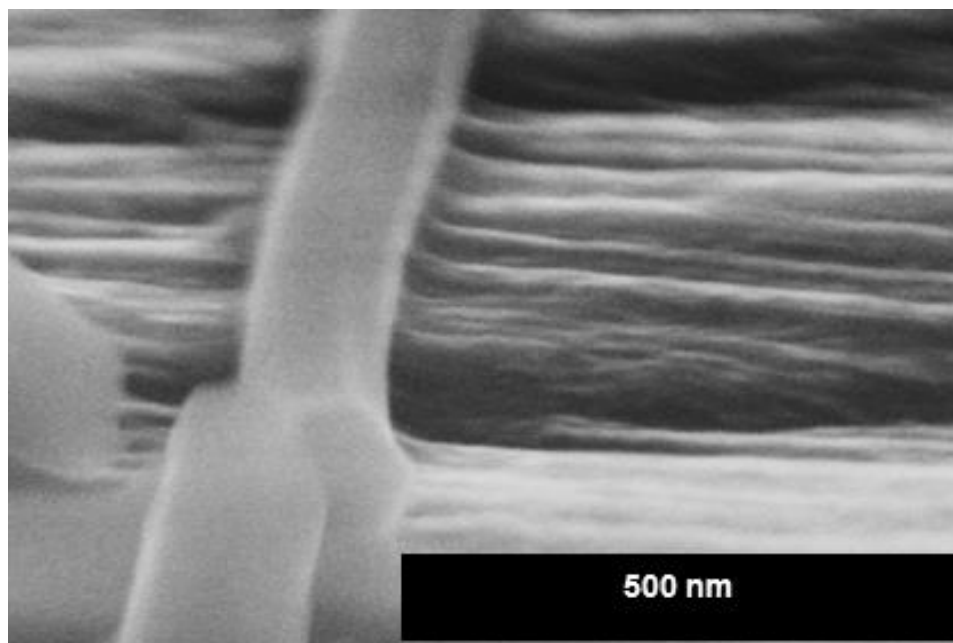


**Figure 4.19** Scanning electron micrograph of a tilted BTTT1.5 crystal which has been bisected. The regular hexagonal profile is clearly observed.

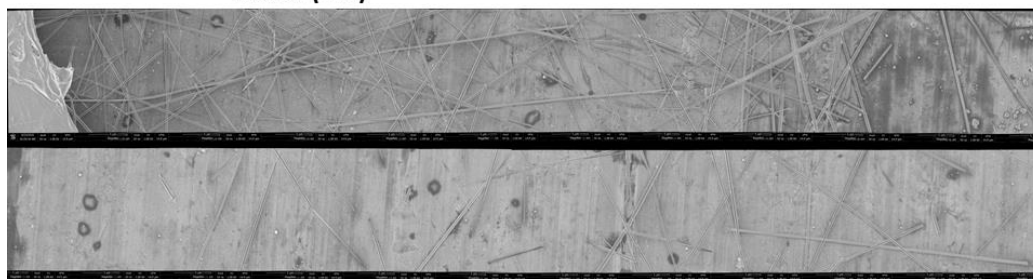
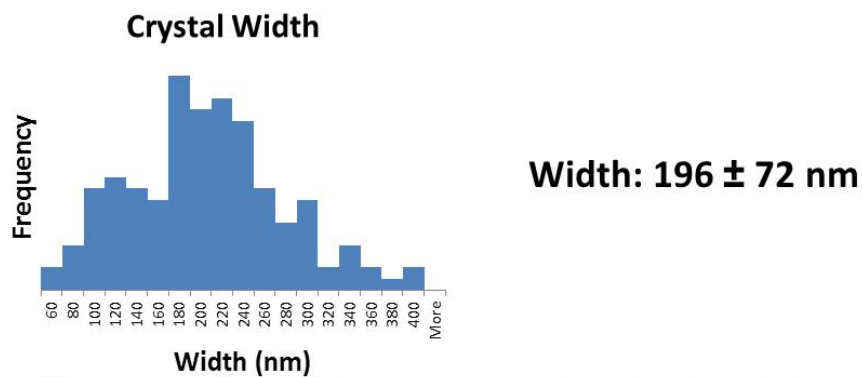


**Figure 4.20** A series of scanning electron micrographs “stitched” together. The source material is seen at the far left of the upper image. The resulting image was analyzed to determine the distribution of crystal widths.

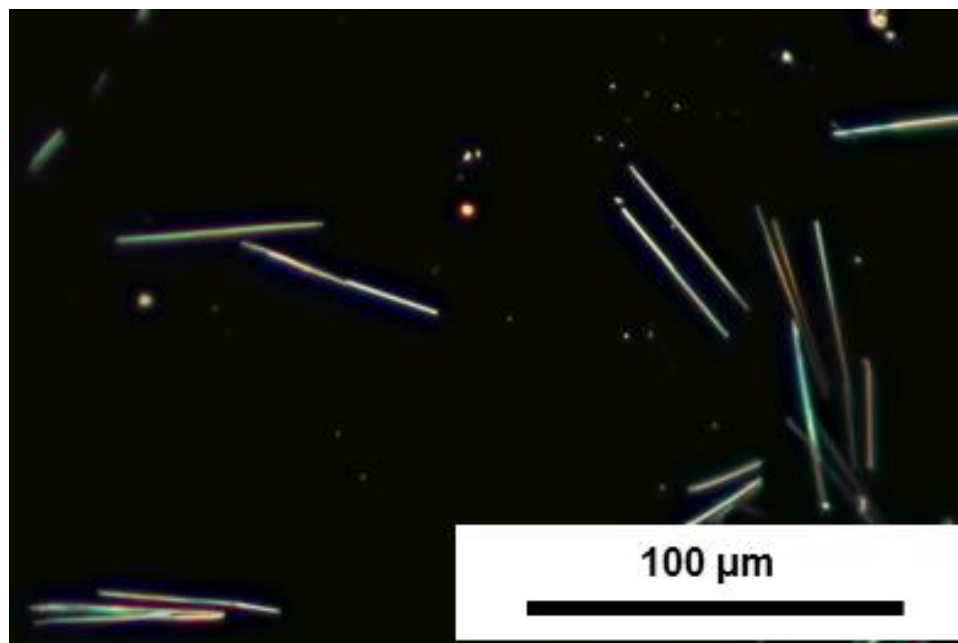


**Figure 4.21** Optical micrograph of BTTT1.5 crystals. The crystals are observed to be approximately 50  $\mu\text{m}$  in length, however their width appears substantially larger than in electron micrographs due to the strong interaction of the crystals with visible light.

#### **4.3.7 Characterization of BTTT1.5 unit cell parameters and molecular packing relative to the crystal axis.**

Transmission electron microscopy (TEM) was also used to characterize the crystal shape and size. The hexagonal structure of the crystals was apparent; sharp facets, mirroring those seen via AFM, were observed. Additionally, selected-area electron diffraction (SAED) was used to determine some of the unit cell parameters for the BTTT1.5 crystals (Figure 4.22). The [010] and [001] directions were identified. The unit cell parameters  $b$ ,  $c$ , and  $a$  were determined to be 8.78  $\text{\AA}$ , 20.1  $\text{\AA}$ , and  $90^\circ$ , respectively.

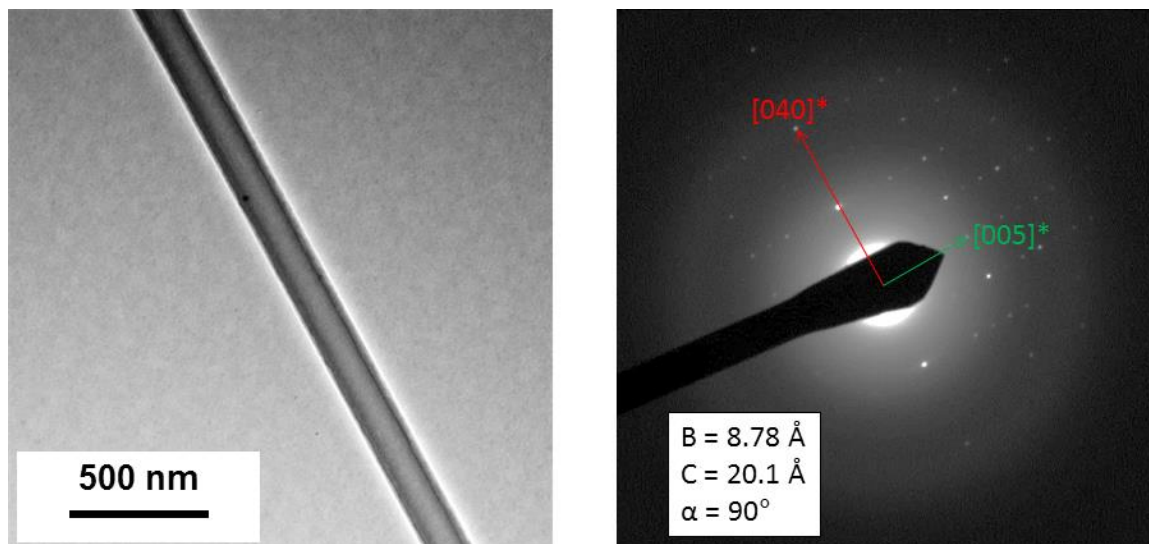


**Figure 4.22** Transmission electron micrograph and selected area electron diffraction of a single BTTT1.5 crystal. Numerous reflections are observed in the diffraction pattern, owing to the high crystallinity and strong long-range order of the crystal. The planes of reflection are identified and unit cell parameters are calculated using Bragg's law.

Polarization-resolved photoluminescence (PRPL) was used to determine the relative orientation of the oligomer backbones (Figure 4.23). In this technique, linear polarized laser light (488 nm) was used to optically excite the crystals. By rotating the polarization of the incident light and measuring the photoluminescence (PL) response, a variation in PL intensity was observed. The PL response was highest when the crystals were excited by incident light which was  $25 \pm 3^\circ$  away from the transverse crystal axis. This highest response is indicative of the light polarization being aligned with the strongest transition dipole moment of BTTT1.5, *i.e.* along the oligomer backbone. This angle is very similar to that observed for the tilt of DDQT-3 oligomers relative to the crystal axis as characterized by TEM.

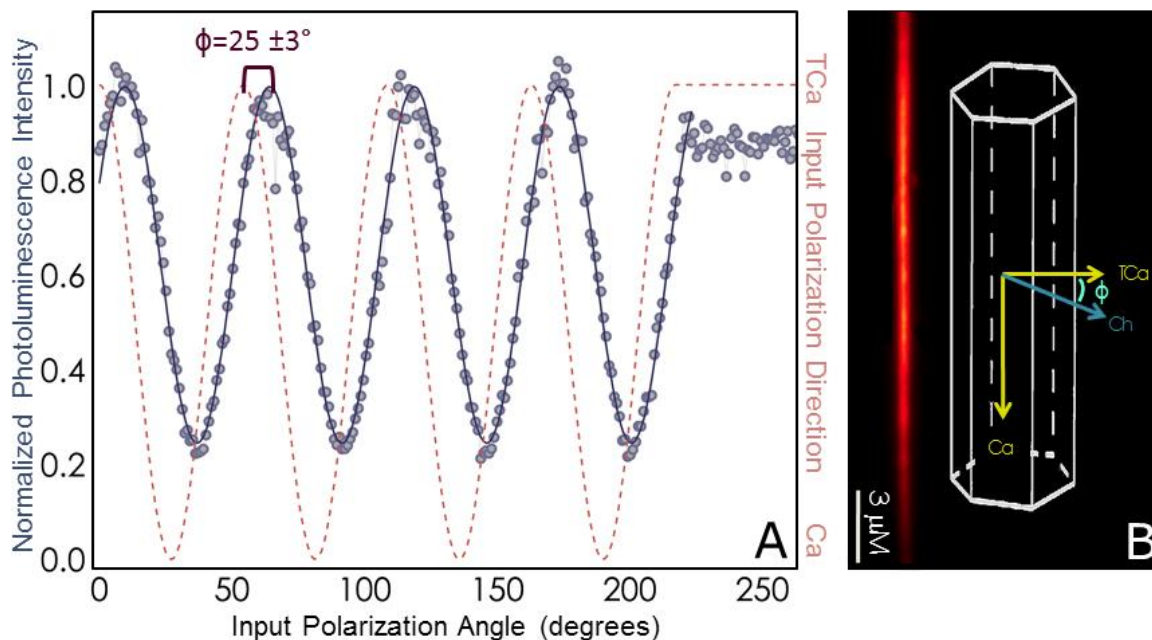


**Figure 4.23** Polarization-resolved photoluminescence data (A) and a photoluminescence image of a PBTtT1.5 crystal and schematic of the crystal, with labeled axes (B). The dashed red line represents the polarization of the laser used to excite the crystal, while the solid blue line is an interpolation of the photoluminescent response. The highest PL intensity is observed when the incident light is  $25 \pm 3^\circ$  relative to the transverse crystal axis (TCa).

Through analyzing these results, a rudimentary crystal structure schematic can be generated. A fully extended BTTT1.5 oligomer with a contour length of  $20.64 \text{ \AA}$  was placed in a two-dimensional approximation of the unit cell (*i.e.* neglecting the  $a$  direction of depth) at an angle of  $25 \pm 3^\circ$  relative to the  $c$  axis. By filling the unit cell with molecules, this results in a very tight  $\pi$  stacking distance of  $3.3 \text{ \AA}$ , indicating very strong  $\pi$ - $\pi$  interactions between neighboring BTTT1.5 chains (Figure 4.24).

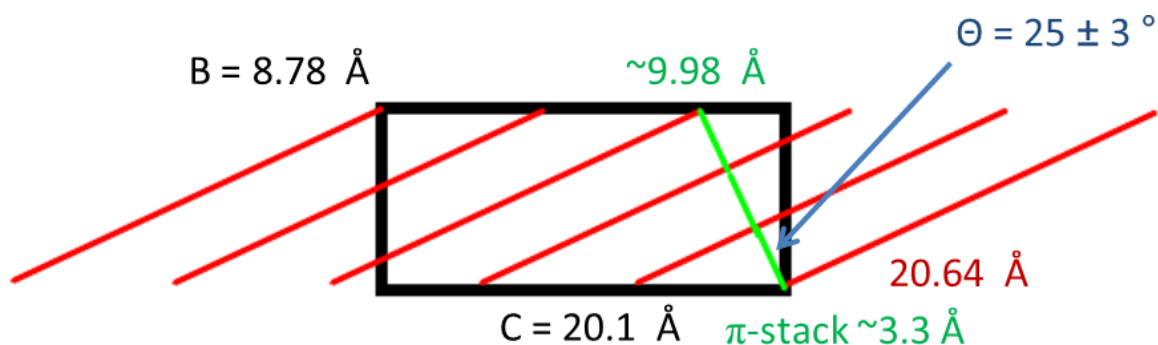


**Figure 4.24** Schematic of a potential unit cell. This orientation of PBTTT1.5 chains was developed by comparing the unit cell calculated from SAED with the angle of the oligomer axis as characterized by PRPL. The tight  $\pi$ - $\pi$  stacking distance as well as substantial backbone overlap suggests that strong electronic coupling may be present in the crystals.

#### 4.3.8 Characterization of BTTT1.5 molecular coupling in crystals

In order to probe the coupling within the crystals, both along the oligomer backbones and through the  $\pi$  stack, time- and polarization-resolved photoluminescence (TPRPL) experiments were performed (Figure 4.25). By exciting molecules with light polarized at different angles relative to the crystal axis and analyzing the decay dynamics, one can determine the extent of charge transfer during the PL process. Through this experimental setup, the excitation mechanism was controlled and the emission mechanism was monitored. Four angles of excitation were selected: along the crystal axis, transverse to the crystal axis, along the oligomer backbones, and transverse to the oligomer backbones (the  $\pi$ -stack direction). The PL emission was separated into two orthogonal polarizations: along the crystal axis and transverse to the crystal axis.

At all angles of excitation, the exciton recombination and PL emission behavior transverse to the crystal axis was starkly different to that observed along the crystal axis. The emission along the crystal axis obeyed a power law decay function

$$I(t) = At^{-p}$$



which is indicative of polaron pair recombination. In contrast, the PL decay transverse to the crystal axis obeyed exponential decay

$$I(t) = \sum_n A_n e^{-t/\tau_n}$$

which is characteristic of bound exciton recombination. Furthermore, the polarization of excitation was correlated with the polarization of emission. Crystals which were excited along the  $\pi$  stack, *i.e.* along the crystal axis or transverse to the oligomer backbones, showed a stronger power law response, as indicated by their smaller exponents ( $p = ca.$  2.8). This is characteristic for larger electron-hole separation distances along this axis, suggesting that the oligomers are strongly coupled in this direction. The exponential decay dynamics transverse to the crystal axis also varied with the polarization of excitation, with longer lived excitations (16 – 19 ns) occurring when exciting along the oligomer backbone.

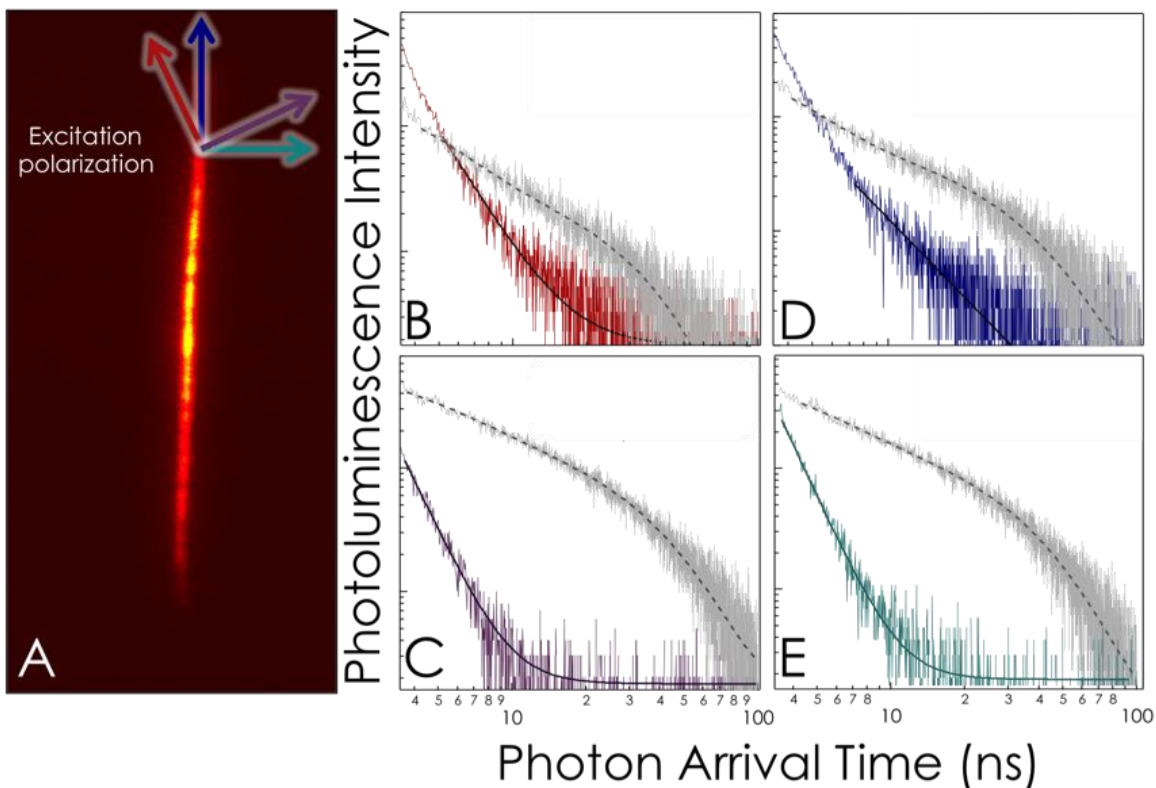


**Figure 4.25** Time and polarization resolved photoluminescent responses (B-E) of a single BTTT1.5 crystal (A). The polarization orientations of excitation are indicated by the colored arrows, corresponding to the crystal axis (Ca, blue), transverse crystal axis (TCa, green), chromophore axis (Ch, purple) and transverse chromophore axis (TCh, red). The photoluminescent responses are resolved into components polarized along Ca (in color) and TCa (in grey) from the same crystal, excited along each of the 4 axes, as indicated by their colors. The solid lines represent power law-fitted responses to the Ca emission and the dashed lines represent exponential-fitted responses to the TCA emission.

#### **4.3.9 Comparison of BTTT1.5 crystals generated in supercritical hexane with BTTT1.5 crystals generated *via* traditional solution recrystallization**

While the source PBTTT was highly disperse in molecular weight and the isolation of BTTT1.5 was difficult outside of the reported supercritical crystallization method, pure BTTT1.5 was synthesized *via* Stille coupling so that the pure, known material could be compared to that of the crystals. This material was then crystallized in hexane at ambient atmospheric pressure and temperature and the photoluminescence

spectra of these crystals were compared with those obtained by crystallization from supercritical hexane (Figure 4.26).

These crystals, a solution of synthesized BTTT1.5 in chloroform, and a drop cast film of the synthesized BTTT1.5 were characterized *via* photoluminescence spectroscopy and compared with the spectrum obtained from the BTTT1.5 crystals grown in supercritical solution. The solution spectrum exhibited the highest energy emission, as expected, while the crystals grown in liquid hexane displayed a strongly bathochromically shifted emission. This strong “red-shift” is indicative of J-type coupling, where oligothiophenes are strongly coupled in the direction of their major transition dipole moment, *i.e.* along the backbone, and weakly coupled in the transverse,  $\pi$ -stack direction. In contrast, the semicrystalline film obtained from drop casting a chloroform solution of the synthesized BTTT1.5 closely resembled that of the crystals obtained in supercritical hexane, with the only observable difference being a high-energy shoulder which can be ascribed to disordered oligomer which is present in the film but not the single crystal. These results indicate that the crystals obtained under supercritical conditions are actually representative of the crystallites observed in the device-relevant oligomer film, while the crystals grown in hexane under atmosphere conditions represent a polymorph. Furthermore, the metastable state of the crystals grown under standard conditions was revealed during this analysis: the crystals began to melt and resolidify, and the resulting emission was similar to that of the BTTT1.5 film.

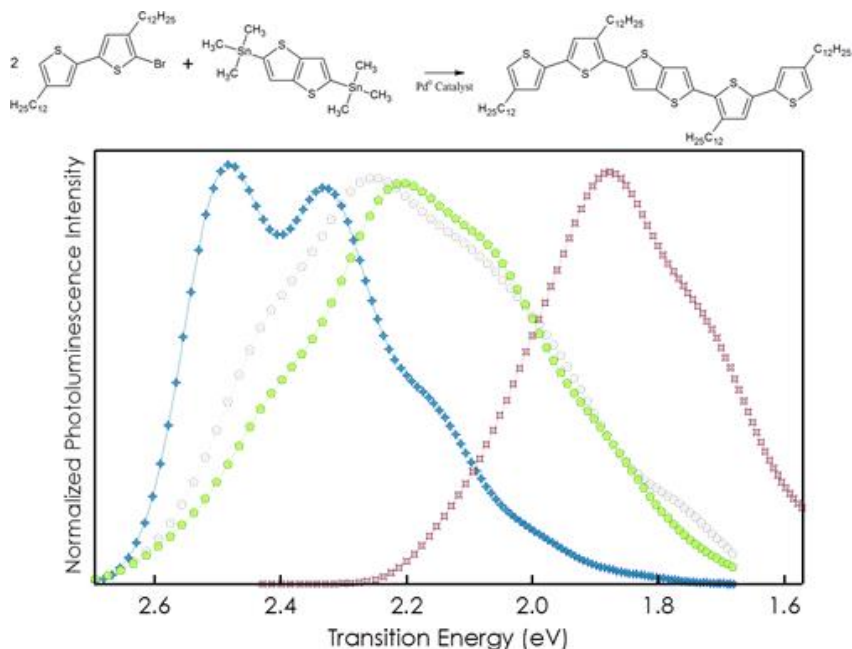


**Figure 4.26** Synthetic scheme of BTTT1.5 and the photoluminescent spectra of the solution (blue), polycrystalline film (grey), crystal grown in supercritical hexane (green), and crystal grown in hexane at ambient conditions (red). The strong bathochromic shift of the crystal grown under ambient conditions is indicative of J-type coupling, while the suppression of the 0-0 emission in the crystal grown under supercritical conditions is indicative of H-type coupling.

#### 4.3.10 Summary

This work reported the development of a novel crystallization technique which maximized the advantages of the solubilizing and transport properties of supercritical fluids. This method leveraged the solvation advantages of solution crystallization and controlled diffusion properties of physical vapor transport to establish a technique for the concurrent purification, fractionation, and crystallization of organic semiconductors. The crystal habit, structure, and coupling properties of the resulting crystals were characterized, revealing a tightly packed structure that is optimal for charge transport. Furthermore, the crystals were demonstrated to be representative of the crystallites found in a polycrystalline film, the crystals grown by traditional solution methods were metastable polymorphs that did not display the same optoelectronic properties of the

thermodynamically stable crystallites. This work produced a method which may be broadly applicable for the fractionation and crystallization of other conjugated polymeric systems.

## CHAPTER 5

### FINAL COMMENTS AND OUTLOOK

#### 5.1 Conclusions

This work provides a basis for the use of oligomers and single crystals as model systems for studying the intrinsic properties of polythiophenes. Three approaches for developing model systems were established.

The characterization of monodisperse, molecularly-defined oligomers was completed to evaluate the transition in relevant properties from monomer to hexamer. It was shown that the morphological properties of the oligomers begin to represent the polymer with a quaterthiophene tetramer, while the optoelectronic properties begin to converge with the pentamer. Furthermore, the pentamer forms crystalline nanostructures which may be representative of polymer crystallites.

The solid-state interactions between oligomer and polymer was characterized and it was shown that oligomers are not simply impurities in polymer films. Remarkably, films which contained a majority, 83%, oligomer exhibited morphological and charge transport properties equivalent to that of high molecular weight polymer. This demonstrated that it is the connectivity of polythiophenes which is their defining feature in producing high-performance organic electronics and that increased oligomer content may increase the crystallinity, and therefore performance, of organic field-effect transistors.

A novel method for the isolation and crystallization of oligomeric species was developed. This technique, which maximized the advantageous solubilizing and

transport properties of supercritical fluids, was used to create representative oligomer crystals which were sufficiently large to be characterized. The crystal properties, including crystal habit, partial unit cell, and molecular coupling, were determined and it was demonstrated that this tightly packed structure was representative of the oligomer crystallites present in thin films, while traditionally solution grown crystals consisted of a metastable polymorph. This recrystallization technique is broadly applicable to other polymeric and oligomer conjugated systems.

## BIBLIOGRAPHY

1. Gershenson, M. E. & Podzorov, V. Colloquium: Electronic transport in single-crystal organic transistors. *Rev. Mod. Phys.* **78**, 973–989 (2006).
2. Coropceanu, V. *et al.* Charge transport in organic semiconductors. *Chem. Rev.* **107**, 926–52 (2007).
3. Olivier, Y. *et al.* 25th anniversary article: high-mobility hole and electron transport conjugated polymers: how structure defines function. *Adv. Mater.* **26**, 2119–36 (2014).
4. Shuai, Z., Wang, L. & Li, Q. Evaluation of charge mobility in organic materials: from localized to delocalized descriptions at a first-principles level. *Adv. Mater.* **23**, 1145–53 (2011).
5. Horowitz, G. Organic Field-Effect Transistors. *Adv. Mater.* **10**, 365–377 (1998).
6. Kippelen, B. & Brédas, J.-L. Organic photovoltaics. *Energy Environ. Sci.* **2**, 251 (2009).
7. Brédas, J.-L., Norton, J. E., Cornil, J. & Coropceanu, V. Molecular understanding of organic solar cells: the challenges. *Acc. Chem. Res.* **42**, 1691–9 (2009).
8. Podzorov, V. Organic single crystals: Addressing the fundamentals of organic electronics. *MRS Bull.* **38**, 15–24 (2013).
9. Horowitz, G. Organic thin film transistors: From theory to real devices. *J. Mater. Res.* **19**, 1946–1962 (2004).
10. Murphy, A. R. & Fréchet, J. M. J. Organic semiconducting oligomers for use in thin film transistors. *Chem. Rev.* **107**, 1066–96 (2007).
11. Anthony, J. E. Functionalized acenes and heteroacenes for organic electronics. *Chem. Rev.* **106**, 5028–48 (2006).
12. Dou, L. *et al.* 25th anniversary article: a decade of organic/polymeric photovoltaic research. *Adv. Mater.* **25**, 6642–71 (2013).
13. Dong, H., Fu, X., Liu, J., Wang, Z. & Hu, W. 25th anniversary article: key points for high-mobility organic field-effect transistors. *Adv. Mater.* **25**, 6158–83 (2013).
14. Thompson, B. C. & Fréchet, J. M. J. Polymer-fullerene composite solar cells. *Angew. Chemie Int. Ed.* **47**, 58–77 (2008).



15. Beaujuge, P. M. & Fréchet, J. M. J. Molecular design and ordering effects in  $\pi$ -functional materials for transistor and solar cell applications. *J. Am. Chem. Soc.* **133**, 20009–29 (2011).
16. McCullough, R. D. The Chemistry of Conducting Polythiophenes. *Adv. Mater.* **10**, 93–116 (1998).
17. De Boer, R. W. I., Gershenson, M. E., Morpurgo, A. F. & Podzorov, V. Organic single-crystal field-effect transistors. *Phys. status solidi* **201**, 1302–1331 (2004).
18. Chabinyk, M. L., Jimison, L. H., Rivnay, J. & Salleo, A. Connecting Electrical and Molecular Properties of Semiconducting Polymers for Thin-Film Transistors. *MRS Bull.* **33**, 683–689 (2011).
19. Rivnay, J., Mannsfeld, S. C. B., Miller, C. E., Salleo, A. & Toney, M. F. Quantitative determination of organic semiconductor microstructure from the molecular to device scale. *Chem. Rev.* **112**, 5488–519 (2012).
20. Koch, F. P. V. *et al.* The impact of molecular weight on microstructure and charge transport in semicrystalline polymer semiconductors—poly(3-hexylthiophene), a model study. *Prog. Polym. Sci.* **38**, 1978–1989 (2013).
21. Salleo, A. Charge transport in polymeric transistors. *Mater. Today* **10**, 38–45 (2007).
22. Noriega, R. *et al.* A general relationship between disorder, aggregation and charge transport in conjugated polymers. *Nat. Mater.* **12**, 1038–44 (2013).
23. Kline, R. J. *et al.* Dependence of Regioregular Poly(3-hexylthiophene) Film Morphology and Field-Effect Mobility on Molecular Weight. *Macromolecules* **38**, 3312–3319 (2005).
24. Schuettfort, T. *et al.* Microstructure of polycrystalline PBTTT films: domain mapping and structure formation. *ACS Nano* **6**, 1849–64 (2012).
25. Podzorov, V. Conjugated polymers: Long and winding polymeric roads. *Nat. Mater.* **12**, 947–8 (2013).
26. Lezama, I. G. & Morpurgo, A. F. Progress in organic single-crystal field-effect transistors. *MRS Bull.* **38**, 51–56 (2013).
27. Carrier, C., Organic, S. & Transistors, F. Charge Carrier Transport in Single-Crystal Organic Field-Effect Transistors. 27–156 (2007).
28. Lim, J. A., Liu, F., Ferdous, S., Muthukumar, M. & Briseno, A. L. Polymer semiconductor crystals. *Mater. Today* **13**, 14–24 (2010).

29. *Electronic Materials: The Oligomer Approach*. (WILEY-VCH Verlag, 2008).
30. Heeney, M. *et al.* Stable polythiophene semiconductors incorporating thieno[2,3-b]thiophene. *J. Am. Chem. Soc.* **127**, 1078–9 (2005).
31. Kline, R. J., McGehee, M. D., Kadnikova, E. N., Liu, J. & Fréchet, J. M. J. Controlling the Field-Effect Mobility of Regioregular Polythiophene by Changing the Molecular Weight. *Adv. Mater.* **15**, 1519–1522 (2003).
32. Prosa, T. J., Winokur, M. J., Moulton, J., Smith, P. & Heeger, A. J. X-ray structural studies of poly(3-alkylthiophenes): an example of an inverse comb. *Macromolecules* **25**, 4364–4372 (1992).
33. Kline, R. J. *et al.* Critical Role of Side-Chain Attachment Density on the Order and Device Performance of Polythiophenes. *Macromolecules* **40**, 7960–7965 (2007).
34. DeLongchamp, D. M. *et al.* High Carrier Mobility Polythiophene Thin Films: Structure Determination by Experiment and Theory. *Adv. Mater.* **19**, 833–837 (2007).
35. Zen, A. *et al.* Effect of Molecular Weight and Annealing of Poly(3-hexylthiophene)s on the Performance of Organic Field-Effect Transistors. *Adv. Funct. Mater.* **14**, 757–764 (2004).
36. Joshi, S. *et al.* Thickness Dependence of the Crystalline Structure and Hole Mobility in Thin Films of Low Molecular Weight Poly(3-hexylthiophene). *Macromolecules* **41**, 6800–6808 (2008).
37. Li, G. *et al.* High-efficiency solution processable polymer photovoltaic cells by self-organization of polymer blends. *Nat. Mater.* **4**, 864–868 (2005).
38. Coffin, R. C., Peet, J., Rogers, J. & Bazan, G. C. Streamlined microwave-assisted preparation of narrow-bandgap conjugated polymers for high-performance bulk heterojunction solar cells. *Nat. Chem.* **1**, 657–61 (2009).
39. Schilinsky, P., Asawapirom, U., Scherf, U., Biele, M. & Brabec, C. J. Influence of the Molecular Weight of Poly(3-hexylthiophene) on the Performance of Bulk Heterojunction Solar Cells. *Chem. Mater.* **17**, 2175–2180 (2005).
40. Yamamoto, T., Sanechika, K. & Yamamoto, A. Preparation of thermostable and electric-conducting poly(2,5-thienylene). *J. Polym. Sci. Polym. Lett. Ed.* **18**, 9–12 (1980).
41. Sato, M., Tanaka, S. & Kaeriyama, K. Soluble conducting polythiophenes. *J. Chem. Soc. Chem. Commun.* 873 (1986). doi:10.1039/c39860000873

42. Sirringhaus, H. *et al.* Two-dimensional charge transport in self-organized, high-mobility conjugated polymers. *Nature* **401**, 685–688 (1999).
43. Verilhac, J. M. *et al.* Effect of macromolecular parameters and processing conditions on supramolecular organisation, morphology and electrical transport properties in thin layers of regioregular poly(3-hexylthiophene). *Synth. Met.* **156**, 815–823 (2006).
44. Bäuerle, P., Fischer, T., Bidlingmeier, B., Rabe, J. P. & Stabel, A. Oligothiophenes—Yet Longer? Synthesis, Characterization, and Scanning Tunneling Microscopy Images of Homologous, Isomerically Pure Oligo(alkylthiophene)s. *Angew. Chemie Int. Ed. English* **34**, 303–307 (1995).
45. Mena-Osteritz, E. *et al.* Two-Dimensional Crystals of Poly(3-Alkyl-thiophene)s: Direct Visualization of Polymer Folds in Submolecular Resolution. *Angew. Chem. Int. Ed. Engl.* **39**, 2679–2684 (2000).
46. Azumi, R., Gotz, G., Debaerdemaeker, T. & Bauerle, P. Coincidence of the molecular organization of beta-substituted oligothiophenes in two-dimensional layers and three-dimensional crystals. *Chemistry* **6**, 735–44 (2000).
47. Izumi, T., Kobashi, S., Takimiya, K., Aso, Y. & Otsubo, T. Synthesis and spectroscopic properties of a series of beta-blocked long oligothiophenes up to the 96-mer: reevaluation of effective conjugation length. *J. Am. Chem. Soc.* **125**, 5286–7 (2003).
48. Takimiya, K., Sakamoto, K., Otsubo, T. & Kunugi, Y. Thin Film Characteristics and FET Performances of  $\beta$ -Octyl-substituted Long Oligothiophenes. *Chem. Lett.* **35**, 942–943 (2006).
49. Mishra, A., Ma, C.-Q. & Bäuerle, P. Functional oligothiophenes: molecular design for multidimensional nanoarchitectures and their applications. *Chem. Rev.* **109**, 1141–276 (2009).
50. Roncali, J. Synthetic Principles for Bandgap Control in Linear  $\pi$ -Conjugated Systems. *Chem. Rev.* **97**, 173–206 (1997).
51. Jimison, L., Salleo, A., Chabinyc, M., Bernstein, D. & Toney, M. Correlating the microstructure of thin films of poly[5,5-bis(3-dodecyl-2-thienyl)-2,2-bithiophene] with charge transport: Effect of dielectric surface energy and thermal annealing. *Phys. Rev. B* **78**, 1–18 (2008).
52. Zhang, L. *et al.* Synthesis, electronic structure, molecular packing/morphology evolution, and carrier mobilities of pure oligo-/poly(alkylthiophenes). *J. Am. Chem. Soc.* **135**, 844–54 (2013).

53. Ong, B. S., Wu, Y., Liu, P. & Gardner, S. High-performance semiconducting polythiophenes for organic thin-film transistors. *J. Am. Chem. Soc.* **126**, 3378–9 (2004).
54. Azumi, R., Mena-Osteritz, E., Boese, R., Benet-Buchholz, J. & Bäuerle, P. The longest oligothiophene ever examined by X-ray structure analysis. *J. Mater. Chem.* **16**, 728 (2006).
55. Briseno, A. L. *et al.* Fabrication of field-effect transistors from hexathiapentacene single-crystal nanowires. *Nano Lett.* **7**, 668–75 (2007).
56. Tang, Q., Li, H., Liu, Y. & Hu, W. High-performance air-stable n-type transistors with an asymmetrical device configuration based on organic single-crystalline submicrometer/nanometer ribbons. *J. Am. Chem. Soc.* **128**, 14634–9 (2006).
57. Xiao, S. *et al.* Transferring self-assembled, nanoscale cables into electrical devices. *J. Am. Chem. Soc.* **128**, 10700–1 (2006).
58. Yuan, Q. *et al.* Microstructure of Oligofluorene Asymmetric Derivatives in Organic Thin Film Transistors. *Chem. Mater.* **20**, 2763–2772 (2008).
59. Mannsfeld, S. C. B., Tang, M. L. & Bao, Z. Thin film structure of triisopropylsilylethynyl-functionalized pentacene and tetraceno[2,3-b]thiophene from grazing incidence X-ray diffraction. *Adv. Mater.* **23**, 127–31 (2011).
60. Yuan, Q. *et al.* Thin film structure of tetraceno[2,3-b]thiophene characterized by grazing incidence X-ray scattering and near-edge X-ray absorption fine structure analysis. *J. Am. Chem. Soc.* **130**, 3502–8 (2008).
61. Bredas, J.-L. Mind the gap! *Mater. Horizons* **1**, 17 (2014).
62. Wenz, G., Mueller, M. A., Schmidt, M. & Wegner, G. Structure of poly(diacetylenes) in solution. *Macromolecules* **17**, 837–850 (1984).
63. Bidan, G., De Nicola, A., Enée, V. & Guillerez, S. Synthesis and UV–Visible Properties of Soluble Regioregular Oligo(3-octylthiophenes), Monomer to Hexamer. *Chem. Mater.* **10**, 1052–1058 (1998).
64. Meier, H., Stalmach, U. & Kolshorn, H. Effective conjugation length and UV/vis spectra of oligomers. *Acta Polym.* **48**, 379–384 (1997).
65. Zade, S. S. & Bendikov, M. From oligomers to polymer: convergence in the HOMO-LUMO gaps of conjugated oligomers. *Org. Lett.* **8**, 5243–6 (2006).
66. Koch, F. P. V., Smith, P. & Heeney, M. ‘Fibonacci’s route’ to regioregular oligo(3-hexylthiophene)s. *J. Am. Chem. Soc.* **135**, 13695–8 (2013).

67. You, J. *et al.* A polymer tandem solar cell with 10.6% power conversion efficiency. *Nat. Commun.* **4**, 1446 (2013).
68. He, Z. *et al.* Enhanced power-conversion efficiency in polymer solar cells using an inverted device structure. *Nat. Photonics* **6**, 593–597 (2012).
69. Tseng, H.-R. *et al.* High-mobility field-effect transistors fabricated with macroscopic aligned semiconducting polymers. *Adv. Mater.* **26**, 2993–8 (2014).
70. Mei, J., Diao, Y., Appleton, A. L., Fang, L. & Bao, Z. Integrated materials design of organic semiconductors for field-effect transistors. *J. Am. Chem. Soc.* **135**, 6724–46 (2013).
71. Bäuerle, P. & Cremer, J. Oligo(thienylene ethynylene)s: A New Class of Oligomeric Model Compounds. *Chem. Mater.* **20**, 2696–2703 (2008).
72. Banerjee, M., Shukla, R. & Rathore, R. Synthesis, optical, and electronic properties of soluble poly-p-phenylene oligomers as models for molecular wires. *J. Am. Chem. Soc.* **131**, 1780–6 (2009).
73. Zhang, L., Colella, N. S., Cherniawski, B. P., Mannsfeld, S. C. B. & Briseno, A. L. Oligothiophene semiconductors: synthesis, characterization, and applications for organic devices. *ACS Appl. Mater. Interfaces* **6**, 5327–43 (2014).
74. Park, S. K., Jackson, T. N., Anthony, J. E. & Mourey, D. A. High mobility solution processed 6,13-bis(triisopropyl-silylethynyl) pentacene organic thin film transistors. *Appl. Phys. Lett.* **91**, 063514 (2007).
75. Wei Chou, K. *et al.* Late stage crystallization and healing during spin-coating enhance carrier transport in small-molecule organic semiconductors. *J. Mater. Chem. C* **2**, 5681 (2014).
76. Podzorov, V. Charge Carrier Transport in Single-Crystal Organic Field-Effect Transistors. 27–156 (2007).
77. Mollinger, S. A., Krajina, B. A., Noriega, R., Salleo, A. & Spakowitz, A. J. Percolation, Tie-Molecules, and the Microstructural Determinants of Charge Transport in Semicrystalline Conjugated Polymers. *ACS Macro Lett.* 708–712 (2015). doi:10.1021/acsmacrolett.5b00314
78. McCulloch, I. *et al.* Liquid-crystalline semiconducting polymers with high charge-carrier mobility. *Nat. Mater.* **5**, 328–33 (2006).
79. Arias, A. C., Endicott, F. & Street, R. A. Surface-Induced Self-Encapsulation of Polymer Thin-Film Transistors. *Adv. Mater.* **18**, 2900–2904 (2006).

80. Jo, P. S., Duong, D. T., Park, J., Sinclair, R. & Salleo, A. Control of Rubrene Polymorphs via Polymer Binders: Applications in Organic Field-Effect Transistors. *Chem. Mater.* 150529143722006 (2015). doi:10.1021/acs.chemmater.5b00884
81. Gasperini, A. & Sivula, K. Effects of Molecular Weight on Microstructure and Carrier Transport in a Semicrystalline Poly(thieno)thiophene. *Macromolecules* **46**, 9349–9358 (2013).
82. Muthukumar, M. & Welch, P. Modeling polymer crystallization from solutions. *Polymer (Guildf)*. **41**, 8833–8837 (2000).
83. Muthukumar, M. Progress in Understanding of Polymer Crystallization. *Notes* **714**, 1–18 (2007).
84. Malik, S. & Nandi, A. K. Crystallization mechanism of regioregular poly(3-alkyl thiophene)s. *J. Polym. Sci. Part B Polym. Phys.* **40**, 2073–2085 (2002).
85. Briseno, A. L. *et al.* Patterning organic single-crystal transistor arrays. *Nature* **444**, 913–7 (2006).
86. Wang, C. *et al.* Single crystal n-channel field effect transistors from solution-processed silylethynylated tetraazapentacene. *J. Mater. Chem.* **21**, 15201 (2011).
87. Rahimi, K. *et al.* Controllable processes for generating large single crystals of poly(3-hexylthiophene). *Angew. Chem. Int. Ed. Engl.* **51**, 11131–5 (2012).
88. Kloc, C., Simpkins, P. G., Siegrist, T. & Laudise, R. A. Physical vapor growth of centimeter-sized crystals of  $\alpha$ -hexathiophene. *J. Cryst. Growth* **182**, 416–427 (1997).
89. Reese, C. & Bao, Z. Organic single-crystal field-effect transistors. *Mater. Today* **10**, 20–27 (2007).
90. Podzorov, V., Pudalov, V. M. & Gershenson, M. E. Field-effect transistors on rubrene single crystals with parylene gate insulator. *Appl. Phys. Lett.* **82**, 1739 (2003).
91. Podzorov, V., Menard, E., Rogers, J. & Gershenson, M. Hall Effect in the Accumulation Layers on the Surface of Organic Semiconductors. *Phys. Rev. Lett.* **95**, 226601 (2005).
92. Okada, Y., Sakai, K., Uemura, T., Nakazawa, Y. & Takeya, J. Charge transport and Hall effect in rubrene single-crystal transistors under high pressure. *Phys. Rev. B* **84**, 245308 (2011).

93. Anitescu, G. Solubilities of solids in supercritical fluids—I. New quasistatic experimental method for polycyclic aromatic hydrocarbons (PAHs) + pure fluids. *J. Supercrit. Fluids* **10**, 175–189 (1997).
94. Cooper, A. I. Polymer synthesis and processing using supercritical carbon dioxide. *J. Mater. Chem.* **10**, 207–234 (2000).
95. Watkins, J. J., Krukonis, V. J., Condo, P. D., Pradhan, D. & Ehrlich, P. Fractionation of high density polyethylene in propane by isothermal pressure profiling and isobaric temperature profiling. *J. Supercrit. Fluids* **4**, 24–31 (1991).
96. Buchwald, A. & Kauschus, W. Description of the solubilities of solids in supercritical fluids. *J. Chromatogr. A* **777**, 283–287 (1997).
97. Marcus, Y. Are solubility parameters relevant to supercritical fluids? *J. Supercrit. Fluids* **38**, 7–12 (2006).
98. UC Davis ChemWiki. at <<http://chemwiki.ucdavis.edu/>>
99. *Catalytic Activation of Carbon Dioxide*. **363**, (American Chemical Society, 1988).
100. Laudise, R. A. Hydrothermal Synthesis of Crystals. *Chem. Eng. News* **65**, 30–43 (1987).
101. Lentz, H., Gehrig, M. & Schulmeyer, J. Dynamic solubility measurements of caffeine in carbon dioxide and in carbon dioxide saturated with water. *Phys. B+C* **139-140**, 70–72 (1986).
102. Takeya, J. *et al.* Very high-mobility organic single-crystal transistors with in-crystal conduction channels. *Appl. Phys. Lett.* **90**, 102120 (2007).
103. Huang, L. *et al.* Rubrene micro-crystals from solution routes: their crystallography, morphology and optical properties. *J. Mater. Chem.* **20**, 159 (2010).
104. Matsukawa, T. *et al.* Growth of thin rubrene single crystals from 1-propanol solvent. *J. Cryst. Growth* **312**, 310–313 (2010).
105. NIST Chemistry Webbook. at <<http://webbook.nist.gov/chemistry/>>